DENSITY FUNCTIONAL THEORY AND SCANNING TRANSMISSION ELECTRON MICROSCOPY: SYNERGISTIC TOOLS FOR MATERIALS INVESTIGATION

By

Timothy John Pennycook

Dissertation
Submitted to the Faculty of the
Graduate School of Vanderbilt University
in partial fulfillment of the requirements
for the degree of

DOCTOR OF PHILOSOPHY
in

Physics

May 2012

Nashville, Tennessee

Approved:
Prof. Sokrates T. Pantelides
Dr. Maria Varela
Prof. Sandra J. Rosenthal
Prof. Kálmán Varga
Dr. Mark P. Oxley

ACKNOWLEDGEMENTS

This work was made possible through the support of many people. I am grateful to all of them. In particular, I would like to thank Sokrates Pantelides for taking me as his student and for all the advise he has given me over the past five and a half years. Special thanks also go to Maria Varela for co-advising me and instructing me on the use of the microscopes. I am also grateful to the other members of my PhD committee, Mark Oxley, Kalman Varga and Sandra Rosenthal for their guidance and collaboration. I would like to thank Matthew Beck and Juan Carlos Idrobo for teaching me how to perform density functional theory calculations and many valuable discussions. I am also grateful to Oscar Restrepo and Weidong Luo for their advice on density functional theory calculations. Thanks go to Juan Carlos Idrobo, Matthew Chisholm, Andrew Lupini and William Sides for their aid and instruction in the use and maintenance of the microscopes. Thanks also go to Julia Luck for her instruction and assistance in the art of sample preparation. I am grateful to Jacobo Santamaria and his group for providing interesting samples and fruitful discussions. I thank James McBride for all the help he has given me with the CdSe project, both growing samples and working with me on the microscope. I thank George Hadjisavvas and Pantelis Kelires for collaborating with me on the Si nanocluster project. I thank Ondrej Krivanek and the other members of Nion for their help, advise and collaboration. Finally, I would like to thank my father, Stephen Pennycook and the rest of the Oak Ridge National Laboratory STEM group for providing use of the microscope facilities and a great many constructive, as well as fun, discussions. This work was supported by the US Department of Energy Grant DE-FG02-09ER46554 and the National Science Foundation GOALI under Grant No. DMR-0513048. Computations were performed at the National Energy Research Scientific Computing Center, which is supported by the Office of Science of the U.S. Department of Energy under Contract No. DE-AC02-05CH11231.

TABLE OF CONTENTS

Appendicies

LIST OF TABLES

LIST OF FIGURES

CHAPTER I

INTRODUCTION

The combination of density functional theory (DFT)[1, 2, 3, 4] and scanning transmission electron microscopy (STEM)[5, 6, 7] provides a very powerful means of synergistic atomic-scale materials investigation. STEM provides simultaneous atomic number contrast imaging [8, 9, 10, 11] and electron-energy loss spectroscopy (EELS) [12, 13, 14, 15] with atomic-scale spatial resolution. DFT provides a means of performing accurate quantum mechanical calculations of many materials properties, which are often difficult or impossible to probe experimentally. The strengths and limitations of the two methods are truly complementary, enabling a cycle of theory and experiment that self-consistently extends our knowledge of both practical materials science and fundamental physics.

1.1 STEM

In STEM, an electron beam is focused into a small probe and scanned across the sample as shown in Figure 1.1. The key advantage of the technique is that the scattering of the probe electrons out to different angles can be recorded simultaneously as a function of position. The most common configuration is to combine a large annular detector with a small disk detector and a electron-energy loss spectrometer. The annular detector typically detects scattering out to high angles while the small disk detects scattering to low angles. As scattering to high angles occurs when the probe is located over a strongly scattering object such as an atomic column, but not in empty space, the annular detector is called the annular dark field (ADF) detector. As empty space appears bright on the disk detector, it is called the bright field (BF) detector.

As on a conventional transmission electron microscope (TEM), interpreting bright

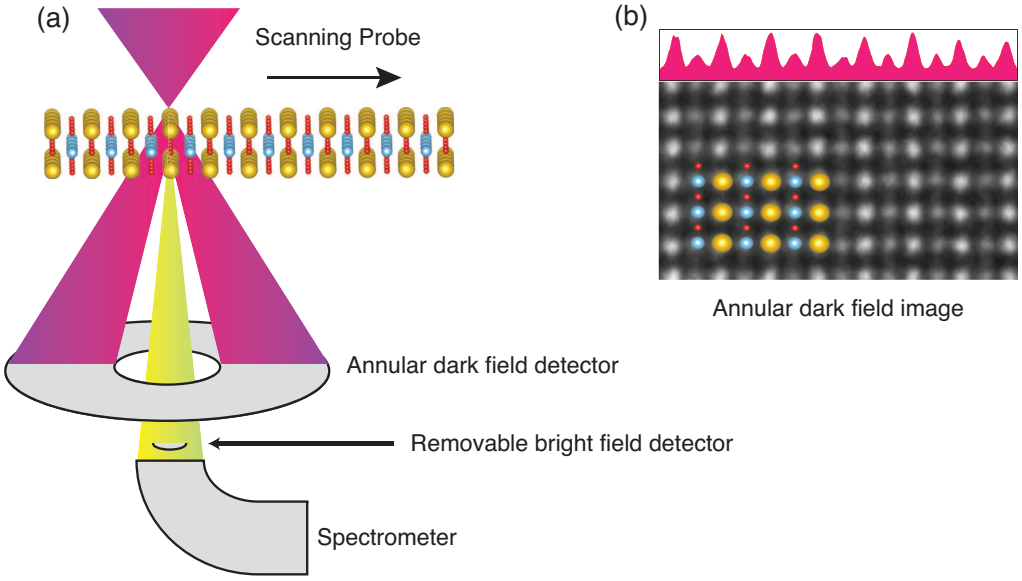

Figure 1.1: As the probe is scanned across the sample the electrons scattered to different angles are collected by different detectors. In this schematic the electrons scattered to low angles are collected by either a bright field detector or a spectrometer. Those scattered out to higher angles are collected by the annular dark field detector, the from which the signal intensity is roughly proportional to the square of the atomic number Z, as illustrated in part (b) of the figure.

field images is nontrivial. Bright field images are coherent, the result of the interference of many diffracting beams. As a result, bright field image contrast depends strongly on the sample thickness and the defocus of the electron beam. Atoms can appear dark on a bright background or bright on a dark background, and everything between. The images formed from the ADF detector on the other hand are mostly incoherent, as are the images we typically see with our eyes, and therefore much more easily interpreted. Atomic columns always appear bright on a dark background, with an intensity roughly proportional to Z^2 where Z is the atomic number of the constituent atoms. This is illustrated in Figure 1.1(b) for $SrTiO_3$ viewed down the $\langle 110 \rangle$ axis. The Z^2 dependance arises because in order to scatter to high angles, the beam electrons must pass very close to the nucleus of an atom where they undergo Rutherford scattering, seeing essentially the full nuclear potential. In order to obtain a useful signal, the inner detector angle is often reduced somewhat. The inclusion of signal from lower angles reduces the exponent somewhat, but the Z dependance remains strong. The reduction is caused by electrons scattered into lower angles seeing a nuclear charge screened by atomic electrons. The relative ease of interpreting the Z-contrast signal obtained from the high-angle ADF (HADF) detector makes it an ideal reference when combined with simultaneously acquired EELS or BF images.

The formation of the electron probe starts with the acceleration of electrons from an electron source. The much smaller wavelength of the electron is the reason why the resolution of electron microscopes far exceeds that of optical microscopes. As dictated by the de Broglie equation, the faster an electron travels, the smaller it's wavelength. Consequently, high voltages are used to accelerate the electrons. The higher the accelerating voltage, the higher the resolution. Prior to the advent of aberration correction, this led to the building of giant megavolt microscopes. Firing high energy electrons at a sample, however, has a tendency to cause damage, and modern microscopes typically operate between 60 and 300 kV. With aberration correction, this range of voltages is sufficient to look at most samples with atomic resolution. Resolutions of up to 0.5 Å [16, 17] have been achieved at 300 kV. The Nion UltraSTEM 100 [18, 19, 20], with its fifth-order aberration corrector has a probe size just

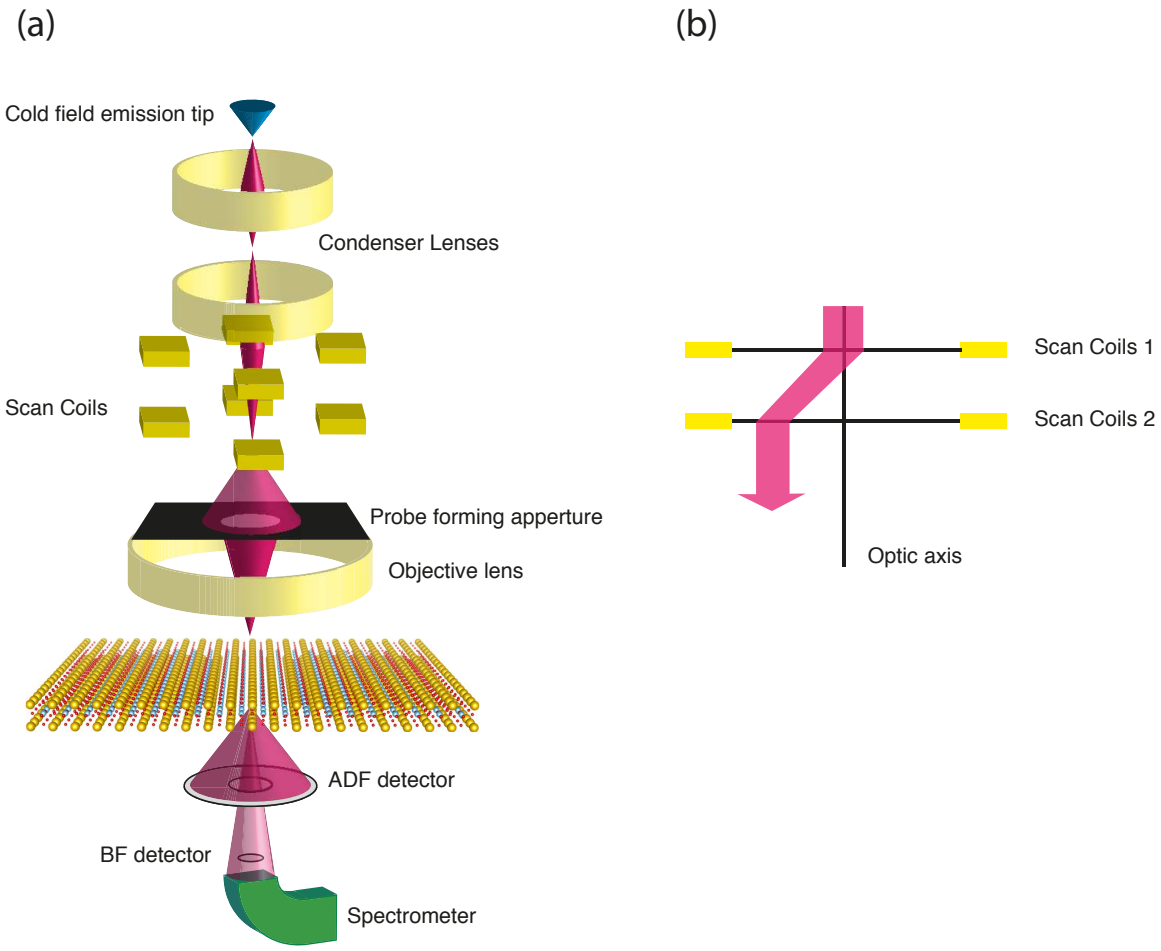

Figure 1.2: Schematic showing the optics used to form the probe (a). The two levels of scan coils work together to shift the beam across the sample without any net tilt (b).

over an Ångstrom at 60 kV. The optimal accelerating voltage depends on whether the specimen is more susceptible to knock-on or ionization damage. Knock-on damage, in which atoms are knocked out of a specimen by the momentum of the beam electrons, increases with with beam energy. Ionization damage, which results from electrons in the sample absorbing enough energy from the beam to be ejected, actually decreases with beam energy.

A number of electron sources can be used in the electron gun. Thermionic sources use heat to push electrons over the work function energy barrier of the source material and out into vacuum. Field emission sources use an electric field to pull electrons out. Sharp points enhance electric fields. For example applying a voltage V to a sphere with a radius of r produces an electric field $E = V/r$ [21]. For this reason, field emission sources use a very sharp needle, called a tip, as the emitter. In high-resolution STEM the size of the scanned probe is determined by a combination of the optics and the source. The optics produce a demagnified image of the source. As it is easier to form a small probe from a small source, using a cold field-emission gun (FEG) results in the best spatial resolution. Field emission requires a clean tip, which can be achieved by keeping the gun at ultra-high vacuum and only periodically heating the tip to remove any buildup of contamination. The need for ultra-high vacuum makes designing and maintaining a cold FEG more difficult, but the benefits are a considerably smaller source size and energy spread. For EELS, a cold FEG is particularly desirable, as the energy spread of the source is what typically limits the EELS energy resolution.

After being accelerated in the gun, the beam of electrons is demagnified by a set of condenser lenses (Figure 1.2(a)). Two layers of of fast deflectors, called scanning coils, allow the beam to be rastered across the sample. The first layer deflects the beam to produce a shift. The second layer brings the beam back to parallel with the optic axis, as illustrated in Figure 1.2(b). The final optical element involved in the formation of the electron probe is the objective lens. It is the most powerful lens, and does the largest amount of demagnification.

An ideal lens would put all rays from the same origin into focus at the same

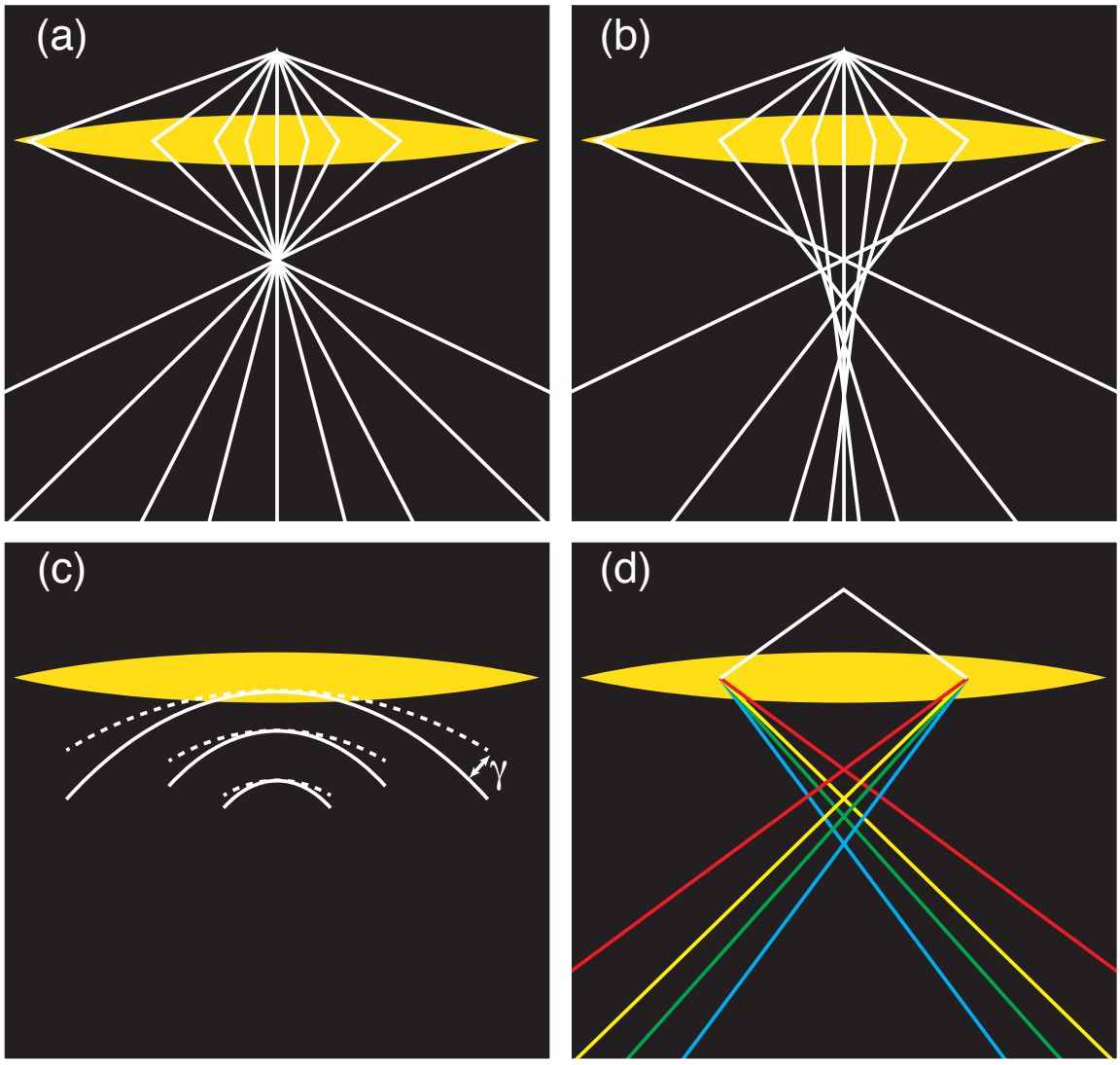

Figure 1.3: (a) Ray diagram for an ideal lens with no aberrations. (b) Ray diagram showing the effect of spherical aberrations (c) The aberrations cause the wavefronts to increasingly diverge from the ideal Gaussian wavefronts with increasing angle. (d) Ray diagram showing the effect of chromatic aberration.

point as in Figure 1.3(a). In reality, because of aberrations, the effect of a lens on a ray depends on the position, angle and energy of the ray. As the tip is small, particularly as seen by the objective lens, the difference in position of the incoming rays is small. Furthermore, the beam's distance from the optic axis also decreases as the magnification is increased, since it is scanned over a smaller area. In describing these aberrations for a STEM, it is therefore usual to neglect the dependence on the position of the incoming rays.

Figure 1.3(b) displays the angular dependence caused by spherical aberration, typically abbreviated as C_s. Rays traveling at different angles are converged by the lens to different points. It is called spherical aberration because the wavefront from an ideal lens would be a section of a spherical shell, collapsing to a point at the sample. One can imagine rotating the dashed arcs in Figure 1.3(c) around the optic axis to form a cylindrically symmetric bowls, each with a constant radius. Electrons traveling at higher angles through the lens are deflected more than those going through at low angles. This deviation γ is a function of the angle from the optic axis as illustrated by the difference between the dashed wavefronts and the solid aberrated wavefronts in Figure 1.3(c).

Chromatic aberration (C_c) is illustrated in Figure 1.3(d). Rays traveling at the same angles are converged by the lens to different points depending on the energy of the ray. In uncorrected STEMs, C_s typically dominates. Correction of the spherical aberrations is however getting good enough that chromatic aberrations do limit resolution, particularly at low accelerating voltages, even on machines with cold FEGs, and correctors for chromatic aberration have been developed.

The lens aberrations broaden the probe in a STEM, and thus reduce resolution. The simplest way of reducing C_s is to simply limit the range of angles with an aperture. To optimize resolution, however, one must also consider the effects of diffraction. A lens without aberrations would still turn points into disks because of diffraction at the outermost collection angle of the lens. These disks are called Airy disks and have a radius

$$r_a = 1.22\frac{\lambda}{\beta}, \tag{1.1}$$

where λ is the wavelength of the electron and β is the outermost semiangle of the aperture. So while using a smaller aperture helps reduce the effects of aberrations, it increases the diffraction limited resolution. The optimum aperture size is the one that balances the competing effects of aberrations and diffraction.

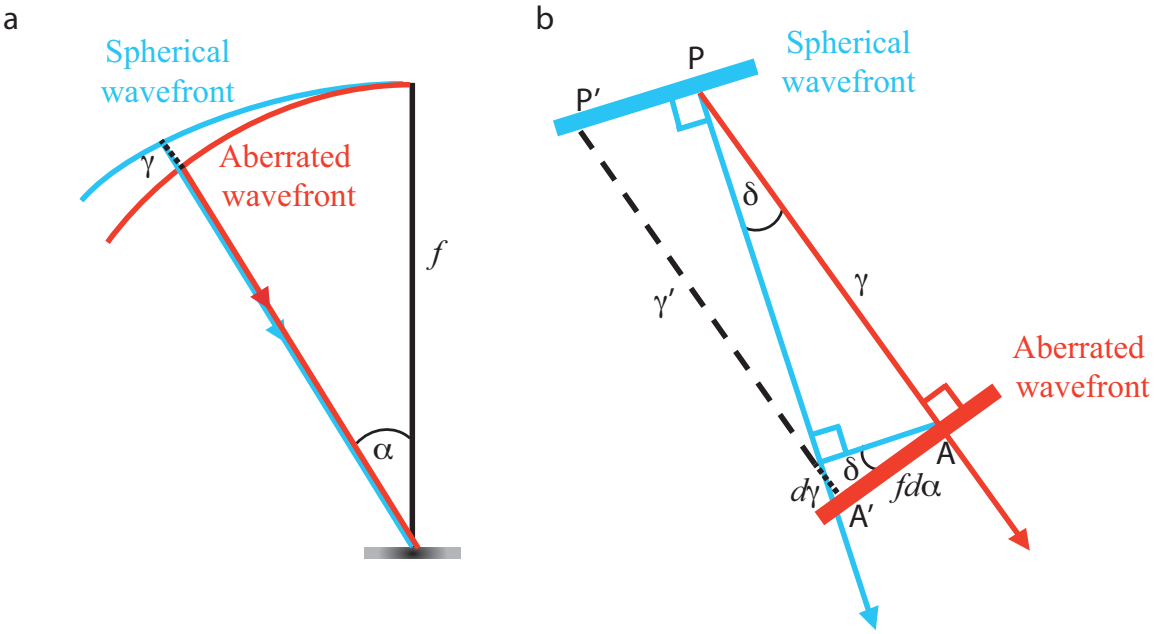

Figure 1.4: Diagrams displaying the relationship between the ideal and aberrated wavefronts and rays.

Determining the correct aperture size and understanding aberration correction requires a more precise mathematical description of the aberrations. Different basis sets can be used to represent the distance the wavefronts deviate from ideal due to spherical aberration, $\gamma(\alpha)$, but it is conventional to express it as a power series. In a spherical coordinate system with $\alpha = 0$ on the optic axis, we therefore expect the deviation γ to increase with the magnitude of α regardless of its sign. So we can rule out odd terms, and write

$$\gamma(\alpha) = \frac{1}{2}C_1\alpha^2 + \frac{1}{4}C_3\alpha^4 + \frac{1}{6}C_5\alpha^6 + \frac{1}{8}C_7\alpha^8 + \cdots . \tag{1.2}$$

Rays traveling at very low angles are insignificantly affected by spherical aberrations and converge at a point called the Gaussian focal point a distance f from the lens.

Let Δf_a denote the distance from this point at which aberrated rays cross the optic axis. The ratio of Δf_a to f in Figure 1.3(b) is exaggerated. In practice, $\Delta f \ll f$, and on the scale of viewing the whole path from the lens to the Gausian focal point, the rays will appear to converge at the same point as in Figure 1.4(a). For small α, the distance between the aberrated and spherical wavefronts will be very small compared to f, so the difference between the lengths P-P' and A-A' in Figure 1.4(b) will be negligible. In Figure 1.4(b) we have zoomed in very closely to the wavefronts coming out the objective lens. An infinitesimal change in α increases length of γ by an amount $d\gamma$. In this small angle approximation,

$$\delta \approx \tan(\delta) = \frac{1}{f}\frac{d\gamma}{d\alpha}, \tag{1.3}$$

and thus the angle which the path of the ray deviates at the lens increases with α as

$$\delta(\alpha) = C_1\alpha + C_3\alpha^3 + C_5\alpha^5 + C_7\alpha^7 + \cdots . \tag{1.4}$$

C_1 is just the distance the sample is from the Gaussian focal point of the lens δf. It can be changed by either moving the sample up and down the optic axis or changing the focal length of the lens with fine changes to the accelerating voltage or the lens current. It is now clear why we use terms such as third order and fifth order aberrations when speaking of aberration correction. Because α is small, the lowest order terms are the most important.

The probe shape is determined by the superposition of all rays allowed through the lens by the aperture. This can be though of as the interference of a set of plane waves whose phase is modified by the aberrations. The so called aberration function

$$\chi = \frac{2\pi}{\lambda}\gamma = \pi\delta f\lambda\mathbf{K}^2 + \frac{\pi}{2}C_3\lambda^3\mathbf{K}^4 + \frac{\pi}{3}C_5\lambda^5\mathbf{K}^6 + \frac{\pi}{4}C_7\lambda^7\mathbf{K}^8 + \cdots \tag{1.5}$$

expresses the phase error they cause in terms of the transverse wave vector $\mathbf{K}$ which has a magnitude $K = \alpha/\lambda$. The probe amplitude can be expressed as a function of

position $\mathbf{R}$ in the plane a distance δf from the focal plane as

$$P(\mathbf{R}) = \int \mathbf{A}(\mathbf{K}) e^{2\pi i \mathbf{K}\cdot\mathbf{R}} e^{-i\chi(\mathbf{K})} d\mathbf{K}, \tag{1.6}$$

where $A(\mathbf{K}) = 1$ inside the aperture and zero outside. The intensity is just the square

$$I(R) = P^2(\mathbf{R}) = \left[\int \mathbf{A}(\mathbf{K}) e^{2\pi i \mathbf{K}\cdot\mathbf{R}} e^{-i\chi(\mathbf{K})} d\mathbf{K} \right]^2. \tag{1.7}$$

The diameter of the probe due to aberrations can be determined from this as a function of defocus, which in turn can be used to determine the optimal aperture size.

In 1949 Scherzer showed that for round lenses, the coefficients in the aberration function, except defocus, are always positive [22]. He proved that, aside from using a slight negative defocus, one couldn't compensate higher order aberrations with rotationally symmetric lenses. He demonstrated, however, that a set of non-rotationally symmetric lenses could be employed to introduce negative aberrations and compensate the positive aberrations of round lenses. Without such aberration correction, Scherzer realized that microscopes in the 100-200 keV range would be limited to resolutions of about 2 Å. Scherzer even presented a design with which to compensate third order spherical aberrations, and pointed out that if it were possible to control C_3, it would be best to make it negative in order to compensate fifth-order aberrations.

It would take half century for a successful corrector to be built and demonstrated. It took so long because accurate correction requires a way to measure the aberrations, and calculate the best way to counteract them. Before the availability of fast computers and charged-coupled-device detectors, it was simply impossible to achieve the necessary precision. Haider et al. demonstrated the first successful correction of aberrations on a TEM using a hexapole corrector [23]. In 1998 Krivanek et al. demonstrated the first successful implementation of a probe corrector for a STEM the following year using a quadrupole/octupole design [24]. Following their initial success, Ondrej Krivanek and Niklas Dellby founded the Nion company and began

working to improve their corrector design. In 2002 sub-Å resolution was first demonstrated in an electron microscope using a Nion corrector on a VG Microscopes HB501 STEM running at 120kV [25]. Putting a similar Nion corrector into the 300 kV VG Microscopes HB603U pushed the resolution boundary down even further, allowing the 0.78 Å separation of Si ⟨112⟩ columns to be resolved [11].

The first aberration correctors all corrected up to third order aberrations. The more terms in the aberration function that are counteracted, the more the aperture can be opened up and the better the resolution. Soon after the success of the first third-order correctors, designs for fifth-order correctors began to appear [26, 27]. Using fifth order correctors 0.68 Å resolution was achieved in 2007 [28] and sub-0.5 Å was reached in 2009 [17, 29], all on 300 kV STEMs.

Fifth-order correction has also allowed lower kV beams to be used with atomic resolution, which is very useful for materials with lower thresholds for knock-on damage. Atomic resolution is now possible at 60 kV [20], and Z-contrast imaging has even been used to identify all the atoms, including substitutional O and C impurities in monolayer BN [19].

EELS also benefits from aberration correction. As with imaging, the finer probe increases the spatial resolution at which EELS can be acquired. The negative defocus used prior to aberration correction to increase image resolution also introduced large probe tails, which could pick up the spectroscopic signal of atoms adjacent to the one under the central peak of the probe [30]. Aberration correction mostly removes these tails, facilitating the interpretation of spatially resolved EELS.

EELS probes the electronic structure of materials by measuring the distribution of energies lost by the probe electrons. The distribution is divided into three regions. They are the zero-loss, low-loss and core-loss regions as shown schematically in Figure 1.5. As the name suggests, zero-loss electrons have not undergone significant inelastic scattering. TEM requires very thin samples, and usually the zero-loss peak is by far the largest feature in an EELS spectrum. The width of the zero loss peak is a good indicator of the energy resolution of the microscope, which is ideally limited only by the energy spread of the emission source. After the zero loss, the next features

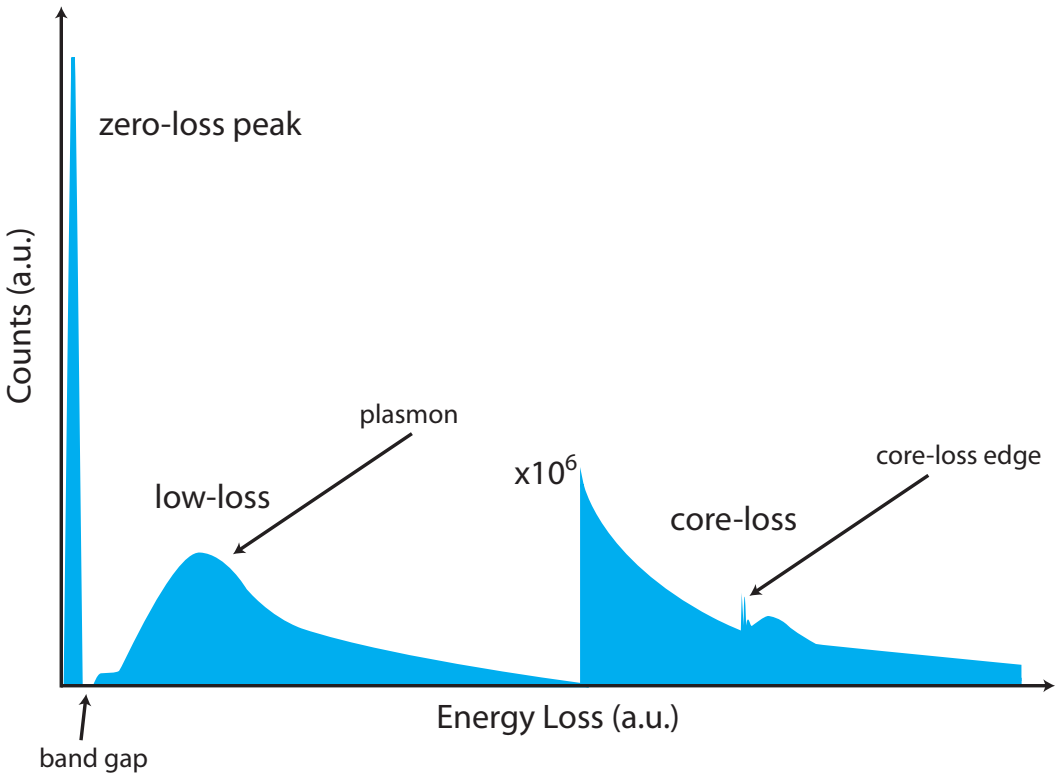

Figure 1.5: Schematic of an EELS spectrum.

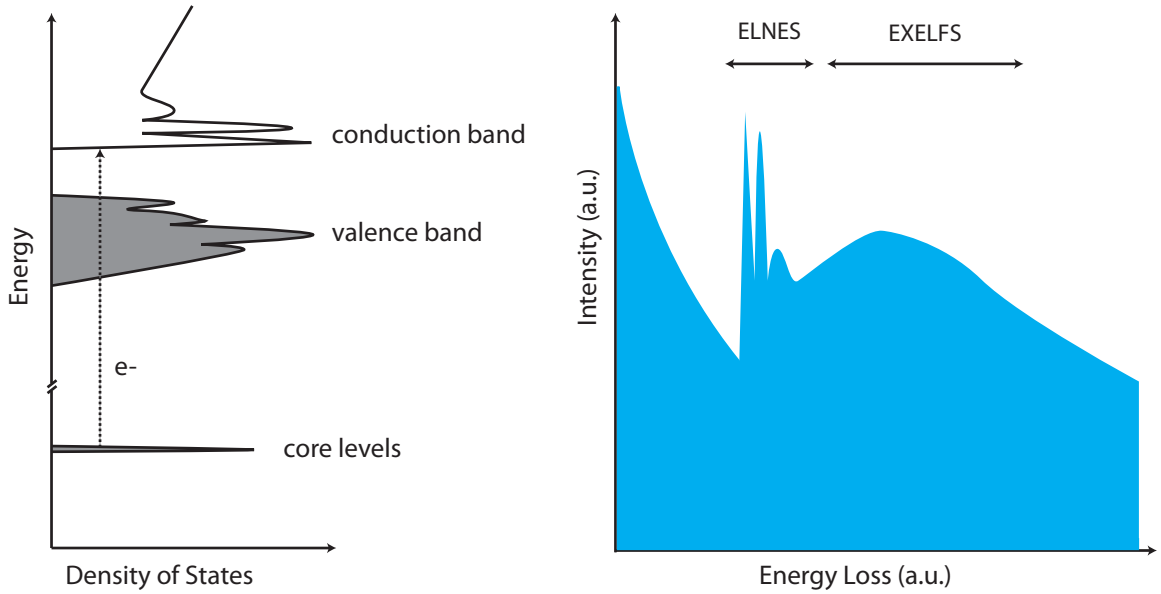

Figure 1.6: Schematic demonstrating how EELS probes the unoccupied density of states with electronic transitions from sharp core loss levels. Occupied states are indicated with gray shading in the density of states plot. Electronic transitions from the core levels to the empty conduction band causes probe electrons to lose energy, resulting in the EELS spectrum on the right.

seen going up in energy loss are those corresponding to the lowest energy electronic transitions in the material. If the material has a band gap, and the energy resolution of the microscope is good enough, one can see it as a gap between the zero loss peak and the next lowest energy features in the spectrum. Plasmons are also present in the low loss region, and are typically the dominant features of the region. The ratio of the zero-loss peak and the integrated plasmon energy-loss intensity gives a good indication of the thickness of the sample.

Features with energy losses above 100 eV are typically core-loss in nature, corresponding to transitions from core shell levels deep inside the atoms to the unoccupied states above the Fermi level as illustrated in Figure 1.6. The spectroscopic features produced by these transitions have a shape corresponding to the convolution of the core levels with the unoccupied densities of states, modulated by the quantum mechanical rules governing electronic transitions. Because the shape tends to be more complicated than a simple peak, the energy at which transitions from a given set of core levels begins is called an edge. The term edge is also used to refer to all the features coming from transitions from the same narrow set of core levels of the same principle quantum number and orbital angular momentum. Edges corresponding to transitions from core levels with principal quantum number $n = 1, 2, 3, 4$ are called K, L, M and N edges respectfully. A numerical subscript is used to indicate the different edges coming from the same quantum numbers. Core states with nonzero angular momentum tend to be spit by the spin-orbit interaction. So, for instance, instead of having just one edge from the $2p$ core levels ($l = 1$) we get two, one from the $2p_{1/2}$ (i.e. total angular momentum $j = 1 - 1/2 = 1/2$) which is called the L_2 edge and one from the $2p_{3/2}$ called the L_3 edge. As the splitting is small on the scale of hundreds of eV, it is common to refer to the EELS features from these split transitions as part of the same edge. So one will often refer to the L_2 and L_3 edges collectively as the L_{23} edge.

Each element has a different set of core levels giving rise to characteristic edges. These presence of these edges can be used to identify the chemical identity of the atoms in a material. With enough spatial localization of both the edge and the probe,

Table 1.1: Naming conventions used to describe edges corresponding to transitions from different core states.

Core state	Spectroscopic name
$1s$	K
$2s$	L_1
$2p_{1/2}$ and $2p_{3/2}$	L_{23}
$3s$	M_1
$3p_{1/2}$ and $3p_{3/2}$	M_{23}
$3d_{3/2}$ and $3d_{5/2}$	M_{45}
$4s$	N_1
$4p_{1/2}$ and $4p_{3/2}$	N_{23}
$4d_{3/2}$ and $4d_{5/2}$	N_{45}
$4d_{5/2}$ and $4d_{7/2}$	N_{67}

the presence of different elements can be determined with atomic spatial resolution. Although changes in the Fermi level due to being placed in different materials can cause the exact energy of the core-loss edges to shift somewhat for an element, these material dependent shifts are typically only a few electron-volts, small on the scale of the typical separation of core-loss edges from different elements.

The fine structure of an EELS edge is divided into two regions as illustrated in Figure 1.6. The lowest energy features form the energy loss near-edge structure (ELNES), and are the most direct probe of the density of states and provides information about the local bonding environment such as the type of coordination and the valence. Further from the absorption edge threshold the effects of plural scattering start to dominate. The features in this region are called extended energy loss fine structure (EXELFS). Oscillations in the EXELFS caused by diffraction can also provide information about the crystalline structure, but the ELNES is the more direct route to probing the electronic structure. Plural scattering is also responsible for the background which goes as one over energy. The amount of plural scattering increases with sample thickness. Because the probability of single scattering events does not increase as quickly as it does for plural scattering, the thinner the sample, the better the signal to noise ratios.

Good signal to noise ratios are especially important when performing spectrum

imaging. In a spectrum image, spectra are recorded as a function of position. Typically, the spectra are recorded in a rectangular grid creating a three-dimensional data set of energy-loss intensity $I(x, y, E)$, allowing the strength of any spectroscopic features to be displayed as a function of position as an image. The most simple application of spectrum imaging is just to map the presence of different elements as a function of position. When this is done with a fine enough grid, it is possible to produce an atomic resolution spectrum image, separately resolving each type of atomic column. Such chemical mapping can be very useful when Z-contrast imaging is insufficient to determine the identity or location of all the atoms in a material. Light elements are often very difficult to detect against a background of much heavier atoms in ADF images. Dopants of similar Z to the host material can also be hard to identify with ADF imaging. With EELS spectrum imaging, one can image light atoms and dopants even when they are not apparent in the Z-contrast images. Furthermore, one can quantify the changes in chemical composition with EELS, detecting, for instance, non-stoichiometry and segregation. One can also map the changes in fine structure with atomic resolution, and use this information to draw conclusions about the electronic structure and bonding environment as a function of position. Caution must be used when interpreting spectrum images, however, as channeling and other dynamical diffraction effects can complicate the spatial dependence of the EELS signal [31, 32]. It is best to compare with the results of image simulations including such effects to avoid misinterpretation. Density functional theory simulations of fine structure can also be used to compliment experimental results, and confirm interpretations of the experimentally observed fine structure.

1.2 Density functional theory

The nanoworld is intrinsically quantum mechanical in nature. In order to truly understand the diverse effects observed in complex nanoscale materials requires quantum mechanical theories. DFT makes it possible to accurately calculate many of the properties of complex solids and molecules from quantum mechanical first-principles. It is said [4] that soon after Schrödinger's equation for the electronic wavefunction

had been shown to work extraordinarily well for simple systems such as He and H_2, P. M. Dirac declared the field of chemistry to be finished, its content being entirely encapsulated by Schrödinger's equation. He is also said [4] to have recognized, however, that in the vast majority of cases the equation was far too complex to be solved. By using the electron density as the fundamental variable rather than the many-body wavefunction, DFT greatly simplifies the mathematical problem, allowing even complex systems described by unit cells containing hundreds of atoms to be studied quantum mechanically.

The time-independent Schrödinger's equation is

$$\hat{H}\psi = E\psi, \tag{1.8}$$

where $\hat{H}$ is the Hamiltonian, ψ is the wavefunction and E is the energy of either an excited or ground state. For a single particle, the Hamiltonian reads

$$\hat{H} = -\frac{\hbar^2}{2m}\nabla^2 + V(r). \tag{1.9}$$

For a many-body system such as a crystal, the Hamiltonian is more complicated. If we consider that each charged particle can feel the Coulomb force from from all the others, the many body Schrödinger's equation can be written (using Gaussian units)

$$\hat{H}\Psi = -\frac{\hbar^2}{2m}\nabla^2\Psi + \sum_{i=1}^{N}\sum_{j=i+1}^{N}\frac{Z_i Z_J}{|\mathbf{r}_i - \mathbf{r}_j|}\Psi = E\Psi, \tag{1.10}$$

where Ψ is the many-body wavefunction depending on the positions $\mathbf{r}_i$ of all N charged particles. One can see how the number of cross terms quickly increases with the number of particles. Most systems of interest consist of too many electrons and ions for an exact solution to be found. Even the most simple solids are too complex for their wavefunctions to be solved for exactly with this equation and approximations must be made.

The first approximation to be made is based on the fact that the ions are much more massive than electrons. The electrons can therefore move far more quickly and

move into an instantaneous ground state for any given configuration of ions before the ions have a chance to move significantly. This justifies the Born-Oppenheimer approximation, in which the ions are kept fixed when calculating the wavefunction of a system. The ions can later be moved, and the most energetically favorable structure can be found by comparing the total energy of different configurations of ions in the Born-Oppenheimer approximation. The approximation allows for a significant simplification of the Hamiltonian. The electron-electron, ion-electron, and ion-ion interactions can now be separated and the Hamiltonian written as

$$\hat{H} = -\frac{\hbar^2}{2m_e}\nabla^2 + \frac{1}{4\pi\epsilon_0}\sum_{i=1}^{N_e}\sum_{j=i+1}^{N_e}\frac{e^2}{|\mathbf{r}_i - \mathbf{r}_j|} + \sum_{i=1}^{N_e}\sum_{k}^{N_i}\frac{eZ_k}{|\mathbf{r}_i - \mathbf{r}_k|} + \sum_{k=1}^{N_i}\sum_{l=k+1}^{N_i}\frac{Z_k Z_l}{|\mathbf{r}_k - \mathbf{r}_l|}, \quad (1.11)$$

where e is the charge of an electron, N_e is the number of electrons and N_i is the number of ions. When determining the electronic degrees of freedom, the last term is simply a constant. This is still a very difficult Hamiltonian to work with for systems with more than a single electron, and further approximations are needed.

The most simple many body ansatz one could use to simplify matters is the Hartree approximation which assumes the many electron wavefunction to be a linear combination of orthonormal single particle wavefunctions:

$$\Psi = \psi_1(\mathbf{r}_1)\psi_2(\mathbf{r}_1)\cdots\psi_N(\mathbf{r}_N) \quad (1.12)$$

Using this form with the Schrödinger equation gives the Hartree equations:

$$\left[-\frac{\hbar^2}{2m_e}\nabla^2 + V_{\text{ions}}(\mathbf{r}_i) + V_i^H(\mathbf{r}_i)\right]\psi_i = \epsilon_i\psi_i(\mathbf{r}); \quad V_i^H(\mathbf{r_i}) = \sum_{j\neq i}\langle\psi_j|\frac{e^2}{|\mathbf{r}_i - \mathbf{r}_j|}|\psi_j\rangle, \quad (1.13)$$

which can be solved iteratively.

The Hartree approximation, however, ignores the fermionic nature of electrons. In order to satisfy the Pauli exclusion principle, the many-body wavefunction must be antisymmetric with respect to the exchange of any two electron positions. For

instance if we have electrons at positions $\mathbf{r}_1$ and $\mathbf{r}_2$, their wavefunction must satisfy

$$\Psi(\mathbf{r}_1, \mathbf{r}_2) = \Psi(\mathbf{r}_2, \mathbf{r}_1). \tag{1.14}$$

Hartree-Fock theory achieves this antisymmetry by expressing the wavefunction as a determinant of N orthonormal orbitals (ψ_i) as

$$\Psi(\mathbf{r}_1, \mathbf{r}_2, \ldots, \mathbf{r}_N) = \begin{vmatrix} \psi_1(\mathbf{r}_1) & \psi_1(\mathbf{r}_2) & \cdots & \psi_1(\mathbf{r}_N) \\ \psi_2(\mathbf{r}_1) & \psi_2(\mathbf{r}_2) & \cdots & \psi_2(\mathbf{r}_N) \\ \vdots & \vdots & \ddots & \vdots \\ \psi_N(\mathbf{r}_1) & \psi_N(\mathbf{r}_2) & \cdots & \psi_N(\mathbf{r}_N) \end{vmatrix}. \tag{1.15}$$

Because of the antisymmetry of the determinant, this wavefunction satisfies the Pauli exclusion principle For instance, in the two electron system

$$\Psi(\mathbf{r}_1, \mathbf{r}_2) = \begin{vmatrix} \psi_1(\mathbf{r}_1) & \psi_1(\mathbf{r}_2) \\ \psi_2(\mathbf{r}_1) & \psi_2(\mathbf{r}_2) \end{vmatrix} = - \begin{vmatrix} \psi_1(\mathbf{r}_2) & \psi_1(\mathbf{r}_1) \\ \psi_2(\mathbf{r}_2) & \psi_2(\mathbf{r}_1) \end{vmatrix} = -\Psi(\mathbf{r}_2, \mathbf{r}_1). \tag{1.16}$$

Using the Hartree-Fock many body wavefunction and Schrödinger's equation gives the Hartree-Fock equations:

$$\left[-\frac{\hbar^2}{2m_e}\nabla^2 + V_{\text{ions}}(\mathbf{r}_i) + \sum_{j \neq i} \langle \psi_j | \frac{e^2}{|\mathbf{r}_i - \mathbf{r}_j|} | \psi_j \rangle \right] \psi_i - \sum_{j \neq i} \langle \psi_j | \frac{e^2}{|\mathbf{r}_i - \mathbf{r}_j|} | \psi_i \rangle \psi_j = \epsilon_i \psi_i(\mathbf{r}). \tag{1.17}$$

These equations are the same as the Hartree equations except for the appearance of the extra term

$$- \sum_{j \neq i} \langle \psi_j | \frac{e^2}{|\mathbf{r}_i - \mathbf{r}_j|} | \psi_i \rangle \psi_j. \tag{1.18}$$

due to enforcing the behavior under exchange demanded by the Pauli exclusion principle.

The Hartree-Fock method works perhaps surprisingly well considering the approximations made. In the Hartree-Fock approximation, each electron sees the *average*

position of all the others, when they should be responding to the actual instantaneous location of the other electrons. In other words, the electron motions should be correlated, and in Hartree-Fock, they are not, causing significant errors in total energies. So called post-Hartree-Fock methods extend the method to include correlation effects. Basic Hartree-Fock calculations, however, already scale poorly with the number of electrons, and these post-Hartree-Fock methods scale even more poorly.

Density-functional theory provides a means of addressing the lack of correlations with far less computational difficulty than Hartree-Fock. The underlying concept is to work with the electron density $n(\mathbf{r})$ rather than the many-body wavefunction $\Psi(\{r_i\})$. Hohenberg and and Kohn first showed [1] that given an external potential $V(\mathbf{r})$, the groundstate density $n(\mathbf{r})$ is unique to within an irrelevant additive constant. Since the density

$$n(\mathbf{r}) = N \int \Psi^*(\mathbf{r}, \mathbf{r_2}, \ldots, \mathbf{r_N}) \Psi(\mathbf{r}, \mathbf{r_2}, \ldots, \mathbf{r_N}) d\mathbf{r_2} \ldots \mathbf{dr_N} \tag{1.19}$$

the potential $V_1(\mathbf{r})$ corresponds to the groundstate Ψ_1 and the energy

$$E_1 = \langle \Psi_1 | \hat{H}_1 | \Psi_1 \rangle = \int V_1(\mathbf{r}) n(\mathbf{r}) d\mathbf{r} + \langle \Psi_1 | T + U | \Psi_1 \rangle, \tag{1.20}$$

where $\hat{H}_1 = V_1 + T + U$ and T and U are the kinetic and electron-electron interaction energy operators.

Suppose a second potential $V_2(\mathbf{r})$ not equal to $V_1(\mathbf{r})$ plus a constant with groundstate $\Psi_2 \neq e^{i\phi}\Psi_1$ produces the same density $n(\mathbf{r})$. Then the energy of this second groundstate would be

$$E_2 = \langle \Psi_2 | \hat{H}_2 | \Psi_2 \rangle = \int V_2(\mathbf{r}) n(\mathbf{r}) d\mathbf{r} + \langle \Psi_2 | T + U | \Psi_2 \rangle. \tag{1.21}$$

Assuming non-degenerate wavefunctions, the Rayleigh-Ritz theorem implies that if

Ψ is the groundstate wavefunction for a Hamiltonian the energy of any other wavefunction used with this Hamiltonian will be higher:

$$E = \langle\Psi|H|\Psi\rangle < \langle\Psi'|H|\Psi'\rangle = E'. \tag{1.22}$$

Using this principle,

$$E_1 < \langle\Psi_2|H_1|\Psi_2\rangle = \int V_1(\mathbf{r})n(\mathbf{r})d\mathbf{r} + \langle\Psi_2|T+U|\Psi_2\rangle \tag{1.23}$$

$$= E_2 + \int [V_1(\mathbf{r}) - V_2(\mathbf{r})]n(\mathbf{r})d\mathbf{r} \tag{1.24}$$

and similarly

$$E_2 < E_1 + \int [V_2(\mathbf{r}) - V_1(\mathbf{r})]n(\mathbf{r})d\mathbf{r}, \tag{1.25}$$

but then adding these two together results in the contradictory statement that

$$E_1 + E_2 < E_1 + E_2. \tag{1.26}$$

Therefore, by *reductivo ad absurdum* there cannot be two potentials differing by more than a constant giving the same density. The proof has been extended to also apply to degenerate groundstates [33]. As the external potential uniquely determines the wavefunction to within an irrelevant phase factor, the link between the density and the potential also means the density determines the wavefunction.

Instead of directly solving the Schrödinger equation, one could arrive at the solution by applying the Rayleigh-Ritz theorem and finding the wavefunction $\tilde{\Psi}$ which produces the smallest energy

$$\tilde{E} = \langle\tilde{\Psi}|H|\tilde{\Psi}\rangle. \tag{1.27}$$

The wavefunction that does this will also be the solution to the Schrödinger equation, Ψ. For the set of trial wave functions $\tilde{\Psi}^{\alpha}_{\tilde{n}}$ that produce a density $\tilde{n}(\mathbf{r})$, the minimum energy for a given potential is

$$E[\tilde{n}(\mathbf{r})] = \min_{\alpha}\left[\langle\tilde{\Psi}^{\alpha}_{\tilde{n}}|H|\tilde{\Psi}^{\alpha}_{\tilde{n}}\rangle\right] = \int V(\mathbf{r})\tilde{n}(\mathbf{r}) + F[\tilde{n}(\mathbf{r})] \tag{1.28}$$

where

$$F[\tilde{n}(\mathbf{r})] = \min_{\alpha} \left(\langle \tilde{\Psi}^{\alpha}_{\tilde{n}} | T + U | \tilde{\Psi}^{\alpha}_{\tilde{n}} \rangle \right) \tag{1.29}$$

is a universal functional of the density, requiring no explicit knowledge of $V(\mathbf{r})$. The ground state energy is then

$$E = \min_{\tilde{n}} E[\tilde{n}(\mathbf{r})] = \min_{\tilde{n}} \left\{ \int V(\mathbf{r}) \tilde{n}(\mathbf{r}) + F[\tilde{n}(\mathbf{r})] \right\} \tag{1.30}$$

This implies that if such a universal functional $F[n]$ could be found and written without reference to the many-body wavefunction, one could find the exact total energy of a system without actually calculating its many-body wavefunction. As long as one can find the right density, one can obtain the total energy. This means that it is possible to find the total energy using an auxiliary system of fictitious non-interacting particles moving in an effective potential which reproduces the density of the real many-body system. Kohn and Sham [2] developed a set of equations for just such a set of auxiliary non-interacting quasi-electrons. They started by defining the functional

$$F[n(\mathbf{r})] = T_s[\mathbf{r}] + \frac{e^2}{2} \int \frac{n(\mathbf{r}) n(\mathbf{r}')}{|n(\mathbf{r})} d\mathbf{r} d\mathbf{r}' + E_{xc}[n(\mathbf{r})] \tag{1.31}$$

in which

$$T_s[\mathbf{r}] = \sum_i \langle \psi_i | - \frac{\hbar^2}{2m_e} \nabla^2 | \psi_i \rangle \tag{1.32}$$

is the kinetic energy of the single particle states and the last term $E_{xc}[n(\mathbf{r})]$ is called the exchange-correlation energy functional. To find the energy minimizing density they derived from this using the constraint that the total number of electrons is a constant, the Euler-Lagrange equations

$$\delta E[\tilde{n}(\mathbf{r})] = \int \delta \tilde{n}(\mathbf{r}) \left\{ V_{eff}(\mathbf{r}) + \frac{\delta}{\delta \tilde{n}(\mathbf{r})} T_s[\tilde{n}(\mathbf{r})]|_{\tilde{n}(\mathbf{r})=n(\mathbf{r})} - \epsilon \right\} d\mathbf{r} = 0 \tag{1.33}$$

where

$$V_{\text{eff}}(\mathbf{r}) = V(\mathbf{r}) + \int \frac{n(\mathbf{r}')}{|\mathbf{r} - \mathbf{r}'|} d\mathbf{r}' + V_{xc} \tag{1.34}$$

and the exchange-correlation potential

$$V_{xc} = \frac{\delta E_{xc}[n(\mathbf{r})]}{\delta n(\mathbf{r})}. \tag{1.35}$$

From the Euler-Lagrange equations they saw that the energy minimizing density is found by self-consistently solving the single particle equations

$$\left[-\frac{\hbar^2}{2m_e}\nabla^2 + V_{\text{eff}}(\mathbf{r})\right]\psi_i(\mathbf{r}) = \epsilon_i\psi_i(\mathbf{r}), \tag{1.36}$$

with

$$n(\mathbf{r}) = \sum_{j=1}^{N} |\psi_j(\mathbf{r})|^2, \tag{1.37}$$

which are now known as the Kohn-Sham equations. Figure 1.7 presents a flow chart showing how the Kohn-Sham equations are solved self-consistently with a planewave basis.

If the exchange-correlation functional $E_{xc}[n(\mathbf{r})]$ were known exactly, it would be possible to compute exact many-body total energies with this method. Unfortunately, for most systems of interest, no exact form is known, and we must rely on approximate functionals. One system for which the functional can be calculated precisely is the homogenous electron gas. All the approximations in use today are based on the calculation of the energy of the gas as a function of density. The simplest approximation is the local-density approximation (LDA), in which $E_{xc}[n(\mathbf{r})]$ depends on the density only locally. For an electron at point $\mathbf{r}$ it is equal to the exchange-correlation energy for an electron in a homogeneous electron gas with the same density. The interaction should however be nonlocal, so it is surprising the LDA works as well as it does. In an effort to more accurately portray the exchange-correlation functional, a slightly less local approximation called the generalized-gradient approximation (GGA) was developed. The GGA $E_{xc}[n(\mathbf{r})]$ depends not just on the density at $\mathbf{r}$, but on it's gradient [34]. The GGA tends to improve the accuracy of DFT calculations somewhat, but at some computational cost due to the extra complexity. Different parameterizations of $E_{xc}[n(\mathbf{r})]$ are available, and improving it is an active area of research. Even with

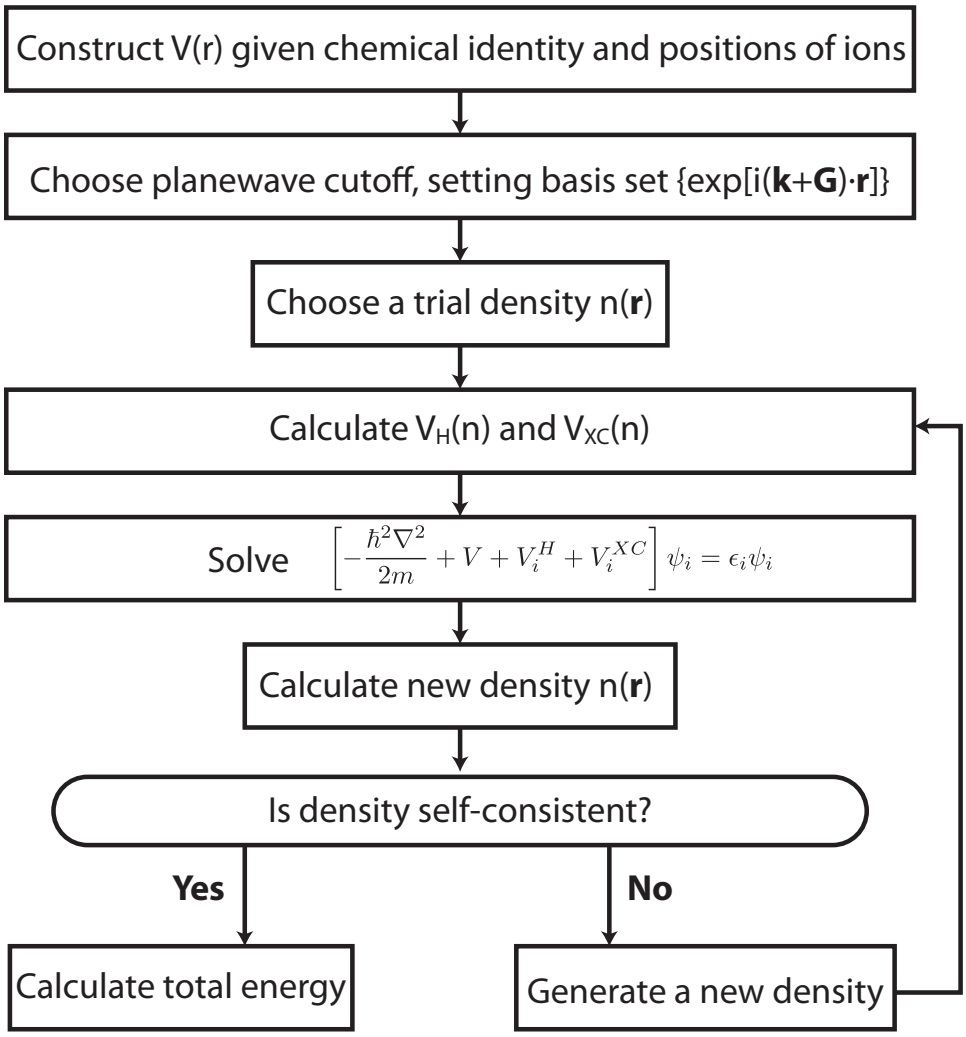

Figure 1.7: Flow chart documenting the procedure for computing the total energy of a material using DFT with a planewave basis.

these quite local approximations, DFT has provided a remarkably accurate means of simulating materials quantum mechanically. Because of its computational cost effectiveness, it has opened the doors to understanding a plethora of materials which would have otherwise been out of the reach of quantum mechanical simulations. The value of DFT was recognized with the awarding of the Nobel prize to W. Kohn for his work developing DFT and J. A. Pople for pioneering development of ab-initio software using Gaussian basis sets.

The most natural basis set in which to set about solving the Kohn-Sham equations for crystals is a plane wave basis. From Bloch's theorem the wavefunctions of a crystal can be written as the product of a cell-periodic function and a plane wave

$$\psi_i = \exp(i\mathbf{k}\cdot\mathbf{r}) f_i(\mathbf{r}). \tag{1.38}$$

The cell-periodic function can be expanded as a series of plane waves

$$f_i(\mathbf{r}) = \sum_{\mathbf{G}} c_{i,\mathbf{G}} \exp(i\mathbf{G}\cdot\mathbf{r}) \tag{1.39}$$

in which the $\mathbf{G}$ vectors are reciprocal lattice vectors. So we can write the wavefunction as a sum of plane waves

$$\psi_i(\mathbf{r}) = \sum_{\mathbf{G}} c_{i,\mathbf{k}+\mathbf{G}} \exp(i(\mathbf{k}+\mathbf{G})\cdot\mathbf{r}) \tag{1.40}$$

Only certain values of $\mathbf{k}$ are allowed by the periodic boundary conditions, however there are an infinite number of these allowed "k-points". The infinitely large number of electrons in a crystal are accounted for by a finite set of electronic states at an infinite number of k-points. Fortunately, wavefunctions are very similar at nearby $\mathbf{k}$, and a wavefunction at single k-point can be used to well represent the wavefunctions over a whole region of k-space. Methods have also been devised to take advantage of symmetry making it possible to use only a small set of special k-points to provide an accurate representation [35]. In a real DFT calculation, convergence must be achieved with respect to the number of k-points.

The plane wave basis forms a complete set which could in principle provide an exact representation of the wavefunctions. The completeness is, however, broken if the number of plane waves is less than infinite. Fortunately, only a good representation is needed, and the sum over $\mathbf{G}$ vectors can be truncated and still provide an adequate representation of the cell-periodic part of the wavefunctions. It is usual to converge the wavefunctions in terms of a planewave energy cut-off, which determines the number of plane waves included in the calculation through their kinetic energy $(\hbar^2/2m)|\mathbf{k}+\mathbf{G}|$.

The required number of plane waves increases with the fineness of the features of the wavefunctions. As the core wavefunctions of the atoms tend to oscillate rapidly they are poorly suited to expansion with plane waves. Since the core electrons do not usually contribute significantly to the physical properties of solids, they are typically removed. The core electrons screen the nuclear potential, and to compensate for their absence a weaker pseudopotential is used [36, 3]. As illustrated in Figure 1.8, pseudopotentials are designed such that they match the full ionic potential outside of a cutoff radius r_c, and such that they produce a smooth wavefunction inside that radius. The smoothness of the wavefunction resulting from using a pseudopotential allows one to use a lower planewave energy cut-off, greatly reducing the computational cost of the calculations.

The main feature of DFT is the calculation of total energies. By comparing the total energies of different atomic configurations, one can determine what structures are most energetically favorable. Interatomic forces can be calculated from the variation in the total energy, allowing structures to be "relaxed" to the lowest energy configuration. The forces can also be used to simulate the effects of temperature using methods such as Car-Parrinello molecular dynamics. DFT can be used to compute electronic structure in varying degrees of approximation. Time-independent DFT is strictly speaking a ground state theory, and in order to get very precise excited state properties time-dependent DFT (TDDFT) is really needed. Despite this, a great deal of excited-state physics can be extracted from time-independent DFT results. For instance, band structure can be obtained from time-independent DFT. This approximation results in some systematic errors, such as band-gap underestimation, but

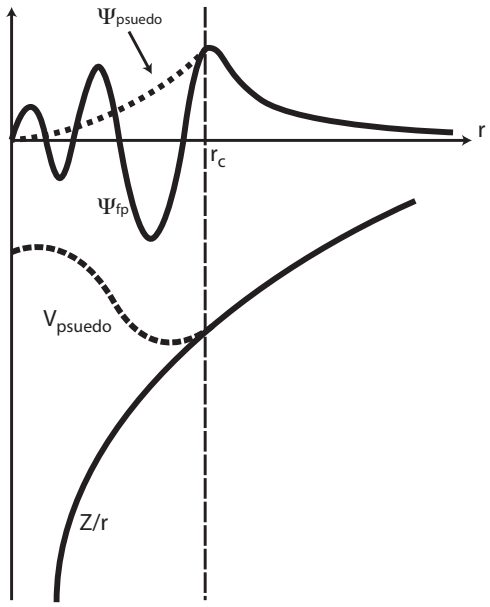

Figure 1.8: Schematic comparing a pseudopotential to the full ionic potential and the pseudowavefunction to the all-electron wavefunction as a function of the distance from the center of the ion.

when these are kept in mind the results are still very useful. Optical properties and EELS fine structure can be extracted as well. Both are more accurately simulated using TDDFT, but time-independent DFT is simpler and less computationally demanding. These features allow DFT to be used to interpret what is observed in the microscope and to make predictions that can then be tested by looking at the real material with STEM, or other methods. The ensuing chapters will provide examples of using DFT and STEM to investigate and uncover the mysteries of materials.

CHAPTER II

ALUMINA

I started my DFT work with a project exploring the effects of Mg on the structure and optical properties of γ-Al_2O_3. The project was selected primarily to acquire experiance with total energy calculations, optimization with defect configurations and optical absorption spectra. A layer of alumina typically forms on aluminum surfaces, either naturally or intentionally by anodization. Although pure alumina is transparent in the visual range, the presence of impurities can cause it to become optically active. Mg is commonly used as an alloying element in heat-treated aluminum alloys. If Mg makes its way into the alumina surface layer, the appearance of the alloy can be affected. The presence of Mg in γ-alumina has been reported to cause darkening, mottling, and surface roughness [37, 38, 39, 40].

The γ-alumina structure is based on that of magnesium spinel ($MgAl_2O_4$). In spinel, Mg atoms occupy tetrahedral (T_d) sites, and Al atoms occupy octahedral (O_h) sites. In γ-alumina, Al atoms occupy both T_d and O_h positions, but in order to satisfy the stoichiometry of Al_2O_3, 11% of the sites are left vacant. These built in vacancies cause the alumina to act as a sponge for hydrogen [41], soaking up hydrogen when exposed to the atmosphere. Since I wished to simulate the material as exposed to the atmosphere, I performed our structural investigations with the lowest energy H-containing stoichometry, HAl_5O_8 [41].

I started by posing the following questions: Given that the γ-alumina structure is based on that of spinel, do dispersed Mg atoms occupy T_d sites in γ-alumina as in spinel, or are the O_h sites preferred, as in MgO? If Mg is present in the alumina will it stay dispersed, or will it aggregate in the bulk or on the surface? I constructed a 1 x 2 x 2 supercell based on one of the minimum volume γ-alumina unit cells [42], such that a single Mg atom placed in the supercell could be considered isolated. Performing structural relaxations, I found that the total energy was lower by 1.0 eV when the Mg atom was substituted for a T_d Al atom rather than an O_h Al atom (see Figure 2.1).

I then introduced two additional T_d Mg, spreading them far away from each other initially, then bringing them together one at a time into nearest neighbor T_d sites. A tenth of an eV was gained by moving one of the Mg atoms next to another, which was then lost when the third was brought in. However, having 6 T_d Mg together turns out to be 0.3 eV lower in energy than the configuration where they are evenly distributed throughout the supercell (Figure 2.2), suggesting that spinel nucleation is likely to occur under the right conditions.

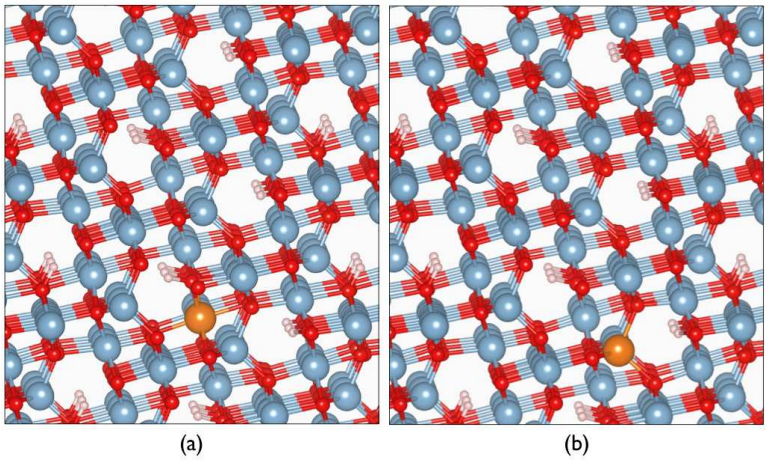

Figure 2.1: Bulk HAl_5O_8 γ-alumina with a single substitutional Mg impurity. Mg atoms are shown in orange, Al in blue, O in red and H in white. The Mg T_d position shown in (b) is 1.0 eV lower in energy than the O_h position shown in (a).

I then shifted my focus to the surface region. A supercell with the preferentially exposed (110)C surface [43, 44] was constructed with 10 Ångströms of vacuum. I found that the total energy was reduced by 0.3 eV when an isolated Mg atom was moved from a subsurface T_d site to a surface O_h site as shown in Figure 2.3. Moving the Mg atom to a surface T_d site resulted in an additional 0.4 eV reduction in total energy, suggesting that Mg impurities would migrate to the surface T_d sites.

To further study the migration of Mg atoms to the surface, I introduced additional Mg atoms into the subsurface region. Moving them to the surface one at a time, I found that migration to the surface was favored energetically until the surface T_d sites were half saturated with Mg. After this point, the Mg atoms preferred to stay in the subsurface. Unlike in the bulk, spinel nucleation at the surface therefore seems

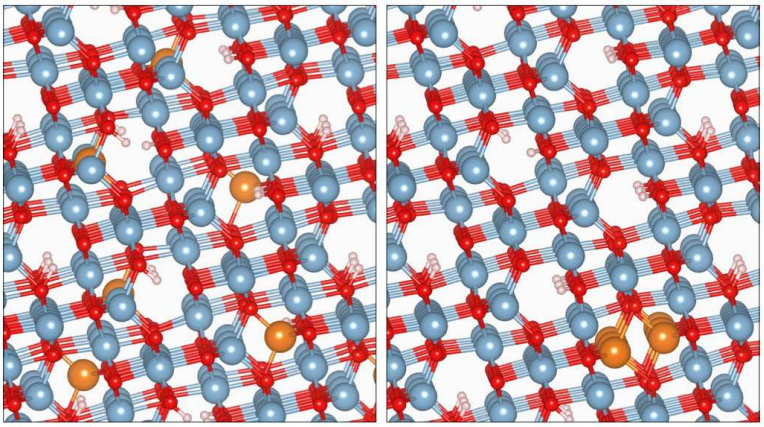

Figure 2.2: Bulk HAl_5O_8 γ-alumina with a six Mg impurity atoms. The clustering of Mg forming a pocket of Mg-spinel as shown in (a) is 0.3 eV lower in energy than the distribution shown in (a), indicating that spinel nucleation is energetically favorable in the bulk.

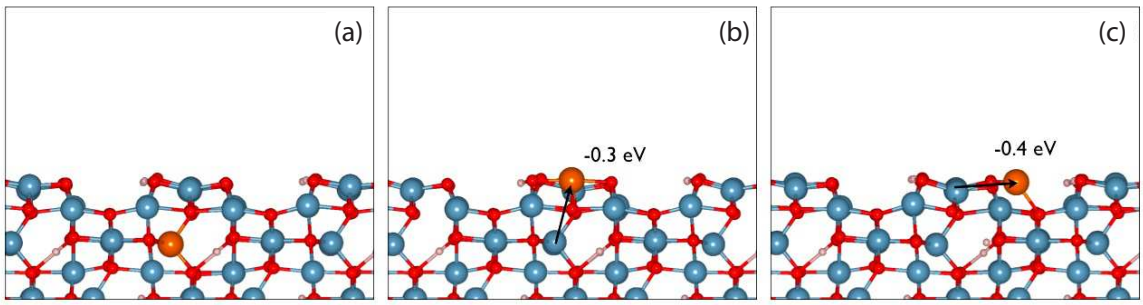

Figure 2.3: Moving a Mg atom from the subsurface T_d position shown in (a) into the surface O_h position shown in (b) decreases the total energy by 0.3 eV. Moving it from the O_h site to the surface T_d site shown in (c) decreases the energy a further 0.4 eV, making the surface T_d position 0.7 eV more energetically favorable than the subsurface.

unlikely. To further test for the possibility of spinel formation on the surface, I placed two unit layers of spinel on the alumina surface as shown in Figure 2.4(a). Upon relaxation, the spinel layers underwent a major reconstruction in which many of the Mg moved into O_h positions (Figure 2.4(b)). The increased propensity for Mg atoms to occupy O_h sites at higher concentrations suggests the possibility that MgO may nucleate at the surface in the presence of large numbers of Mg atoms. Uneven formation of MgO would be likely to cause the undesired surface roughening seen in Mg-Al alloys.

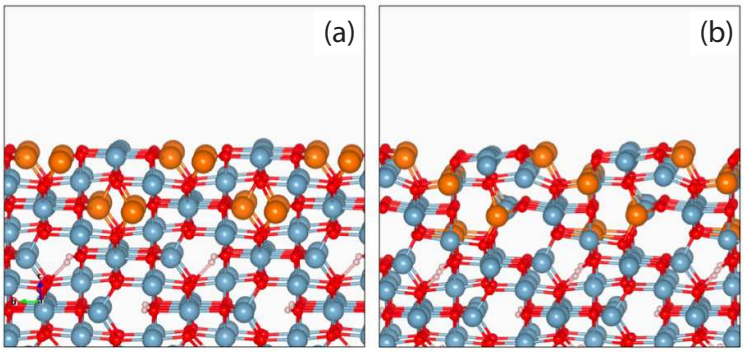

Figure 2.4: The layer of spinel on top of the γ-alumina shown in (a) undergoes a major reconstruction into the structure shown in (b) when allowed to relax. Notice the tendency for Mg atoms to move into O_h sites.

Having gained some insight into the behavior of Mg atoms in alumina, I began to explore the effects of the presence of Mg and H on the imaginary part of the dielectric function, ϵ_2. Figure 2.5(a) shows ϵ_2 calculated for bulk γ-HAl_5O_8, γ-Al_2O_3 and $MgAl_2O_4$. The HAl_5O_8 ϵ_2 is essentially unchanged from that of pure Al_2O_3. If there is an excess of H in the γ-Al_2O_3 structure, or equivalently an excess of Al in γ-$HAl_{5+1/3}O_8$, the material acquires a degree of metallicity. Figure 2.5(b) shows ϵ_2 calculated for γ-$HAl_{5+1/3}O_8$, undoped and with 1% and 2% dopings of Mg. A large spike in ϵ_2 occurs near zero eV, the tail of which extends all the way through the visual range. In Al_2O_3, the two 3+ Al atoms balance with the three 2- O atoms. In HAl_5O_8 the five 3+ Al atoms and the H atoms balance with the eight 2- O atoms.

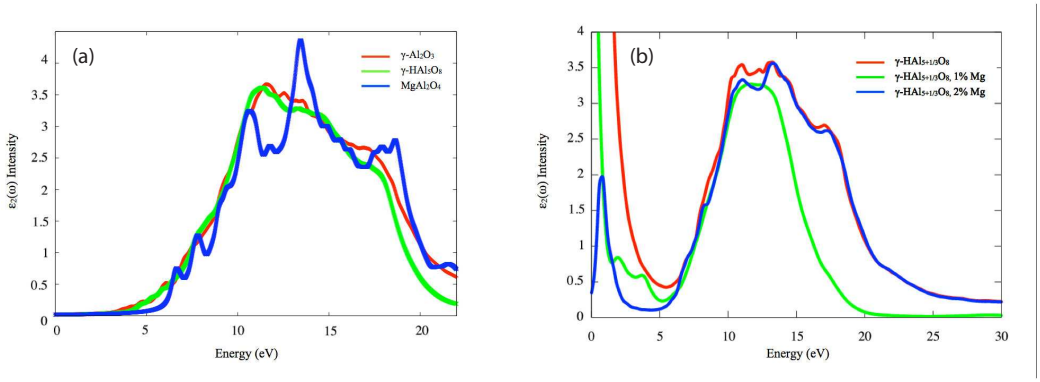

Figure 2.5: (a) Imaginary part of the dielectric function for bulk γ-HAl_5O_8, γ-Al_2O_3 and $MgAl_2O_4$. (b) Imaginary part of the dielectric function for bulk γ-$HAl_{5+1/3}O_8$, undoped and with 1% and 2% dopings of Mg.

In $HAl_{5+1/3}O_8$, however, the counting does not balance. The non-stoichiometry introduced electrons into the bottom of conduction band, which could then be excited higher into the conduction band, causing the low energy peak in ϵ_2. Replacing 3+ Al atoms with 2+ Mg atoms in tetrahedral positions reduced the number of "extra" electrons in the conduction band, which as shown in Figure 2.5(b) reduced the size of the low-energy peak.

From these studies it was apparent that the optical properties of the alumina are highly sensitive to the precise details of the doping. We did not pursue this project further.

CHAPTER III

COLOSSAL IONIC CONDUCTIVITY IN OXIDE MULTILAYERS

Ionic conductivity is essential to the operation of fuel cells and sensors. In a H fuel cell, O and H are supplied separately to an anode and cathode that are separated by an electrically insulating electrolyte ionic conductor. Chemical reactions occur that release electrons at the anode and consume electrons at the cathode, resulting in an electric potential difference which can be tapped to provide power. The role of the ionic conductor is to permit either H or O ions, depending on the type of fuel cell, to travel between anode and cathode so that they may react to form H_2O. As the rate at which fuel is delivered is limited by the ionic conductivity of the electrolyte, so too is the current output of the fuel cell. In solid oxide fuel cells (SOFCs), O_2 is reduced to O ions at the cathode, which are transported though a solid oxide electrolyte to the anode, where they react with H to form water and electrons. SOFCs are among the most efficient types of fuel cells, but typically require very high operating temperatures in order for their electrolytes to achieve sufficient levels of ionic conductivity. The most commonly used O conducting electrolyte is yttria stabilized zirconia $(Y_2O_3)_x(ZrO_2)_{1-x}$ (YSZ). It typically reaches usable levels of ionic conductivity only at temperatures in excess of 700° C [45, 46, 47, 48]. Such high temperatures tend to reduce durability, increase costs, and generally limit their application. As a result, the search has been on for alternative O electrolytes with higher ionic conductivities at lower temperatures.

Although progress has been made towards the goal of higher O ionic conductivites at lower temperatures in bulk materials such as $Ce_{1-x}M_xO_{2-\delta}$ (M: Sm, Gd, Ca, Mn), the greatest enhancements have been achieved in heterogenous superlattices. Following work in CaF_2-BaF_2 multilayers [49, 50], which showed an increase in the F ionic conductivity as the layer thickness was decreased, a variety of thin oxide heterostructures were fabricated. Enhancements of one to two orders of magnitude were achieved in (YSZ + 8.7 mol. % CaO)/Y_2O_3 [51] and YSZ/Y_2O_3 [52] multilayers and

over three orders of magnitude in highly textured YSZ thin films grown on an MgO substrate [53]. In these multilayer materials, the conductivity increased as the film thicknesses were decreased or when the number of interfaces was increased, indicative of an interfacial conduction pathway. It was proposed that in addition to space charge effects, the disordered and partially coherent interfaces of these multilayers enhanced the ionic conductivities by opening up pathways of decreased packing density [51, 52]. On the other hand, segregation in disordered areas such as grain boundaries oriented perpendicular to the O ion current could also block O transport. The lack of such blocking grain boundaries was attributed to the extra order of magnitude enhancement of ionic conductivity in YSZ grown on MgO [53, 54].

Two primary mechanisms have typically been invoked to account for large, so-called superionic conductivities. In the first case, there is a vacant sublattice that is unavailable to the mobile ion at low temperatures. As the temperature is increased, ions transfer randomly to the vacant sublattice and, at some critical temperature, an order-disorder phase transition sets in leading to a highly conducting disordered phase [55, 56]. This mechanism is often referred to as "sublattice melting". In the second case, ionic conduction is merely diffusion by the vacancy-mediated mechanism, *i.e.*, vacancy hopping [57, 56]. In the case of YSZ, instead of relying solely on temperature to produce vacancies, a supply of O vacancies results from replacing ZrO_2 units with Y_2O_3 units in the cubic fluorite lattice.

The greatest enhancements in O ionic conductivity were achieved by J. Santamaria and coworkers in YSZ/STO heterostructures [58]. The ionic conductivity of the 8 mol % yttria YSZ in these heterostructures was measured to be up to eight orders of magnitude higher than bulk YSZ between room temperature and 600 K. The magnitude of the enhancement led to the effect being dubbed colossal ionic conductivity. The conductivity increased with the number of interfaces, but only slowly with the YSZ layer thickness up to 30 nm, suggesting that the majority of O conduction was occurring in the interface region.

The STEM images and x-ray experiments reported by Garcia-Barriocanal et al.

[58] showed the YSZ/STO interfaces possessing colossal ionic conductivity to be coherent and atomically flat, with the YSZ rotating 45° around the *c* axis and expanding 7% in-plane such that the two cation sublattices fit together perfectly. Although small strains had been shown to enhance the diffusion of O ions in molecular dynamics simulations of YSZ [59], it was previously thought that disorder would provide the greater enhancement [51, 52]. Strains as large as 7% had not, however, been considered. Based on lattice mismatch theory [60], one would not expect such large strains to be stable, yet Santamaria's group had produced coherent YSZ/STO interfaces despite the 7% mismatch. A coherent expansively strained material has the advantage of possessing a decreased packing density without the blocking effects of segregation or grain boundaries.

Using DFT simulations I found that colossal ionic conductivity can be explained in terms of a combination of lattice-mismatch strain and O sublattice incompatibility as follows: Using finite temperature dynamical simulations of bulk cubic zirconia with a built-in supply of O vacancies, I found that 7% strain completely changes the O sublattice. At high temperatures the oxygen structure becomes extremely disordered, so much so that by 2000 K the O sublattice appears completely random. At these high temperatures, the mean-square-displacement (MSD), and therefore the mobility, of the O atoms in the strained structure are greatly enhanced over the already superionic unstrained structure. The enhancement correlates with the degree of O disorder, but is not mediated by sublattice melting as no enhancement is observed without vacancies. The key to understanding the *low-temperature* colossal ionic conductivity lies in the finding that the incompatibility of the oxygen sublattices at the YSZ-STO interface, together with the 7% lattice-mismatch strain, cause an *extreme* O sublattice disorder at room temperature that is comparable to the disorder found in strained bulk vacancy-doped zirconia at 2000 K. It was therefore possible to use the high-temperature data to estimate the low-temperature conductivity of the strained multilayers to be greater than 10^6 times higher than in unstrained bulk zirconia. Finally, the present calculations provide an answer to the puzzle of the stability of the YSZ epitaxial films with 7% strain to thickness of up to 30 nm in an

apparent serious violation of lattice mismatch theory [60]. I found that a new phase exists with an optimum strain of ∼5.2%.

The calculations, including finite-temperature quantum molecular dynamics (MD) [61] were performed using density functional theory [1, 2] in the generalized-gradient approximation and the projector-augmented-wave method [62] with a plane-wave basis as implemented in the Vienna *ab initio* simulation package (VASP) code [63]. Supercells containing two unit layers of zirconia and three unit layers of STO were used for the multilayer calculations. The zirconia was expanded 7% such that the cation lattices fit together perfectly. The experimental STO layer was sufficiently thick that the middle atomic planes were not affected by the interfaces. As I could not include as many STO atomic planes in the calculations, I froze the positions of the atoms in the middle plane, allowing the rest of the planes to relax. Although this might force the STO to take on its bulk structure more quickly than in reality, it provided the necessary feature of preventing the interfaces from affecting each other through the STO. The height of the multilayer supercell was then varied using an in-plane width of one unit cell. The structures were relaxed with an energy cutoff of 343 eV and up to a $6 \times 6 \times 6$ Monkhorst-Pack k-point mesh centered at the Γ-point.

The energetically optimum height was then used as the starting point for finite-temperature MD simulations. As the colossal ionic-conductivity of the multilayers is observed in-plane, I used supercells made of three unit cells in the two lateral directions and two units cells high for bulk MD simulations. For the larger multilayer calculations I used supercells two unit cells by two unit cells wide, again with two and three unit layers of zirconia and STO respectively. MD calculations were performed using only the Γ-point in k-space, with an energy cutoff of 250 eV. Atomic motion time-steps of 3.6 fs were used so that no atom could travel further than 0.1 Å per time-step [64]. Bulk 0 K relaxations of single zirconia unit cells were performed using an energy cutoff of 250 eV and $8 \times 8 \times 8$ k-point meshes.

I first investigated the effect of the very large 7% expansive strain using simulated annealing for bulk cubic ZrO_2 from 2000 K to 0 K. In Figure 3.1 I show snapshots of the strained structure at three temperatures and compare them with the structure of

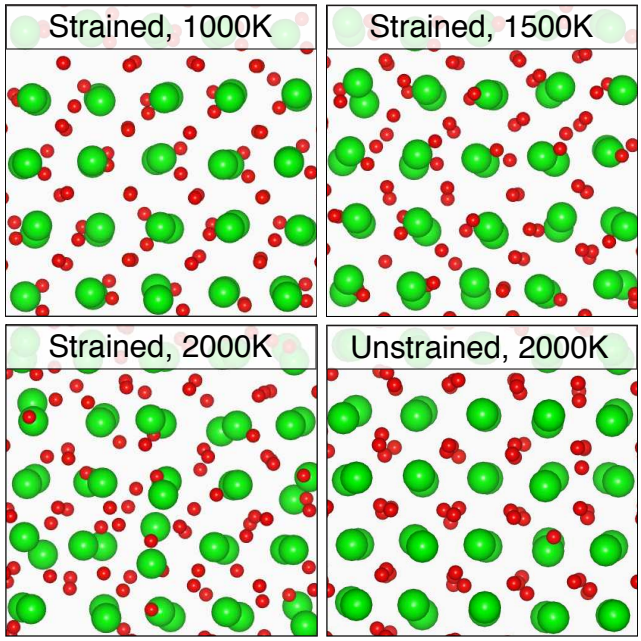

Figure 3.1: Zirconia structures resulting from quantum mechanical simulated annealing at various temperatures. O atoms are shown in red, and Zr atoms in green. The 7% expansive strain is in the plane of the page. The zig-zag ordering of the strained O sublattice shown at 1000 K persists down to 0 K, but begins to break down at higher temperatures. At 2000 K and above the O positions appear random, in contrast to the unstrained material in which most O atoms simply oscillate about the cubic-fluorite positions.

unstrained cubic ZrO_2 at 2000 K. It is evident that 7% strain results in a completely new O sublattice. At temperatures of 1000 K and below the O atoms are organized into zig-zags. The zig-zags are more complicated than the simple alternating O displacements seen in tetragonal zirconia. Furthermore, the O atoms in the strained zig-zag phase are in 7-fold coordination around the cations, as in amorphous ZrO_2 [65]. At higher temperatures, the O atoms are increasingly disordered until by 2000 K the zig-zags have completely disappeared and the O-sublattice appears totally amorphous. This result contrasts sharply with the unstrained structure in which even at 2000 K most of the O atoms display only Debye-Waller type oscillations about the cubic-fluorite tetrahedral positions (Figure 3.1).

The mobility of the O atoms was studied by calculating their thermal MSD as a function of time in MD calculations for up to 6 picoseconds (Figure 3.2). Without any

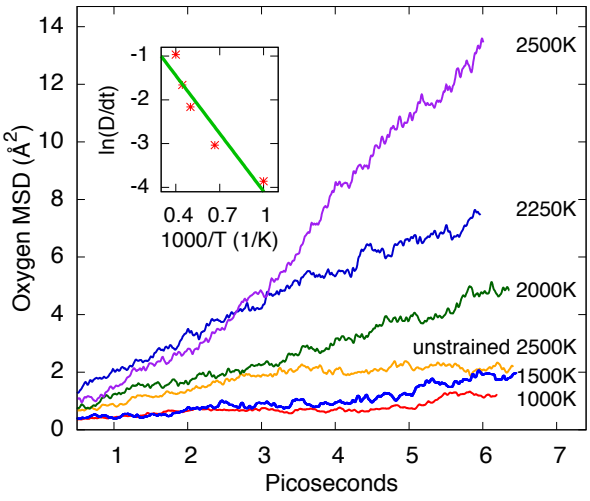

Figure 3.2: MSD of O atoms as a function of time during MD simulations at various temperatures. (Inset) Arrhenius plot of D from the strained MSDs (same units). The linear fit shown in green yields an energy barrier of 0.4 ± 0.1 eV.

vacancies, no net displacement occurs. Even with one vacancy per supercell at 2000 K, the superionic unstrained zirconia still produces no MSD on this timescale. Applying 7% strain to the zirconia with a single vacancy, however, I find that significant O MSD occurs as low as 1000 K. As no motion occurs without vacancies, the mobility is therefore not mediated by "sublattice melting" but by vacancy hopping.

With vacancies, the strained zirconia O MSD increases with temperature and correlates with the degree of disorder. At 1000 K and 1500 K, where a degree of zig-zag ordering remains, plateaus occur in the MSD corresponding to periods of time without hopping. At 2000 K and above, where the O sublattice appears random, the MSD increases continuously. The activation barrier extracted from an Arrhenius plot of the diffusivities (Figure 3.2 inset) is 0.4 ± 0.1 eV, smaller than the 0.6 eV reported by [58].

To investigate the role of the interface, I determined the structure down to 360 K by performing simulated annealing of the STO-YSZ multilayers starting from 1200 K, which is roughly the substrate temperature used during growth of the multilayers in the experiment. The result is shown in Figure 3.3. Unlike in the bulk strained zirconia, the O sublattice near the interface remains highly disordered all the way down to 360

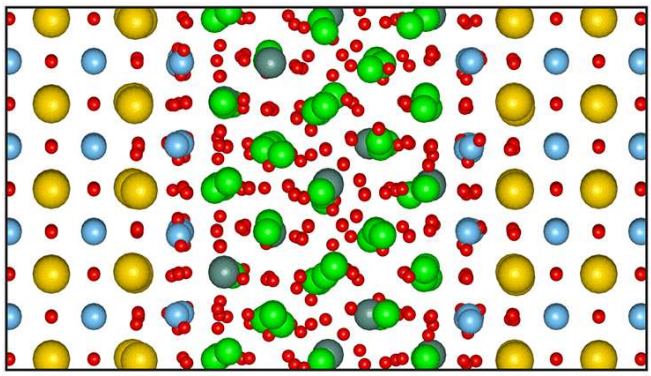

Figure 3.3: Structure of the 1 nm YSZ layer sandwiched between layers of STO at 360 K. Sr atoms are shown in yellow, Ti in blue, Zr in green, Y in gray, and O in red.

K. In fact the multilayer YSZ O sublattice appears to have the same degree of disorder at 360 K as the strained bulk at 2000 K. The presence of the interface therefore causes the high temperature phase with its very low hopping barrier to persist down to low temperatures.

As the disordered high temperature phase persists to low temperatures in the multilayer, the enhancement of the ionic conductivity in the multilayers over that of bulk YSZ could be estimated from the MSD calculations. Using the Einstein relation $\langle r^2 \rangle = 6Dt$ I obtained diffusivities from the MSDs. I was then able to solve for the pre-exponential D_0 in the expression for the diffusivity, $D = D_0 \exp(E_b/kT)$, in which E_b is the energy barrier, k is the Boltzmann constant, and T is the temperature. The value of D was then extrapolated to low temperatures. The Nernst-Einstein relation, $\sigma = Nq^2D/kT$, in which q and N are the charge and density of the mobile ions, was then used to obtain conductivities from diffusivities.

It was not feasible to obtain a reliable estimate of the absolute value of the conductivity of O vacancies because of a large uncertainty in the density and the fact that the charge on the ions is ill-defined. It was possible, however, to estimate the effective magnitude by evaluating the ratio of the conductivity in the strained disordered phase to that in the unstrained phase $\sigma_s/\sigma_b = D_s/D_b$, assuming the density and charge of the carriers to be the same in both phases. For the strained phase pre-exponential, I used the average of the pre-exponentials determined at each temperature a MSD was

calculated. As previously noted, the unstrained phase was not conductive enough to show any net motion even at 2000 K. By increasing the temperature to 2500 K, however, I was able to get a single MSD slope for the unstrained phase. As an energy barrier cannot be obtained from a single temperature, I used the 1.1 eV experimental energy barrier for the unstrained bulk material [58] in the expression for D_b. Using this method, I estimated the ionic conductivity of the strained disordered phase to be 4×10^6 times higher than that of unstrained bulk YSZ at 500 K, close to the eight orders of magnitude reported experimentally.

It is evident that the disorder induced by the strain and the presence of the interface are responsible for the majority of the observed colossal enhancement in ionic conductivity. In halide based multilayers such as BaF_2/CaF_2, space charge effects enhance ionic conduction up to about two orders of magnitude for thin layers [50]. Our estimate for the conductivity enhancement in the thin YSZ multilayers does not include space charge effects, so it may well be that space charge effects provides the last 1-2 orders of magnitude enhancement.

The results of the simulations also allowed us to gain further insights into the cause of the extreme O sublattice disorder in the YSZ layer of the multilayer structure. The O sublattice of bulk zirconia under 7% strain exhibits essentially the same zig-zag ordering as shown at 1000 K in Figure 3.1 all the way down to 0 K. It is this zig-zag-ordered sublattice that is juxtaposed with the STO O sublattice. The zig-zag ordered YSZ O atoms occupy sites that are close to tetrahedral positions. On the other hand, O atoms in STO occupy octahedral positions. Evidently, the incompatibility of the STO and YSZ O sublattices is causing the observed O disorder. Figure 3.3 shows that at 360 K there are relatively small O-atom displacements on the STO side of the interface. In contrast, because the YSZ is strained by 7%, the O sublattice is more flexible and succumbs to the perturbation, exhibiting extreme disorder. The stable STO structure controls the positions of the O atoms in the YSZ interfacial plane, forcing them all to occupy octahedral positions. This constraint then disturbs the O atoms in the underlying layers of YSZ, with no Ti neighbors, that are free to disorder.

I probed the above issue further by examining the energetics of O vacancies at the

YSZ interfacial plane. When one of the octahedral O atoms in the YSZ interfacial plane is removed and the structure relaxed, an O atom from further into the YSZ immediately moves to fill the octahedral vacancy. This preference for full occupation of the octahedral O positions at the interfacial plane is consistent with electron energy-loss spectra reported in [58] which shows no difference between the Ti oxidation state at the interface and deep within the STO. As long as there are O atoms occupying all the octahedral positions in the interfacial plane, the effect of the STO seems to only be felt through the displacement of neighboring O atoms. When vacancies are placed in positions away from the interfacial plane the vacancies do not relax to another layer. These results indicate that vacancy hopping, and therefore ionic conduction occurs preferentially in a region below the interfacial plane, where the O atoms are perturbed but unconstrained by the STO.

It is natural to infer that the extreme disorder seen at 360 K in the thin 1 nm YSZ O sublattice tapers off with distance from the interface in thicker layers of YSZ. Colossal conductivity, therefore, is likely to occur only in a relatively thin section of the YSZ layer adjacent to the interface. This thin disordered section would completely dominate the conductivity, resulting in the lack of variation in the conductance with YSZ thickness observed experimentally for 1-30 nm YSZ layers [58].

Increasing the YSZ layer thickness to 62 nm causes a three-orders-of-magnitude drop in the ionic conductivity, which was attributed to relaxation due to exceeding the critical thickness of the YSZ [58]. Lattice mismatch theory for epitaxial films, however, suggests that for 7% mismatch strain, the critical thickness ought to be extremely small [60], not on the scale of tens of nanometers. The present calculations resolve this quandary. The zig-zag structure resulting from simulated annealing in the strained bulk represents a new zirconia phase that becomes energetically favorable at high strains. Varying the in-plane strain of the zig-zag structure results in a parabolic dependence of the total energies centered around 5% strain. The total energy of the 5% strained zig-zag structure is only about 0.16 eV per unit cell higher than the total energy of the unstrained cubic fluorite structure. At 7%, the total energy of the zig-zag structure is 0.49 eV higher, but this is still 2.76 eV lower than the cubic fluorite

structure strained to the same dimensions. The phase change, therefore, reduces the energy penalty imposed by the strain, and allows the YSZ layer to remain coherently strained up to 30 nm. Once the strain is released the present calculations suggest that the ionic conductivity would drop significantly, as observed.

After publishing these DFT results [66], I turned to microscopy to support the findings. STEM and EELS measurements were performed on a Nion UltraSTEM operated at 100 kV using a cold field emission electron source, a corrector capable of neutralizing up to fifth order aberrations [18] and an Enfina EEL spectrometer. Some images were also obtained on a VG Microscopes HB501UX with a third order Nion aberration corrector (indicated in the figure caption). The YSZ/STO heterostructures were grown in a high oxygen pressure (3 mbar) pure O RF sputtering system and prepared in cross section or plan view geometry by conventional thinning, dimpling, and ion milling. The samples were tilted in the microscope to either the $\langle 100 \rangle$ or $\langle 110 \rangle$ cubic zone axis of STO. The principle component analysis (PCA) method of [67] was used to eliminate noise in atomic-resolution EELS elemental maps as described in [68].

EELS O K-edge fine structure simulations were performed using the $Z+1$ approximation [69, 70] . The calculations were carried out using DFT as implemented in the VASP code. For faster convergence with respect to the k-point sampling density and greater accuracy, the linear tetrahedron method with Blöechl corrections was used for Brillouin zone integrations [62].

Image simulations were carried out using a absorptive multislice STEM code [71] with absorption due to thermal diffuse scattering included using an Einstein Model [72]. The inelastic scattering coeffiecients for EELS were calculated using relativistically corrected Hartree Fock bound states and Hartree Slater continuum states [73]. An aberration free probe with a aperture semiangle of 30 mrad was assumed. Simulations were for a specimen thickness of approximately 110 Å with an EELS detector semiangle of 30 mrad. A Gaussian blur with a full width half maximum of 1 Å was applied to account for the finite source size.

Due to the propensity of YSZ to facet, growing flat coherent YSZ/STO thin

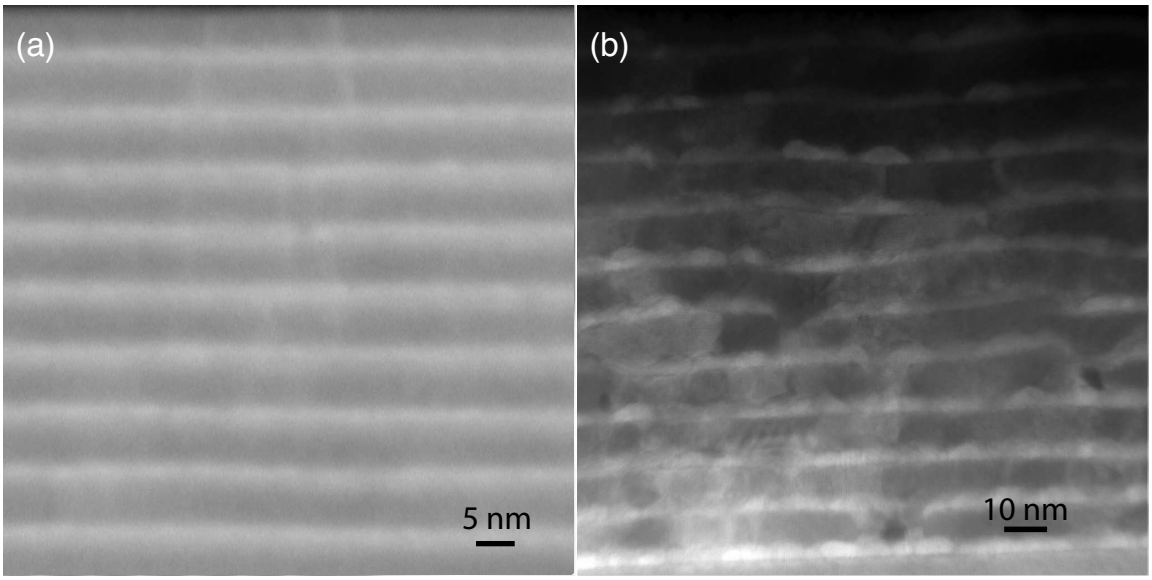

Figure 3.4: Low magnification ADF images of YSZ/STO thin film multilayers acquired on a VG Microscopes HB501UX. (a) Sample showing flat coherent multilayers grown in 2007. (b) Sample grown under slightly different growth conditions in 2009 showing incoherent layers.

film multilayers is quite challenging. Figure 3.4 shows low magnification annular dark field (ADF) images of two YSZ/STO samples, one grown in 2007 [58] and the other in 2009. Although both were grown using the same high pressure oxygen RF sputtering equipment under similar growth conditions, the layers in the 2007 sample are coherent and flat while those in the 2009 sample are not. Slight differences in the growth environment caused the YSZ in the 2009 sample to clump, facet, and bend. Dislocation cores formed at the interfaces, relieving the strain on the YSZ layers.

In an effort to recreate the coherent YSZ/STO multilayers grown in 2007, samples were grown with thinner nominal YSZ layer thicknesses. These samples often showed islanding, as shown in the high resolution ADF image shown in Figure 3.5, in which clumps of YSZ have formed surrounded on all sides by STO. They also possess coherent areas in which the YSZ is strained to match the STO, such as the area pointed to by the arrow in Figure 3.5(a) below the more obvious incoherent facet of the YSZ island. A similar island is shown in the high resolution ADF image shown in Figure 3.5(b) and in an ADF image (3.5(c)) recorded simultaneously with a spectrum image

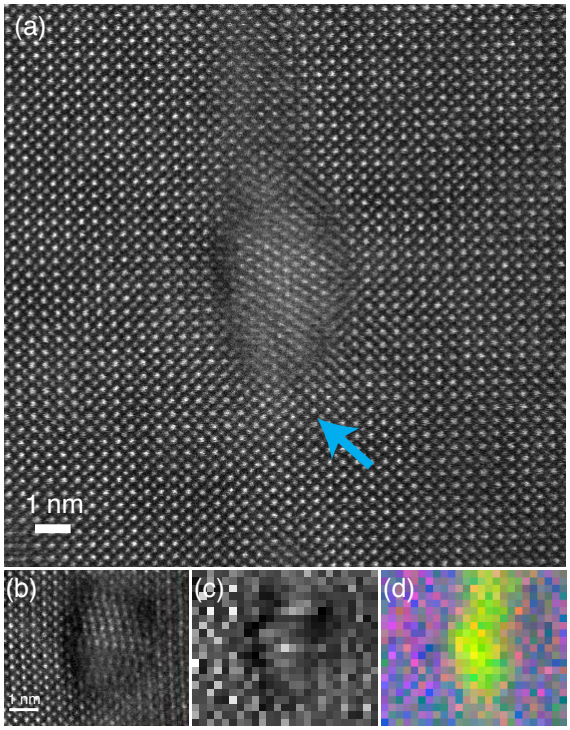

Figure 3.5: High resolution ADF images of islands of YSZ in STO are shown in (a) and (b). The arrow in (a) points to a section of coherent YSZ/STO. An elemental map created from a spectrum image of the the area imaged in (b) is shown alongside a simultaneously acquired ADF image (c) in (d). Red, green and blue channels of (d) are composed of the integrated intensities of the O K, Zr $M_{2,3}$ and $M_{4,5}$, and Ti $L_{2,3}$ edges respectively, causing STO to appear purple and YSZ yellow.

of the area used to create the elemental map shown in 3.5(d). The elemental map shows the integrated intensities of the O K, Zr $M_{2,3}$ and $M_{4,5}$, and Ti $L_{2,3}$ edges as the red, green and blue channels of the image. Integration windows of approximately 50, 180, and 25 eV were used for the O, Zr, and Ti signals respectively. The only other features that should affect the signal in the large integration window used for Zr are the Y $M_{4,5}$ and $M_{2,3}$ edges, but this was fine as I was interested in distinguishing YSZ from STO. Red and blue make purple while red and green make yellow, so STO will appear purple and YSZ yellow. The island is clearly zirconia.

Figure 3.6 shows coherent interfaces looking down the $\langle 100 \rangle$ and $\langle 110 \rangle$ axes of the STO. As the YSZ must rotate 45° to fit the STO cation lattice, these correspond to the $\langle 110 \rangle$ and $\langle 100 \rangle$ axes of the YSZ respectively. Intensity in ADF imaging varies

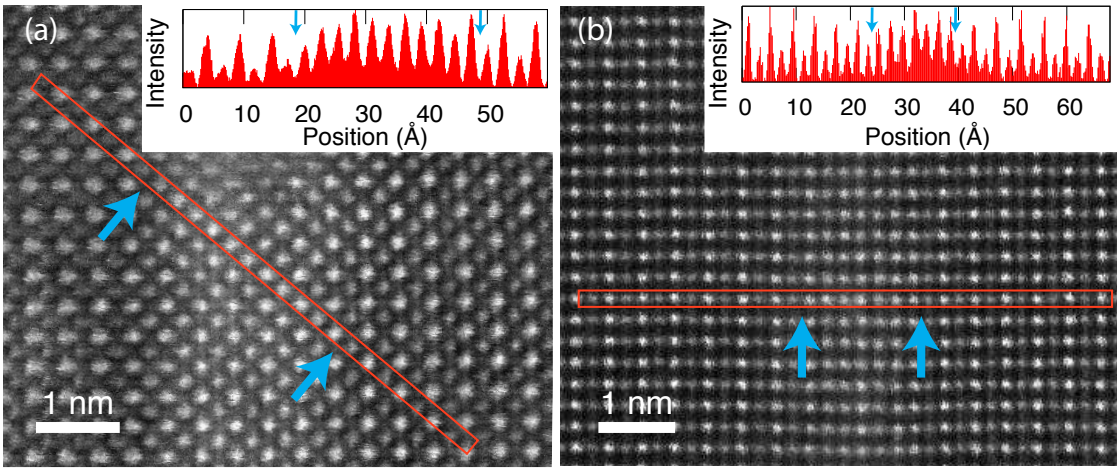

Figure 3.6: High resolution ADF images of sections of coherent regions of YSZ/STO multilayers looking down the STO ⟨100⟩ and YSZ ⟨110⟩ directions in (a) and the STO ⟨110⟩ and YSZ ⟨100⟩ in (b). ADF intensity is plotted as a function of position along the long direction of the red boxes for both images in the insets. The intensity is integrated along the direction of the short side of the red boxes. Blue arrows indicate the transition from consistently high intensity peaks to alternating bright dark peaks in the linetraces, corresponding to the transition from YSZ to STO. The corresponding positions on the images are also marked with arrows.

roughly as the square of the atomic number of elements being imaged. With atomic numbers 38, 39 and 40, respectively, Sr, Y and Zr are neighbors on the periodic table and will therefore appear similarly bright compared to Ti with atomic number 22. Against the background of these heavier atoms, the O columns are not readily discernible. STO therefore appears with equal numbers of bright and dark columns, while the YSZ columns all appear bright. Linetraces taken in the ⟨110⟩ directions of the images in Figure 3.6 show a series of bright columns surrounded by the alternating bright and dark columns, identifying the YSZ and STO. The areas of the images used in the linescans are delineated in the figure with red rectangles. Arrows mark the transitions between the alternating bright and dark columns of STO and the more consistently bright columns of the YSZ in the linescans and the corresponding points in the images. The width of the transition from YSZ to STO contrast is roughly one unit cell, consistent with the expected beam broadening for this sample thickness.

Figure 3.7(a) shows another section of coherent YSZ/STO layers. A spectrum

image (SI) was acquired, consisting of EEL spectra taken in a 4×24 pixel grid within the area shown in the yellow rectangle. An exposure time of 2 seconds was used for each pixel. During the acquisition of each pixel of the SI, the beam was scanned in a 16×16 pixel subgrid, allowing an ADF image (Figure 3.7(b)) to be recorded at higher spatial resolution simultaneously with the EELS SI. As sample drift almost always occurs during the long periods of time needed to record SIs, the higher resolution simultaneously recorded ADF image is useful in identifying exactly where the spectra were recorded. From Figure 3.7(b) it is clear that there was some sample drift down and to the left, but the STO is clearly discerned from the YSZ by its alternating bright and dark columns. A map of the Ti concentration created from the integrated background subtracted Ti L-edge is shown in Figure 3.7(c) at the same scale as the simultaneously recorded ADF. In the STO, bright rows are seen in the Ti map where darker Ti columns are seen in the ADF image. Near the interface, the Ti intensity begins to drop. Moving into the layer of more consistently bright atoms, the Ti intensity continues to decrease, supporting the identification of the layer as YSZ.

EELS fine structure reflects the local bonding environment. Changes in either bond-lengths or coordination shift or change the intensities of the fine structure features. In a disordered material, with many slightly different local bonding environments, the EELS spectrum is the sum of many slightly different fine structure features. One, therefore, expects the fine structure features of a disordered material to be blurred out in comparison to an ordered material. I illustrate this effect with DFT $Z+1$ O K-edge fine structure simulations for ordered cubic ZrO_2 and disordered O sublattice strained ZrO_2. For the ordered structure it is only necessary to calculate the $Z+1$ projected density of states for a single O site, as all the O sites are equivalent. To simulate the fine structure of the disordered material I summed the $Z+1$ projected density of states calculated for 6 different O atoms in the high temperature disordered O sublattice strained bulk structure produced by the MD calculations of reference [66]. Monkhorst-Pack k-point meshes of up to $18 \times 18 \times 18$ were used for the small ordered supercell and up to $4 \times 4 \times 4$ for the much larger disordered O sublattice structure. The resulting spectra were convolved with a 0.5 eV full width half

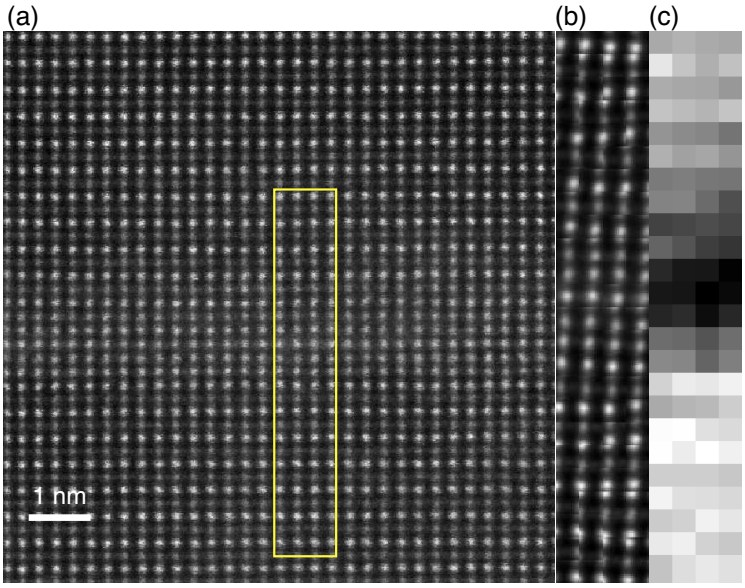

Figure 3.7: (a) High resolution ADF image of a ⟨100⟩ YSZ layer sandwiched between ⟨110⟩ STO layers. A SI was acquired from the area indicated by the yellow rectangle superimposed on (a). An ADF image recorded simultaneously with the SI is shown in (b) at the same scale as the Ti elemental map shown in (c). A drop in the Ti intensity correlates with the more consistently bright columns of the YSZ layer.

maximum Gaussian to facilitate comparison to experiment. The results are shown in Figure 3.8 normalized to the integrated intensity of the first 50 eV of the edges. The simulated fine structure features of the ordered structure correspond well to those seen in normal bulk YSZ. Shifts in the features of the projected density of states for each of the different $Z + 1$ sites used in the simulation for the disordered structure sum up to create a fine structure which appears much like a blurred version of the fine structure of the ordered structure. Where there are two peaks close together in the fine structure of the ordered material, there is a single broad peak for the disordered material.

In Figure 3.9(a) the YSZ O K-edge fine structure obtained from the spectrum image of the coherent region of the STO/YSZ multilayer shown in Figure 3.7 is compared to that obtained from bulk YSZ. From the simultaneously acquired ADF image it is easy to pick out which SI pixels are inside the YSZ layer. The spectrum shown in green in Figure 3.9(a) was created by summing over the 20 SI pixels corresponding

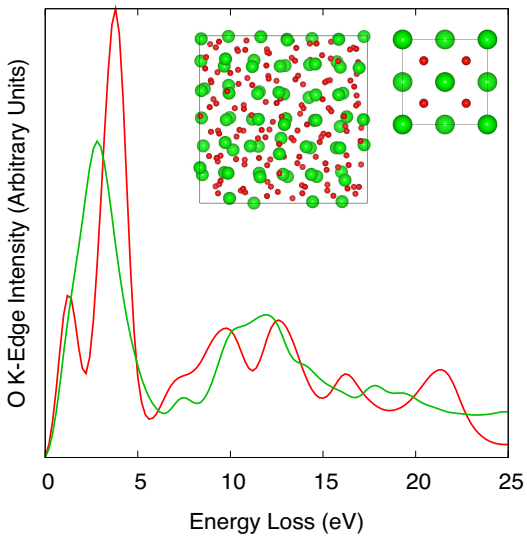

Figure 3.8: EELS O K-edge fine structure simulated using DFT and the $Z + 1$ approximation for bulk ordered cubic ZrO_2 (shown in red) and the 2000 K strained bulk structure with the extremely disordered O sublattice (shown in green). The energy loss is taken to be zero at the Fermi energy. Both spectra were normalized to the intensities integrated over the first 50 eV and broadened with a 0.5 eV Gaussian. It is seen that the disorder causes the fine structure to blur out.

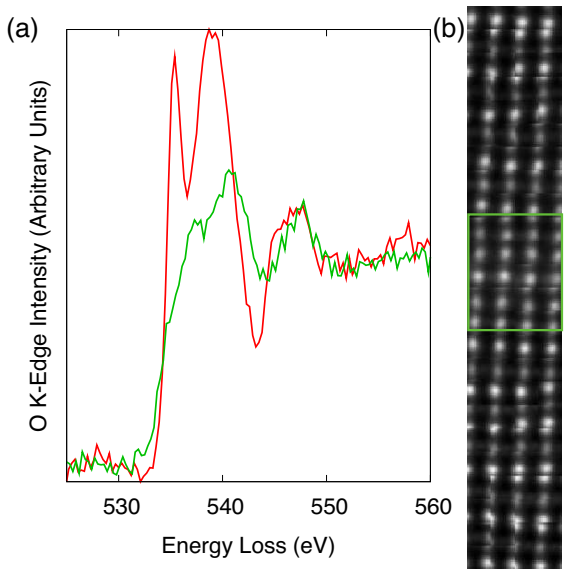

Figure 3.9: (a) O K-edge fine structure from the thin YSZ layer shown in Figure 3.7 plotted in green and from bulk cubic YSZ in red. The multilayer spectrum was created from the same spectrum image used to produce the Ti map in Figure 3.7. Pixels were summed up in the area corresponding to the green box superimposed on the simultaneous ADF image shown in (b).

to the area within the green box superimposed on the simultaneously acquired ADF image shown in Figure 3.9(b). With a per pixel exposure time of 2 seconds, this corresponds to a 40 second exposure, plenty of time for fine structure to dominate the noise, yet only broad peaks are seen. Compared to the spectrum from bulk YSZ, the multilayer spectrum appears blurred out just as predicted by theory for a structure with O disorder. It is likely there is some contribution to the multilayer spectrum from STO - the integrated Ti $L_{2,3}$ signal does not go to zero in the YSZ layer - but the spectrum does not appear to be a simple linear combination of YSZ and STO bulk fine structure. STO has a prominent prepeak at very nearly the same energy as bulk YSZ, yet the multilayer YSZ spectrum has only a weak strength in this region, supporting the view that the fine structure is blurred out due to O disorder in the YSZ.

Another way EELS can be used to search for disorder is through atomic-resolution elemental mapping. Images created from the integrated edge intensities of each pixel

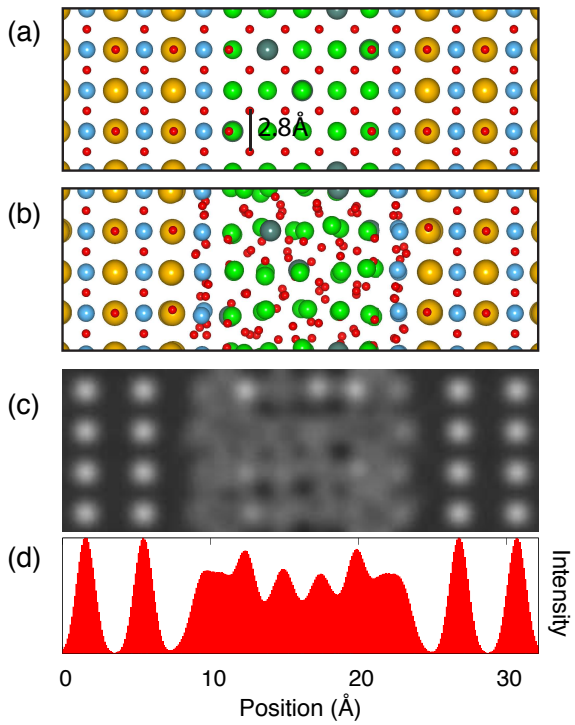

Figure 3.10: (a) Model of YSZ/STO multilayer with ordered strained YSZ O sublattice viewed such that the STO is seen down the ⟨110⟩ direction. In this orientation the pure O columns of STO can be resolved using high spatial resolution elemental mapping. The O columns of the strained ordered YSZ have the same 2.76 Å in plane separation as the pure O columns in STO in the vertical direction of the Figure and a slightly shorter 2.39 Å. As such, the YSZ O columns should be resolved in an elemental map, if O atoms are ordered. If they are instead disordered as in (b), then one would expect to see a highly blurred out structure or just a blur. The blurring out is illustrated in (c) with a multislice simulation of the O K-edge elemental map of the structure shown in (b), viewed in the same orientation. The integrated intensity of each column of pixels in the simulated elemental map is shown in (d). The intensity is shown in arbitrary units.

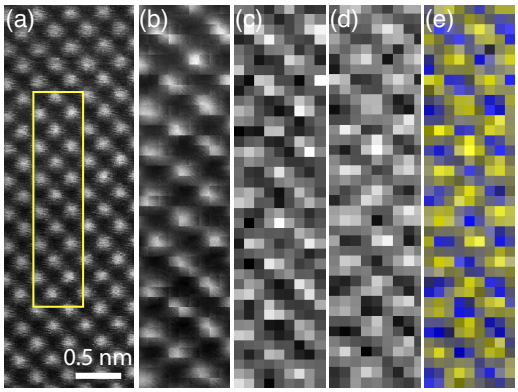

Figure 3.11: (a) High resolution ADF image of bulk YSZ viewed down the ⟨100⟩ axis. A SI was acquired from the area indicated with the yellow box simultaneously with the ADF image shown in (b). The Zr $M_{4,5}$ and O K edge integrated intensities of the PCA processed SI are shown as a function of position in (c) and (d) respectively. A composite of the two in which the red and green channels are composed of the O map (making O intensity appear yellow) and the blue channel of the Zr map is shown in (e).

of spectrum images are capable of independently resolving the structure of each element's sublattice, provided they all have well defined edges which do not overlap. In order to reduce the effects of sample drift and achieve the highest spatial resolution, spectrum images used for atomic-resolution elemental mapping tend to have larger numbers of pixels and shorter per pixel exposure times than spectrum images used to study fine structure.

Maximizing sample stability is vital to successful high spatial resolution elemental mapping. Modern instruments such as the UltraSTEM take stability to a new level, and elemental maps taken on it achieve resolutions sufficient to resolve even fine features such as Jahn-Teller distortions. When viewed down the ⟨110⟩ direction, the pure O columns of STO are separated by 2.76 Å in plane and are routinely resolved using elemental mapping. If YSZ is coherently strained to match the STO and the O atoms were ordered as in bulk YSZ, they would also have a separation of 2.76 Å as illustrated in Figure 3.10(a). As viewed in the model, the material is oriented such that the STO is viewed down the ⟨110⟩ and the YSZ down the ⟨100⟩ axis. The structure is the result of DFT calculations which optimized the size of the supercell

in the direction perpendicular to the interface. The O spacing in this direction is a slightly shorter 2.39 Å. Both of these lengths are greater than the resolution typically achieved in EELS maps acquired on the UltraSTEM. Therefore, if the O lattice is ordered it should be resolved.

Figure 3.10(b) is the result of performing simulated annealing with DFT on the structure shown in (a). The O sublattice disorders to the point of randomness, as in the high temperature MD of bulk strained YSZ. A multislice simulation of the O K-edge elemental map that would result from viewing a sample consisting of the 11 Å thick structure shown in Figure 3.10(b) repeated to a thickness of approximately 110 Å is shown in Figure 3.10(c). The O columns are clearly resolved in the STO but appear quite blurred out in the interfacial planes of TiO_2 and in the YSZ. The repetition of the relatively thin supercell used in the DFT calculation to make a thicker sample imposes order that is not likely to exist in a real sample. In a real sample, O atoms will be distributed over far more probe positions, causing even greater spatial blurring than in the simulation. If the YSZ O sublattice is disordered, an O elemental map should resolve columns in the STO but be only a blur in the YSZ.

To demonstrate that ordered O atoms in YSZ are resolved when viewed down the $\langle 100 \rangle$ axis, I performed atomic-resolution elemental mapping in bulk YSZ. A high resolution ADF image of bulk YSZ is shown in Figure 3.11(a). A yellow box delineates the region nominally used for the spectrum image. An ADF image recorded simultaneously with the spectrum image is shown in Figure 3.11(b), from which it is clear what the true positions of the heavy columns were during EELS acquisition. The SI data were denoised using PCA, and the integrated intensities of the Zr M and O K edges shown in Figures 3.11(c) and (d) respectively. A composite of the two maps is shown in Figure 3.11(e) in which the blue channel is composed of the Zr map and the red and green channels composed of the O map. As such, Zr columns appear blue and O columns appear yellow. Areas with high intensity in the simultaneous ADF image correspond to Zr sites, and also appear bright in the Zr elemental map. The O map also shows a lattice of bright spots. They are between the Zr columns seen in the ADF as is the correct position of the O atoms in the ordered material.

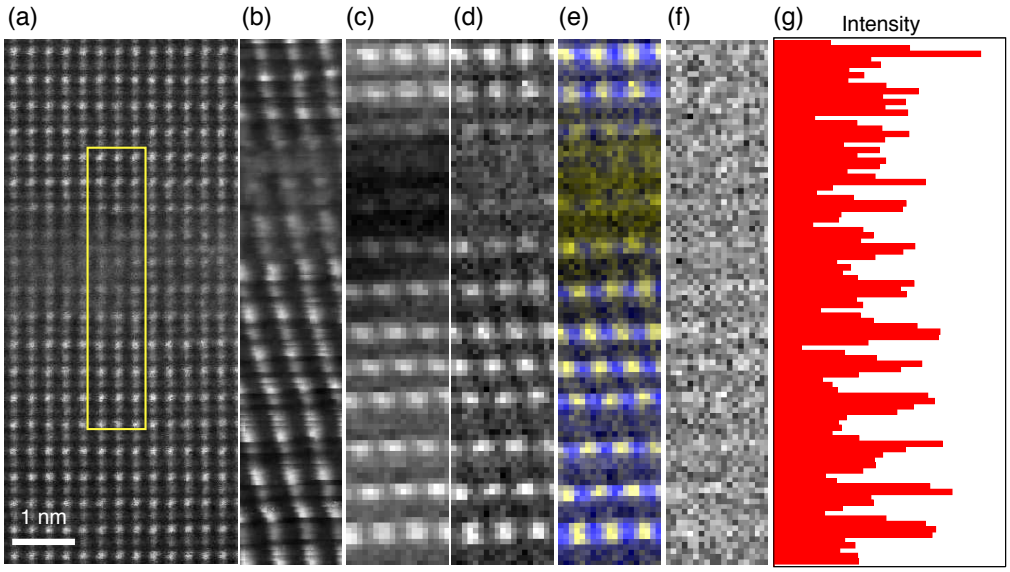

Figure 3.12: (a) High resolution ADF image of a section of coherent YSZ/STO multilayers viewed down the ⟨110⟩ STO axis. An ADF image recorded simultaneously with a SI taken in the area indicated by the yellow box is shown in (b). Integrated Ti L and O K edge intensity elemental maps extracted from the PCA processed SI are shown in (c) and (d) and as a composite map in (e) in which O intensity is shown in yellow and Ti intensity is shown in blue. An O elemental map extracted from the SI without PCA processing is shown in (f), and the integrated intensity of each row of pixels in the raw O map is shown in (g). The intensity is given in arbitrary units, with the background subtracted to improve the contrast.

Having established that an ordered YSZ O sublattice should be resolved, let us now turn to elemental maps of the YSZ/STO multilayers. PCA processed Ti and O elemental maps taken from the boxed area in Figure 3.12(a) are shown in Figures 3.12 (c) and (d) and as a composite in which O is shown in yellow and Ti in blue in (e). In addition an O map produced from the SI without PCA processing is shown in (f) and the integrated intensity of each row of pixels in the raw O map is plotted at the same scale beside it in part (g) of the figure. From the simultaneous ADF image, (b), it is clear that there was some sample drift over the course of the 6 minutes and 27 seconds it took to acquire the 19×98 pixel SI. The drift is seen to be relatively uniform and without any large jumps. More importantly the Ti and pure O columns are clearly resolved in the STO in the elemental maps and in the correct positions based on the positions of the Sr and Ti columns in the simultaneous ADF image. In the YSZ region of the O maps, the O lattice blurs out and all but disappears, consistent with the presence of a disordered YSZ O sublattice.

The ADF images show small variations of intensity between the rows of atoms inside the YSZ region consistent with the patterning of the surrounding STO, but with much lower contrast, suggesting there is some STO above or below the YSZ. The Ti map shows only very weak intensity columns in the YSZ region. Their presence is significant, however, as the only O columns that appear in the YSZ region in the O elemental maps are similarly weak, and positioned vertically aligned and horizontally interspersed with the dim Ti columns. As can be seen from the model in Figure 3.10(a), the spacing between rows of pure O columns in STO is twice that of ordered YSZ. If the YSZ O atoms were ordered as in the model, one would therefore expect to see strong peaks at twice the frequency as in STO, not just weak spots in TiO rows against a relatively uniform background. The lack of such peaks thus strongly suggests that we are indeed seeing O disorder in the YSZ.

Further support for the presence of a disordered YSZ O sublattice is seen by comparing the linetraces of the experimental and theoretical O elemental maps. The average intensity of each row of pixels in the raw O map (Figure 3.12(g)) shows clear contrast in the STO with peaks corresponding to the TiO_2 planes, but very little

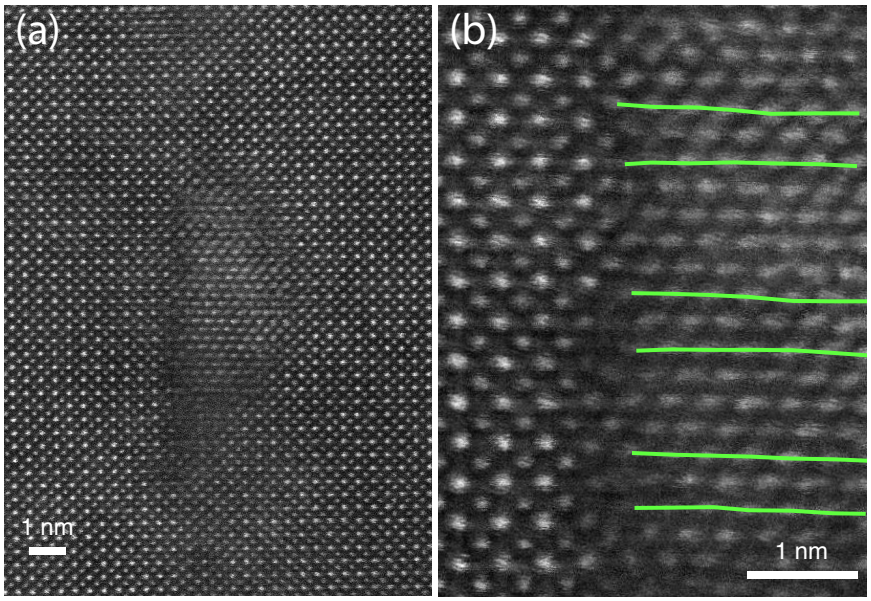

Figure 3.13: (a) High resolution ADF image of an incoherent YSZ island surrounded by STO. (b) A magnified view of the interface on the left side of the island shown in (a). The green lines are drawn through the centers of the Zr columns, illustrating the expansive strain that occurs in these regions near the interface.

contrast in the YSZ region. This lack of contrast is similar to that seen in Figure 3.10(d) for the O elemental map simulated for the multilayer structure with extreme O disorder produced by DFT calculations. I note that the blurring out of the heavy ions in the YSZ region seen in the ADF images is consistent with the deviations seen in the Zr positions seen in the simulated multilayer shown in Figure 3.10(b). Although the Zr atoms are not disordered to the extreme degree of the O atoms, they do not form perfect columns, which would cause some blurring out of the Zr columns in the ADF images.

In addition to the coherent STO/YSZ interfaces I also saw evidence for a combination of strain and O disorder at the interfaces of incoherent YSZ islands and the surrounding STO. Figure 3.13 shows a high resolution ADF image of a YSZ island. Strain and disorder are associated with dislocation cores such as those seen in the magnified view of Figure 3.13. Areas of YSZ expansion and contraction appear along the interface. The green lines follow the YSZ unit cells from the middle of the island to the interface where the unit cells are expanded. The lattice spacing around the

dislocation cores is up to 10±2 % larger than in the center of the island. This strain is even greater than the 7% of YSZ coherently layered with STO, suggesting the region may also support a high O conductivity.

A similar island is shown in the ADF image in Figure 3.14(a) for which a 9×55 pixel spectrum image was recorded in the area indicated by the yellow rectangle with a 0.3 second per pixel exposure time. The O K-edge extracted from spectra integrated over equal numbers of pixels in the STO, the middle of the YSZ island and from the interface region are shown background subtracted in part (e) of Figure 3.14. The regions used for the integration are indicated by boxes superimposed on the simultaneous ADF image. The O edge from the center of the YSZ island, which is not strained, looks very much like that of normal bulk YSZ. The fine structure of the edge from the interface regions shows only broad features, however, other than features on the scale of noise. Integrating over the interfacial region, one would expect to see a combination of STO and YSZ fine structure features, yet in these interfacial regions the fine structure does not appear to be a simple linear combination of the two. The blurred out appearance of the fine structure at the interface is again suggestive of O disorder. As the combination of expansive strain and O sublattice disorder enhances the O ionic conductivity, it is likely that these strained interfacial regions can also support enhanced ionic conductivities. Blocking effects may prevent them from achieving such high ionic conductivities as reported for the coherent YSZ/STO multilayers. In addition, incoherent islands of YSZ in STO are unlikely to be well connected, meaning that although AC conductivity measurements could show high conductivities due to ionic conductivity in isolated expansively strained regions, O transport over long distances may not be possible.

The integrated Ti and O edge intensities are shown in parts (c) and (d) of the Figure 3.14 alongside the simultaneously acquired ADF image shown at the same scale. The Ti signal intensity drops off quickly at the interface with the YSZ island where it is dark. The O signal is bright in both the STO and the YSZ but is significantly reduced around the interface region. The reduced O signal suggests the presence of an enhanced vacancy concentration at the interface. The O deficient region extends

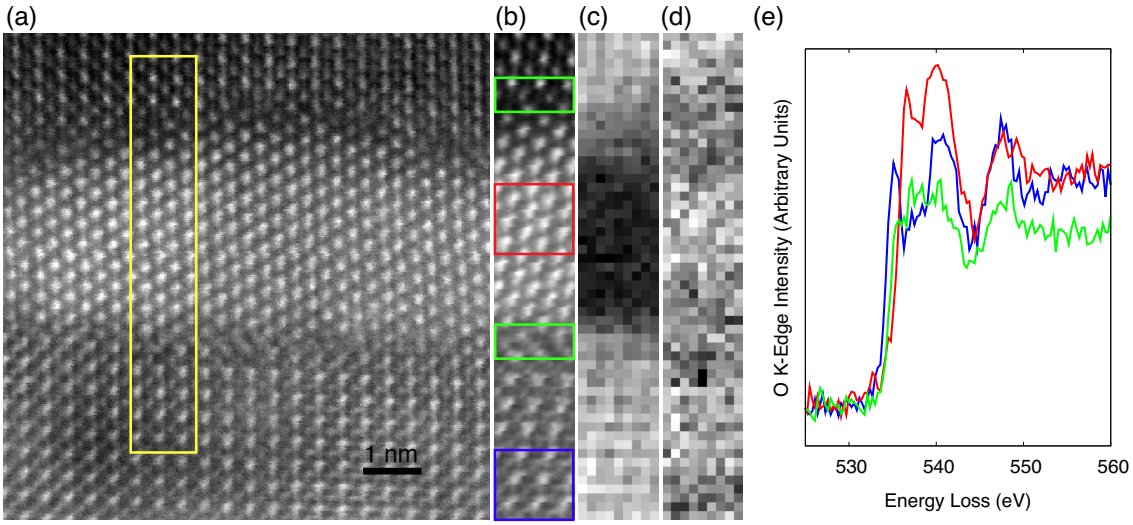

Figure 3.14: (a) High resolution ADF image of an incoherent island of YSZ surrounded by STO. (b) ADF image recorded simultaneously with a SI recorded in the area indicated by the yellow box in (a). Ti and O elemental maps extracted from the SI are shown in (c) and (d) at the same scale as (b). The O K-edge extracted from the regions indicated by the corresponding colors in (b) are shown in (e). The green spectrum shows a significant reduction in the continuum region of the spectrum, indicating the presence of O vacancies.

into the STO. O deficiency at dislocation cores in STO and related structures and its effect on current transport has been reported previously [74, 75]. Vacancies cause STO to become metallic.

Experiments on samples of STO containing YSZ islands have been reported by Cavallaro et al. [76], which they believe show the majority of the conduction occurring in samples they have grown by pulsed laser deposition to be electronic in nature. They report a one order of magnitude decrease in the conductance of their material as they decrease the O partial pressure from 1 bar pure oxygen to 3×10^{-4} bar. The decrease in partial pressure should increase the number of O vacancies in the material. The decrease in conductance with partial O pressure they measure could therefore be explained, as they suggest, by the n-type doping of vacancies compensating an intrinsic p-type doping of the material. P-type doping could, for instance, be caused by diffusion of Y into the STO.

Clearly the nature of the conductivity of STO/YSZ nanocomposites depends on the balance of doping by interdiffusion of ions and the concentration of vacancies in the STO. Note that DFT calculations suggest that it is energetically unfavorable for O vacancies to leak out of YSZ into the STO when they are grown in coherent multilayers [66]. Additionally, the conductivity of the coherent STO/YSZ multilayers grown by Garcia-Barriocanal et al. showed negligible dependence on the partial oxygen pressure [58]. These facts support ionic conductivity as the dominant form of the conductivity observed in the coherent YSZ/STO produced by Garcia-Barriocanal et al. If electronic conduction was dominant, the change in the STO vacancy concentration introduced by changing the O partial pressure should have significantly altered the conductivity.

CHAPTER IV

ATOM-BY-ATOM IDENTIFICATION OF ATOMS IN SINGLE LAYER BORON NITRIDE WITH ANNULAR DARK-FIELD STEM AND DFT

Light single layer materials such as graphene and boron nitride have low knock-on damage thresholds. Even at 100 kV holes are drilled in the sample too quickly for microscopy to be practical. At 60 kV however, these materials are far more stable, and it is possible to observe them for many minutes without causing damage. The development of aberration correction has coincided with the recent explosion of interest in such light atomically thin materials. This is fortunate as prior to aberration correction the resolution at low-kV was too poor to observe the atomic structures of graphene and BN. With aberration correction it is now possible to achieve probe sizes close to 1 Å at 60 kV [20]. As there are no interatomic distances not involving hydrogen less than 1.2 Å, a probe close to 1 Å should be sufficient for atomic resolution imaging of single layer materials.

In order to identify which atom is which in monolayer boron nitride (BN), bright-field phase-contrast imaging has recently been used [77, 78, 79]. However, because the bright-field signal is very similar for boron and nitrogen, the two types of atoms are difficult to distinguish. The only study to distinguish B and N sites in a TEM had to resort to averaging over 20 different B-N pair locations in order to obtain a sufficient signal-to-noise ratio. The identification of individual atoms was therefore not direct, and the technique is not able to image a particular configuration in a changing sample. EELS, also suffers from a need for long acquisition times, and a lack of spectral features suitable for an identification at high spatial resolution for about 50% of elements. The ADF STEM image intensity increases with the atomic number (Z) of the atom as about $Z^{1.7}$. This dependence makes the ADF signal from light atoms much weaker than from heavy ones, and the technique has therefore not been used much in the past for imaging light atoms. My collaborators and I

have now shown that aberration correction allows a STEM to be optimized for low-voltage operation such that the ADF signal is strong enough to image and identify the chemical type of light atoms neighboring each other on the periodic table [19].

Figure 4.1(a) shows a high-magnification ADF STEM image of monolayer BN grown by Valeria Nicolosi, recorded at 60 kV on a Nion UltraSTEM by Matthew F. Chisholm. The probe size was about 1.2 Å. The BN monolayer region was surrounded by thicker regions, one of which is seen on the left side of the image, and vacuum. Individual boron and nitrogen atoms are clearly distinguished by their intensity. Each single hexagonal ring of the BN structure, for instance the one marked by the green circle in the figure, consists of three brighter nitrogen atoms and three darker boron atoms. The pattern is repeated throughout the image of the monolayer BN. However, there are several deviations from this pattern, such as the hexagonal ring marked by the yellow circle, which shows six atoms with intensities intermediate to those of B and N.

In order to interpret the irregular features correctly, it was necessary to remove the contribution from the tail of the electron probe to the nearest-neighbour sites. If this contribution is present, the tails from the heavier N atoms contribute more strongly to the B sites than the tails from the lighter B atoms contribute to the N sites, and the intensities at the two sites cannot be compared quantitatively. Ondrej L. Krivanek and Niklas Dellby deconvolved the image using a procedure that removed the tail contribution from the nearest-neighbour sites, and also removed (smoothed) the pixel-to-pixel statistical noise caused by the spreading of the available signal among the many pixels in a massively oversampled image. The deconvolved version of Figure 4.1(a) is shown in Figure 4.1(b).

Figure 4.1(c) shows line profiles through the two locations marked in Figure 4.1(b). Profile X-X' starts with two atoms of the hexagonal ring marked by the yellow circle in Figure 4.1(a). The rings atoms are clearly different from the alternating boron and nitrogen atoms shown in the rest of the profile. Carbon (Z = 6) substituting for the B (Z = 5) and N (Z = 7) is the likely explanation. Profile Y-Y' goes through the regular B-N pairs, with one exception: the first atom in the profile is significantly

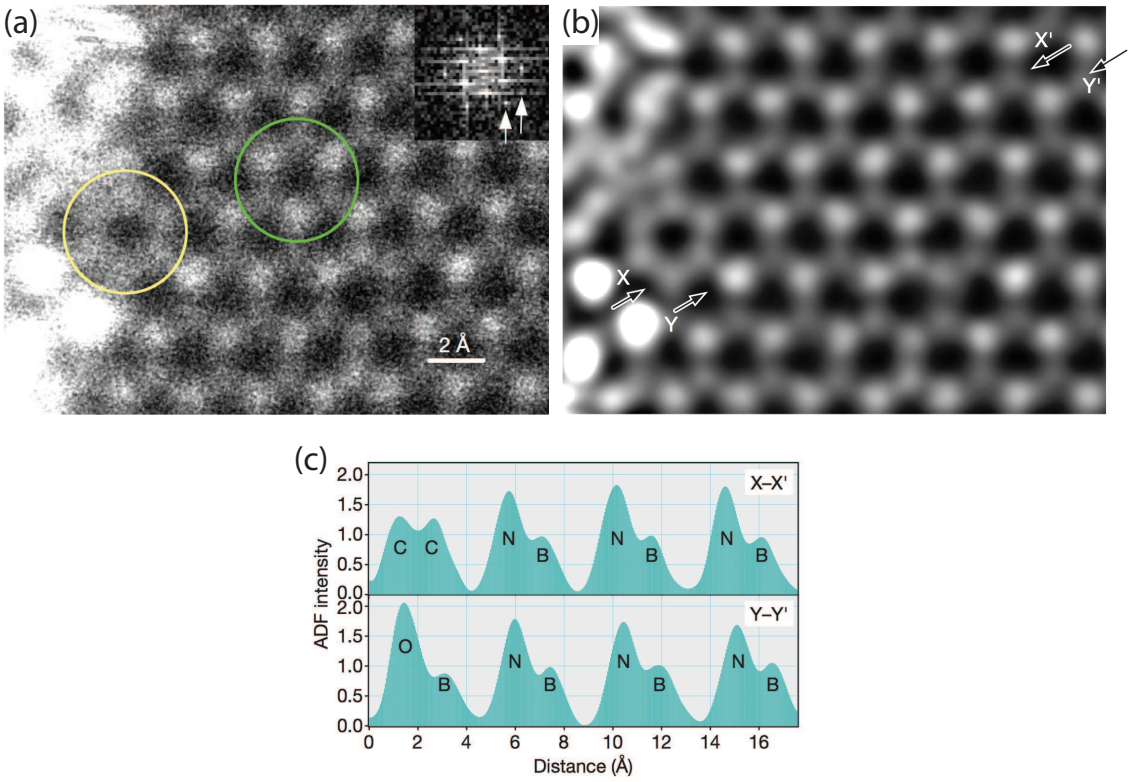

Figure 4.1: ADF STEM image of monolayer BN. (a), As recorded. (b), Corrected for distortion, smoothed, and deconvolved to remove probe tail contributions to nearest neighbours. (c), Line profiles showing the image intensity (normalized to equal one for a single boron atom) as a function of position in image b along X-X' and Y-Y'. The elements giving rise to the peaks seen in the profiles are identified by their chemical symbols. Inset at top right in a shows the Fourier transform of an image area away from the thicker regions. Its two arrows point to $(11\bar{2}0)$ and $(20\bar{2}0)$ reflections of the hexagonal BN that correspond to recorded spacings of 1.26 and 1.09 Å. Image recorded by M. F. Chisholm, deconvolution performed by O. L. Krivanek and N. Dellby.

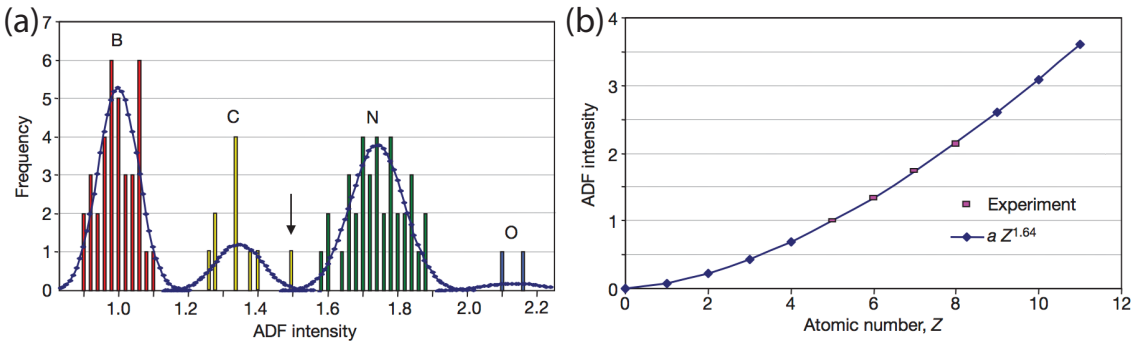

Figure 4.2: Analysis of image intensities. (a), Histogram of the intensities of atomic image maxima in the monolayer area of Figure 4.1(b). (b), Plot of the average intensities of the different types of atoms versus their atomic number, Z. The heights of the rectangles shown for B, C, N and O correspond to the experimental error in determining the mean of each atomic types intensity distribution.

brighter, and is probably oxygen (Z = 8). Without a quantitative statistical analysis, however, atomic identifications such as these are rather tentative. The appropriate way to quantify the image is to compute a histogram showing the distribution of the atom intensities [80, 81] for all the atoms in a given area, and to use the histogram to determine the probability that the atomic assignments were made correctly. Such an analysis seems not to have been done before on images of atoms of similar Z.

Figure 4.2(a) shows a histogram of the peak intensities for all the atoms in the monolayer sample area shown iny Figure 4.1(b) (that is, excluding atoms in the thicker region on the left side of the figure) created by Ondrej L. Krivanek and Niklas Dellby. The intensities were normalized such that the center of the B peak is 1. A theoretical fit for the distributions of the different species of the atoms, based on the standard deviations determined experimentally for the B and N atoms, and extrapolated to the C and O distributions, is overlaid on the figure. The separation of the histogram peaks is such that every atom in the analyzed area could be assigned to a particular species with >99% confidence, with one exception: the atom marked by the arrow in the histogram. This atoms intensity was $3\sigma_C$ from the mean C value and $5.6\sigma_N$ from the mean N value, and it was therefore likely to be carbon at 94% confidence level. In the examined part of the image, no N atoms were assigned to B sites or vice versa.

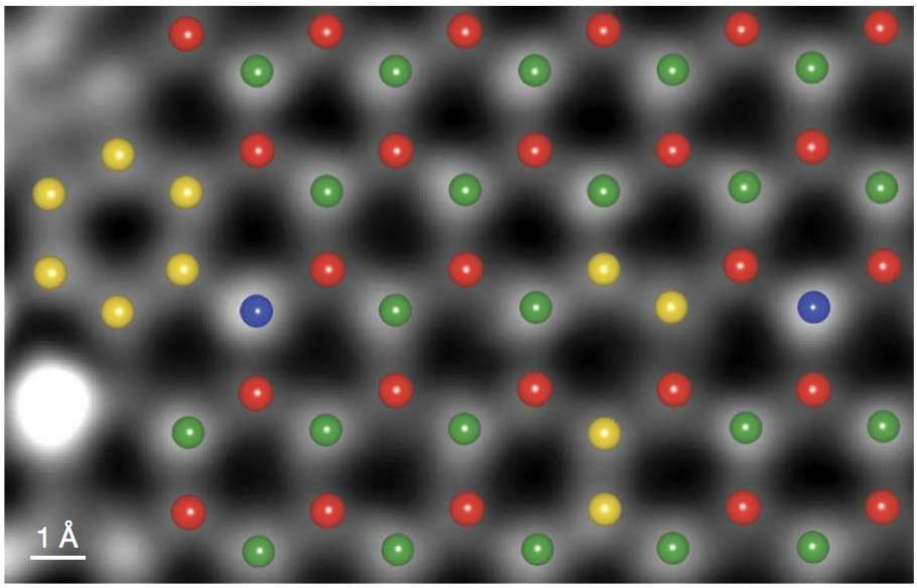

Figure 4.3: Part of a DFT simulation of a single BN layer containing the experimentally observed substitutional impurities overlaid on the corresponding part of the experimental image. Red, B; yellow, C; green, N; blue, O.

This was expected at the >99.99% confidence level that applied to not assigning an atomic species differing by $\Delta Z = 2$ from the correct one.

Figure 4.2(b) shows the dependence of the average intensity of the four types of atoms identified in the sample on their atomic number Z, and compares it to a $Z^{1.64}$ model spanning from Z = 1 to 11 (H to Na). The match for the observed elements shows no deviation exceeding the statistical noise present in the image. It demonstrates the simple nature of ADF image contrast, which is able to reveal the chemical identity of non-overlapping atoms very directly. The power of the derived Z dependence is influenced by the deconvolution procedure, and it will also vary slightly depending on the signal collection geometry used and the Z of the studied elements. However, it is expected to remain in the range 1.5 to 1.8.

Figure 4.3 shows a diagram I created of the atomic structure that corresponds to the impurity atoms identified in the monolayer, superimposed on the deconvolved experimental image. Carbon atoms are only seen to substitute for B-N pairs, not for individual boron or nitrogen atoms. Oxygen, on the other hand, substitutes for

single N atoms. I determined the atomic positions in the diagram by relation with DFT. The input was a single BN layer containing the substitutional defects identified by the histogram analysis. The DFT calculations were performed using a plane-wave basis within the projector-augmented-wave method and generalized-gradient approximation as implemented in the VASP code. A periodic supercell containing a single layer of boron nitride consisting of 60 atoms was constructed using the B-N nearest neighbor separation of 1.45 Å. The out of plane dimension of the supercell was set to 12 Å. Carbon atoms were substituted for the B and N atoms of one of the boron nitride rings, and an O atom substituted for a N atom neighboring the carbon ring. The structure was then relaxed using an energy cutoff of 400 eV and up to a 3x3x3 Monkhorst-Pack k-point mesh centered at the Γ-point. The resulting supercell was then doubled in each of the inplane directions and filled with additional single layer BN and the extra C and O substitutional impurities identified by the histogram analysis. The resultant 240 atom supercell was relaxed using only the Γ-point in k-space and an energy cutoff of 400 eV.

Close inspection of Figures 4.1(b) and 4.3 shows that there were significant distortions in the lattice next to the two oxygen atoms, whose nearest neighbors were significantly further away than the B-N distance of 1.45 Å. One very visible result of these distortions was that in the hexagonal ring of C atoms, the C nearest neighbor of the adjacent O atom appears pushed into the carbon ring. This is seen both in the experimental image, which shows the average distance between the two oxygen atoms and their nearest neighbors (averaged over the six nearest neighbors of the two atoms) to be stretched by 0.14 ± 0.08 Å relative to the B-N distance of 1.45 Å, and in the DFT-relaxed model, which shows an O-C stretch of 0.09 Å. This demonstrates that even in the presence of statistical noise that shifts the individual atomic images by small random amounts, ADF imaging is at present able to track atomic displacements with a precision of about 0.1 Å.

In summary, ADF imaging in an aberration-corrected STEM operated at 60 kV primary voltage has allowed us to determine the positions and the chemical types of all the atoms in a significant part of an unknown, non-periodic material. Looking

towards the future, note that the ADF signal originates from electron scattering by the atomic nucleus, and that the potentially attainable ADF resolution is therefore much sharper than the conventional atomic size that is determined by the diameter of the outermost electron orbitals. As instrumentation advances improve the resolution of electron microscopes even further in the future, the ADF signal from individual atoms will be focused into smaller and smaller image areas. This will improve the signal-to-noise ratios of individual atomic images recorded at a given electron dose, and the atoms will become easier to identify unambiguously even in complicated projections.

CHAPTER V

HYBRID DENSITY FUNCTIONAL THEORY APPLIED TO LCMO

Transition metal oxides are often considered too complex for DFT in the LDA or GGA approximations because of the 3d electrons. It is widely believed that a Hubbard U is needed to account for strong correlations. A phase diagram of $La_xCa_{1-x}MnO_3$ adapted from data reported in [82, 83] is shown in Figure 5.1. It begins with LMO on the left, which is an anti-ferromagnet (AFM) at low temperatures. Doping LMO with Ca causes the material to turn into a ferromagnet (FM) for $x < 0.5$. The doped LMO remains an insulator until between $x = 0.1$ to 0.2, after which it becomes a metal until around $x = 0.5$, after which LCMO becomes an AFM insulator.

The results of Luo et al. comparing the predictions of GGA and GGA+U at three values of x are shown in Figure 5.2. The vertical axis displays the difference in total energy predicted for the AFM and FM magnetic orders in meV. Negative values indicate the AFM order is more energetically favored whereas positive values indicate that the FM order is favored. Using both the experimental volumes and the theoretically predicted volumes for CMO and $La_{0.5}Ca_{0.5}MnO_3$ with ordered dopants produced superior results to GGA+U. In principle, calculations with dopants should be performed using large supercells with different dopant arrangements followed by averaging over such arrangements. Such a series of calculations is not practical. A method to circumvent the need for such an arduous series of calculations is "generic doping" in which extra electrons are introduced or removed and compensated for with a uniform background charge. The validity of generic doping is supported by the fact that the total energies produced for $La_{0.5}Ca_{0.5}MnO_3$ using it and ordered doping were very similar. Using ordered doping for $x = 0.33$ was not possible, and the generic doping method allowed the GGA to be compared to GGA+U for $La_{0.33}Ca_{0.67}MnO_3$. Again, GGA outperformed GGA+U. In every case GGA+U decreased the energy advantage of the experimentally observed AFM phase, and with $U = 8$ eV for all points with $x \leq 0.5$ the FM structure was considerably more energetically favorable.

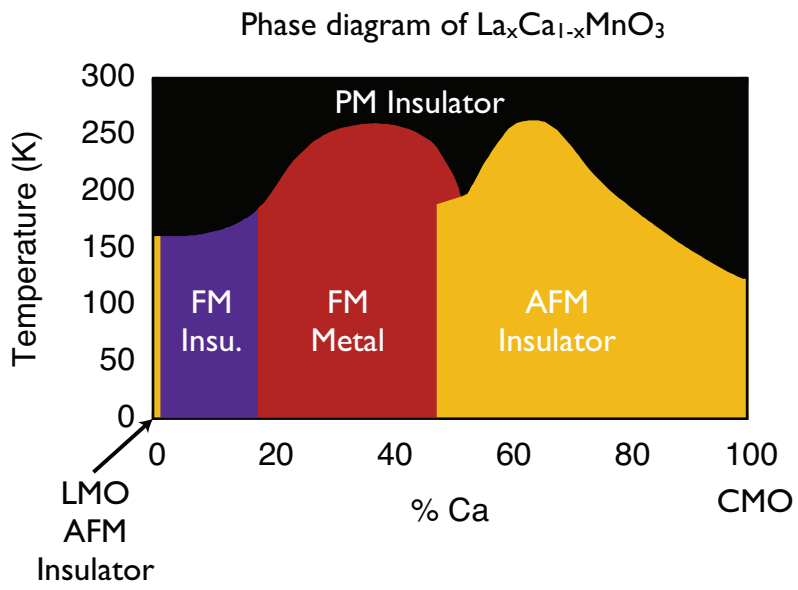

Figure 5.1: The phase diagram of $La_xCa_{1-x}MnO_3$.

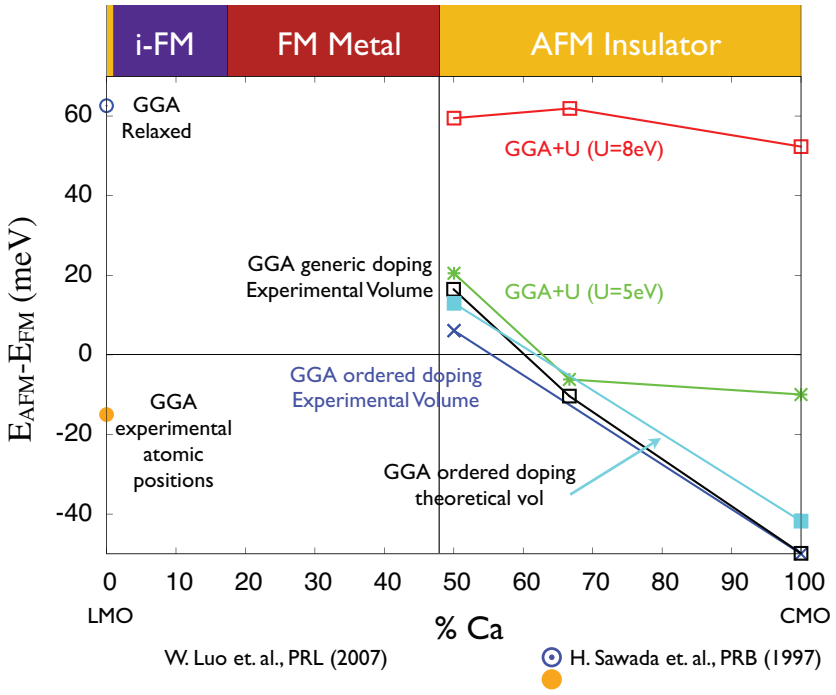

Figure 5.2: The energy difference of the AFM and FM phases as a function of x in $La_xCa_{1-x}MnO_3$. The experimentally observed phase is indicated in the colored bar at the top.

With $U = 5$ eV, the GGA+U results were better, predicting AFM for CMO and $x = 0.33$, but FM for $x = 0.5$. GGA also produced a FM phase lower in energy than the AFM phase for $x = 0.5$, but the difference in energy was smaller.

These results suggest that the U is not helping, but hindering the calculations of the magnetic ordering for LCMO. On the other hand, GGA+U calculations predict the correct structure and AFM magnetic ordering for LMO, whereas GGA slightly underestimates the Jahn-Teller distortions causing it to predict a FM magnetic ordering. If however the experimental structure is enforced, GGA does predict the correct AFM magnetic ordering. The two methods, GGA and GGA+U, also produce inconsistent band structure. New exchange-correlation functionals have recently become available that do very well in correcting the well-known band gap problem of semiconductors and insulators. To test if such a hybrid functional might provide more accurate and consistent results I performed calculations with the HSE06 hybrid density functional [84] to predict the structure and magnetic order for several members of the $La_xCa_{1-x}MnO_3$ series.

Hybrid functionals use an admixture of the DFT and Hartree-Fock exchange functionals. The PBE0 hybrid functional [85, 86, 87, 88] is based on the PBE DFT exchange correlation functional of Perdue et al. [89], and uses the exchange-correlation energy

$$E_{xc}^{PBE0} = aE_x^{HF} + (1-a)E_x^{PBE} + E_c^{PBE},$$

where E_x^{HF} is Hartree-Fock exchange, E_x^{PBE} is the PBE exchange functional and E_c^{PBE} is the PBE correlation functional. The HSE06 hybrid functional [84] reduces the computational complexity by using a screened Coulomb potential for the Hartree-Fock exchange E_x^{HF}. The PBE0 functional is used for interactions inside a given radius, and the PBE GGA functional is used for interactions outside that radius. I used this functional as implemented in the VASP code. Strict HSE06 uses a value of 1/4 for a [90], and although other values can be used, I used this value in the calculations.

In LMO, the hybrid functional slightly overestimates the Jahn-Teller distortions by a similar amount as GGA underestimates them. HSE06 gives a C/A ratio of 1.14,

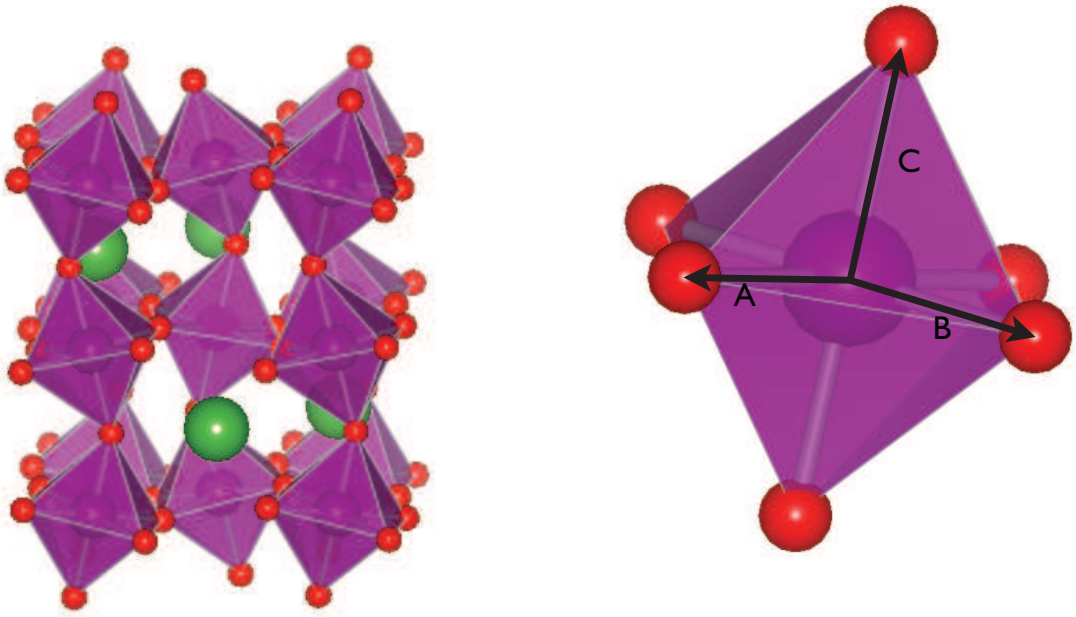

Figure 5.3: The LMO supercell after relaxation with HSE06 (left) with an isolated oxygen octahedron with bond lengths labeled as used to describe the Jahn-Teller distortions (right).

GGA a ratio of 1.07, and the experimentally determined ratio is 1.11. For the C/B ratio HSE06 gives a value of 1.16, GGA a value of 1.08, and the experimentally determined value is 1.15. So HSE06 does a slightly better job of predicting the Jahn-Teller distortions than GGA. Probably because it slightly overestimates the distortions, HSE06 also predicts the correct magnetic ordering after relaxing the structure, unlike GGA.

Unlike GGA+U, the hybrid functional also predicts the correct magnetic ordering for $La_xCa_{1-x}MnO_3$ at $x = 0$ (CMO), $x = 0.33$, and $x = 0.50$ as well. Table 5.1 gives a comparison of the energy differences $E_{AFM} - E_{FM}$. These points however are all AFM insulating phases. Due to the large number of kpoints needed to accurately simulate metals, it was not possible to test the functional for the metallic points on the phase diagram. So it is possible that the functional might introduce a systematic bias in favor of AFM. The computational expense of using the hybrid functional was also a severe limitation. The calculations of the two end materials, CMO and LMO,

were very computationally demanding. I was only able to converge the relaxation with up to a $4 \times 4 \times 4$ Monkhorst-Pack grid for CMO and only a $2 \times 2 \times 2$ grid for LMO. The intermediate phases have considerably larger supercells, and I was only able to converge the relaxation with up to 2 kpoints for these structures. The inability to use higher kpoint samplings for these intermediate phases makes it hard to draw any useful conclusions for these phases. With a higher kpoint density, the FM phase might become the preferred order. The computational cost of such hybrid functionals would therefore seem to make them at present impractical for many of the systems of interest today, which tend to require larger supercells.

Table 5.1: Energy difference between the AFM and FM magnetic orders as calculated by HSE06.

	LMO	$La_{0.5}Ca_{0.5}MnO_3$	$La_{0.33}Ca_{0.67}MnO_3$	CMO
$E_{AFM} - E_{FM}$ (eV)	-0.015	-0.18	-0.31	-0.106

CHAPTER VI

OPTICAL GAPS OF FREE AND EMBEDDED SI NANOCLUSTERS: DENSITY FUNCTIONAL THEORY CALCULATIONS

The tunable optical properties of nanoclusters make them attractive candidates for a diverse variety of applications. Among these are lasers, biomarkers, solar cells, displays and optoelectronics, for which Si nanoclusters (Si-NCs) are of particular interest [91, 92, 93, 94, 95, 96]. Simulations show that the optical band gap of perfect isolated Si-NCs increases roughly as the inverse of their diameter from the bulk Si gap of 1.1 eV to 5 eV or more [97, 98, 94]. Real Si-NCs are rarely isolated or perfect, however, and experimental reports of the tunable range of the gap vary significantly. For Si-NCs greater than 3 nm in diameter, the optical gaps generally increase with decreasing diameter as predicted for perfect isolated Si-NCs. Below 3 nm however, the energy gaps open up much more slowly, reaching only 2-3.5 eV [99, 100, 101, 102, 103, 104, 105]. The optical properties of Si-NCs have also been studied over a wider range of energies [106, 107, 108].

Many studies have been devoted to understanding the optical gaps of small Si-NCs. The observation that Si-NCs with photoluminescence (PL) peak energies between 2-3 eV all had PL peaks at $\sim$2 eV after exposure to oxygen [100] led many to believe that O bonds on the surface of the NCs cause the reduced optical gaps. Subsequent theoretical studies [100, 94, 109, 110, 111, 112, 113, 114, 115] showed that O atoms bonded to the surface of ideal Si-NCs indeed introduce localized defect states within the band gaps, reducing or eliminating the opening of the HOMO-LUMO gaps due to quantum confinement. Other experimental studies have reported little difference in the optical gaps with or without O, but the gaps are still considerably smaller than would be expected for a perfect isolated nanocluster [103, 116]. More recent theoretical studies have considered nanoclusters that are not isolated, but embedded in SiO_2[117, 118, 119, 120, 110, 121, 95, 122, 123, 124]. These studies revealed that the HOMO or LUMO charge densities extend into the oxide overlayer, reducing the

confinement and therefore the gaps. Additionally, an effort has recently been made to realistically simulate the deformation of NCs that can occur when they are embedded in an amorphous matrix [125]. Calculations of the densities of states (DOS) reveal that deformation alone can cause significant changes to the band gap [122].

In this chapter I compare the effects of deformation, O impurities, and oxide coverage on the optical gaps of small Si-NCs using real-space linear response calculations within the time-dependent local-density approximation (TDLDA) [126]. The TDLDA approach extends ground state density-functional theory to better describe excited states and optical transition probabilities. TDLDA significantly increases the optical gaps of semiconductor and s- and d-electron metal nanoclusters, bringing them into much better alignment with experimental values than LDA [109, 127]. So far TDLDA has been used to study free Si nanoclusters [109, 128]. By systematically comparing the photoabsorption for undeformed and deformed 0.75 nm clusters as they are increasingly oxidized I demonstrate that deformation, O impurities and oxide coverage all decrease the size of the optical gaps. Furthermore, by examining the charge densities of the states that are actually involved in the lowest energy optical transitions I show that both localized defect states and reduced quantum confinement due to wavefunction spillage cause reduction of the optical gap. These observations explain the wide variety of experimental results seen for Si-NCs both in porous Si and embedded in SiO_2.

The deformed Si-NCs embedded in amorphous SiO_2 were generated as in [125, 122], starting with a supercell of SiO_2 containing 192 atoms in the cubic β-crystobalite structure, which is the closest to the diamond structure among the SiO_2 polymorphs. The supercell is 14.32 Å on each side. The O atoms within a 0.75 nm sphere are removed, leaving behind an embedded 13 atom Si-NC. The structure is then relaxed using DFT before the SiO_2 is amorphized and the Si-NC deformed. The DFT relaxations were performed in the generalized-gradient approximation with a plane-wave basis and projected-augmented wave potentials as implemented in the VASP code. The calculations were performed using only the Γ point in k-space with an energy

cutoff of 400 eV. The residual forces on the atoms in the relaxed structure were less than 1 meV/Å.

To amorphize SiO_2 and deform the embedded Si-NCs my collaborator, George Hadjisavvas, used the Monte Carlo (MC) algorithm of Wooten et al. [129]. This method is a well established means of generating continuous random networks from perfect crystals using bond breaking and switching moves. A Keating-like valence force model [130, 131] was used to approximate the energy of the system. After each attempted move the structure around the bond was relaxed using a steepest-descent method, minimizing the forces on the atoms. The energy of the relaxed structure was then compared to the energy before the attempted move, and the move is accepted or rejected according to the Metropolis criterion. Bond switching moves were periodically followed by volume relaxation to relieve stresses in the system.

Bond switching was first performed in only the oxide at high temperature ($k_BT =$ 3eV) for 40,000 moves, allowing it to liquify. The temperature is subsequently gradually reduced to $k_BT = 0.1$ eV over more than 10^6 moves, leaving the oxide in a glassy amorphous state. Additional bond switching was then performed by Hadjisavvas allowing moves in the NC as well as the oxide for 3×10^6 moves. This last step topologically equilibrates the composite system and deforms the Si-NC.

To separate the effects of the oxide matrix and the O bonded to the surface of the NC on the photoabsorption, Hadjisavvas produced structures in which we progressively removed layers of the SiO_2, leaving behind the two O atoms bridge bonded to the NC which resulted from the deformation process. Hadjisavvas next produced structures in which we stripped off these remaining O atoms one at a time. He also placed a single double bonded O atom on the surface of the stripped cluster so I could check what effect it would have compared to the bridge bonds. All dangling bonds were passivated with H, and I relaxed the resulting structures using DFT with VASP. To determine the role of deformation, Hadjisavvas also generated a set of undeformed 13 atom Si-NCs with similar types and levels of oxygen and oxide coverage. To generate these structures Hadjisavvas started with a supercell of bulk crystalline Si and removed Si atoms such that we were left with a Si-NC of the same

size as the deformed clusters. Hadjisavvas then added the same types of O bonds as on the surfaces of the deformed NCs and relaxed the structures after passivating the dangling bonds. Undeformed Si-NCs with additional overlayers of SiO_2 were constructed similarly, with the dangling bonds being passivated with additional Si or O atoms and the dangling bonds of the overlayers passivated with H before I relaxed them with DFT.

I obtained photoabsorption spectra from each of the structures by placing them in a large spherical domain, outside of which their wavefunctions were required to vanish. I then calculated the local density approximation wavefunctions in real space within the framework of the higher-order finite-difference *ab initio* pseudopotential method [132] , utilizing a Chebyshev-Davidson eigenvalue algorithm[133]. Finally, I also calculated the optical absorption spectra from the LDA wavefunctions using a linear-response formalism within the TDLDA, as implemented in the PARSEC code [134, 135], in which both the Coulomb and exchange-correlation interactions are taken into account in the electrostatic screening produced by electrons and holes.

I performed tests to determine the real-space grid-spacing required for each of the atomic species in the calculations. For structures containing only Si and H atoms a grid-spacing of 0.8 Bohr was used. A grid-spacing of 0.5 Bohr was used for calculations containing O atoms. Up to 400 energy levels were used to compute the LDA wavefunctions, which were required to vanish at a radius of 35 Bohr. In the calculation of the TDLDA photoabsorption itself, I increased the number of bands included until the photoabsorption was converged up to 6 eV, to allow reliable comparisons of the optical gaps.

The TDLDA photoabsorption spectra are shown alongside the LDA DOS for the undeformed NCs in Figure 6.1 and for the deformed NCs in Figure 6.2. The photoabsorption spectra and DOS have been broadened by a Gausian with a 0.1 eV full-width-half-maximum, normalized by the total number of electrons and displayed on the same scale. My collaborators and I defined the optical gap as the energy at which the oscillator strength reaches 0.1% of the oscillator strength integrated from

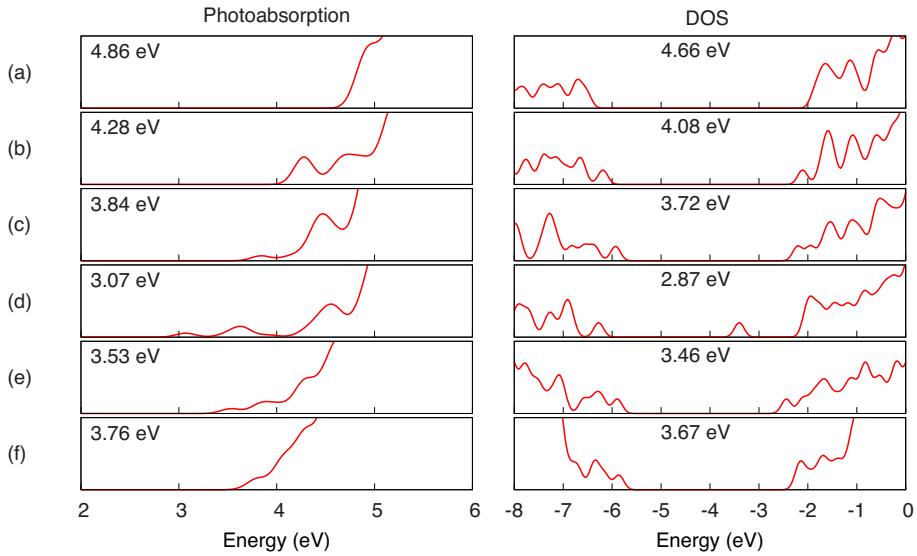

Figure 6.1: TDLDA photoabsorption and the LDA DOS for the undeformed Si-NCs at various levels of oxidation. (a) has no O, (b) has one O bridge-bond, (c) has two O bridge-bonds, (d) has one O double-bond, (e) has one layer of oxide, and (f) has two layers of oxide. The corresponding TDLDA optical and LDA HOMO-LUMO gaps are indicated.

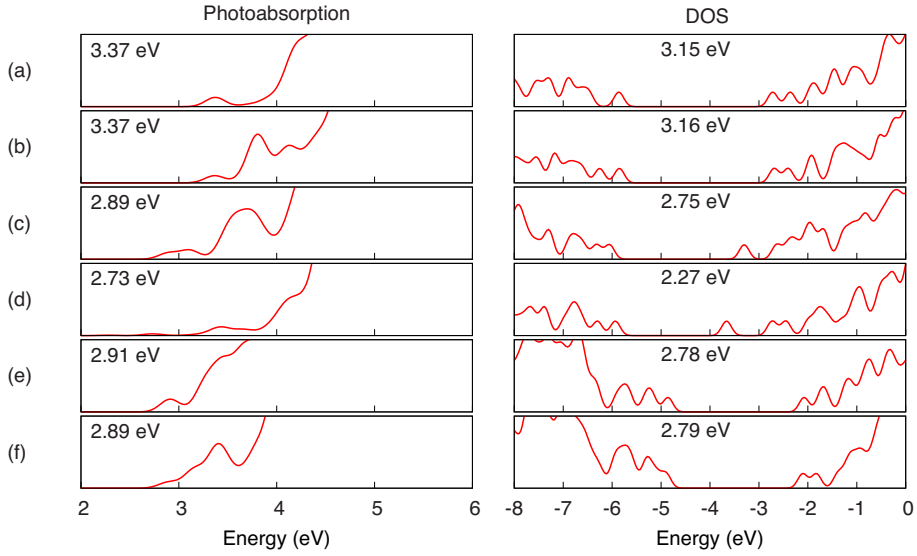

Figure 6.2: TDLDA photoabsorption and the LDA DOS for the deformed Si-NCs at various levels of oxidation. (a) has no O, (b) has one O bridge-bond, (c) has two O bridge-bonds, (d) has one O double-bond, (e) has one layer of oxide, and (f) has two layers of oxide. The corresponding TDLDA optical and LDA HOMO-LUMO gaps are indicated.

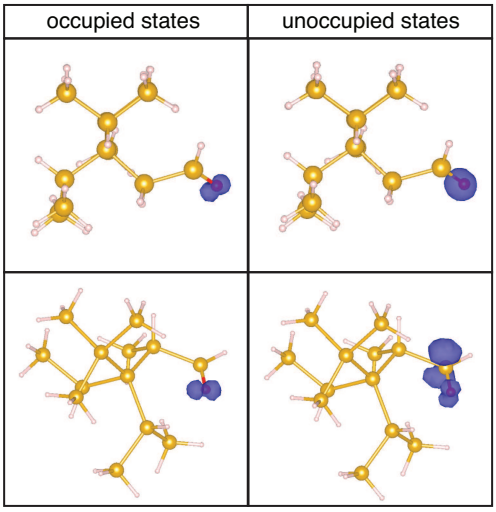

Figure 6.3: Charge density isosurfaces (dark blue) superimposed on the structures of the undeformed (top) and deformed (bottom) Si-NCs with a single O atom (dark/red) double bonded to their surfaces. Si atoms are shown as large gold balls and H as small light pink colored balls. The charge densities are weighted according to each state's contribution to the TDLDA photoabsorption strength up to 4 eV for the undeformed structure and 3 eV for the deformed structure. Isosurfaces are plotted at 10% of the maximum charge density.

0-5 eV. The optical gaps and LDA HOMO-LUMO gaps are indicated in Figures 6.1 and 6.2.

The optical gap of the bare undeformed NC is 4.86 eV, slightly larger than the 4.66 eV LDA band gap. Adding first one then two O bridge bonds to the surface of the cluster reduces the optical gap to 4.28 eV and 3.84 eV respectively. The DOS for the bridge-bonded clusters resemble that of the bare cluster, but with extra peaks just above the LUMO and below the HOMO of the bare cluster. The extra peaks reduce the size of the band gap allowing optical transitions to occur at lower energies than in the bare cluster.

Replacing the bridge bonded O atoms with a single double bonded O atom also introduces DOS peaks inside the band gap. Although the HOMO is at about the same energy as the HOMO of the cluster with a single bridge-bonded O atom, the LUMO is much deeper inside the gap. The first unfilled state appears 1.37 eV below

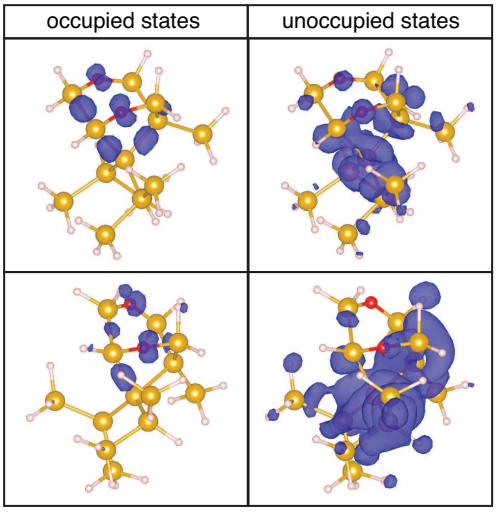

Figure 6.4: Charge density isosurfaces (dark blue) superimposed on the structures of the undeformed (top) and deformed (bottom) Si-NCs with two O (dark/red) atoms bridge bonded to their surfaces. Si atoms are shown as large gold balls and H as small light pink colored balls. The charge densities are weighted according to each state's contribution to the TDLDA photoabsorption strength up to 5 eV for the undeformed structure and 4 eV for the deformed structure. Isosurfaces are plotted at 10% of the maximum charge density.

the next lowest state in the DOS. The optical gap of the double bonded cluster is correspondingly smaller, with a size of 3.07 eV.

When a layer of O atoms was added around the cluster with two bridge bonds, the O atoms passivated the Si atoms and H atoms passivated the O atoms in the overlayer. Adding the O layer reduced the HOMO-LUMO gap by 0.26 eV. The optical gap similarly decreased by 0.21 eV. Adding a layer of Si atoms over the O layer, making a layer of SiO_2, increased the HOMO-LUMO gap to 3.67 eV, only 0.05 eV lower than the cluster with just two bridge-bonded O atoms. The optical gap increases up to 3.76 eV, also only slightly lower than for the cluster with only the two bridge-bonded O atoms.

With the realistically deformed NCs I found that deformation alone greatly reduces the optical gap. The bare deformed cluster had a HOMO-LUMO gap of 3.15 eV and an optical gap of 3.37 eV, both 1.49 eV lower than that of the bare undeformed cluster. The only undeformed cluster with smaller gaps was the one with an

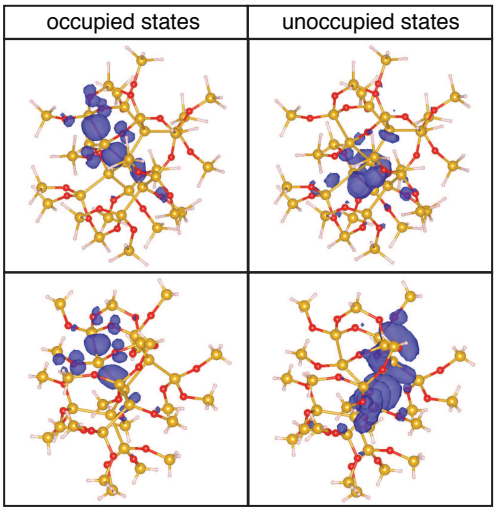

Figure 6.5: Charge density isosurfaces (dark blue) superimposed on the structures of the undeformed (top) and deformed (bottom) Si-NCs with two O atoms bridge bonded to their surfaces and covered in a full layer of SiO_2. Si atoms are shown as large gold balls, O as smaller red balls and H as small light pink colored balls. The charge densities are weighted according to each state's contribution to the TDLDA photoabsorption strength up to 4 eV for the undeformed structure and 3 eV for the deformed structure. Isosurfaces are plotted at 10% of the maximum charge density.

O double bond, the rest all had larger optical and HOMO-LUMO gaps. Adding a single O bridge-bond made no significant difference to the gaps, as might be expected from the fact that the deformation reduced the gap more than the double-bond on the undeformed cluster. The DOS of the deformed cluster with and without a single bridge-bond look fairly similar, but the bridge bond added a second peak below the energy of the HOMO. Correspondingly, a peak appears in the photoabsorption around 3.8 eV which is not there without the bridge-bond.

The addition of a second bridge-bond moved the HOMO peak slightly down in energy, but also introduced a peak in the unoccupied DOS significantly lower in energy than the LUMO of the bare cluster. The optical gap was correspondingly reduced by 0.48 eV to 2.89 eV. Replacing the bridge bonds with a single double bond produced similar HOMO and HOMO-1 peaks, but moved the LUMO DOS peak even lower in energy, resulting in a 2.73 eV optical gap. Note that the TDLDA spectrum presents an optical excitation at $\sim$2.3 eV with a nonzero oscillator strength, however

its magnitude is small compared to the other optical transitions shown in Figure 6.2(d). As its optical strength is nonzero it is not a forbidden transition. Finally, as with the undeformed cluster, covering the deformed cluster with two bridge bonds with SiO_2 matrix does not significantly alter the optical gap, suggesting that those O atoms bonded to the surface of NCs have the most influence on the size of the band gap.

In order to further investigate the nature of the states that reduce the size of the optical gaps, I plotted isosurfaces of the charge densities of the states which are actually participating in the lowest energy TDLDA photoabsorption transitions. From Figure 6.3 it can be seen that the states introduced into the HOMO-LUMO gap of the bare clusters by single O atom double-bonds are concentrated around the O atom. Reducing the isosurface level however, one can see that these states also extend to other parts of the nanocluster, which explains why the deformation of the nanocluster would affect the energies of these defect states. The bridge bonds shown in Figure 6.4 also introduce optical gap-reducing states which are concentrated around the O atoms. The charge density of these gap-reducing states is less localized than those introduced by the double bonds, and this may be the reason the optical gaps of the NCs with bridge bonds are more sensitive to deformation than those with double bonded O atoms. Finally, one can see from Figure 6.5 that adding a layer of SiO_2 over the NCs with bridge bonded O atoms makes only minor differences to the spatial localization of the states which limit the size of the optical gaps. The charge density leaks out into the oxide somewhat, explaining the slightly lower optical gaps, but is mostly concentrated in the same areas of the NCs as without the oxide.

The present results are in agreement with previous theoretical work showing that the optical gaps of small Si-NCs are reduced by the presence of O bonded to their surfaces [100, 94, 109, 110, 111, 112, 113, 114]. Previous theoretical studies of embedded Si-NCs agree that the matrix reduces the HOMO-LUMO gaps, but a number of different conclusions are reached. Some conclude that the gap shrinkage is mainly due to reduced quantum confinement due to the wavefunctions leaking out into the matrix [117, 118, 119, 121, 95]. Others show that similar gaps are produced before

and after most of the embedding SiO_2 have been removed, leaving behind only O atoms bonded to the surface of the NCs, indicating the importance of O bonds on the surface of the Si-NCs [124, 123]. Some studies also point out that the interface between Si-NC and bulk SiO_2 matrix is not likely to be abrupt, and that strain and deformation can reduce the gaps [120, 110, 124, 123, 122]. The present results, the first produced with TDLDA for embedded clusters, show that deformation and localized O impurity states have the greatest impact on the size of the optical gaps of embedded Si-NCs, with reduced confinement due to wavefunction spillage causing only relatively minor additional closing. Additionally, although deformation and O bonds on the surfaces of the NCs independently affect the optical gaps, the smallest gaps are caused by a combination of the two.

From the present calculations it is seen that O bonds and deformation can independently reduce the sizes of the optical gaps of Si-NCs. Additionally, different types of O bonds introduce defect states at different energies and result in different optical gaps. It is clear, however, that when both O and deformation are present, it is not a simple question as to which independently produces the smaller HOMO-LUMO gap. O bonded to the surface of the NCs introduces defect states at different energies depending on whether the NC is deformed or not. The optical gaps of the deformed clusters are smaller than those of the undeformed clusters by 0.34 eV with a double bonded O atom and by 0.95 eV with two bridge bonded O atoms. In general, it seems that the smallest optical gaps are produced with a combination of deformation and O atoms bonded to the surface of the NCs. In particular, the lowest energy optical gap of 2.73 eV is produced by the combination of deformation and an O double bond. Experimental samples of embedded Si-NCs generally contain NCs with a range of both deformation and O bonds. Macroscale properties such as absorption and photoluminescence depend on the average characteristics. Generally, the largest, most deformed and oxygenated clusters will limit the optical gap, with the statistical distribution of the size, deformation and oxidation determining the shape and width of the optical spectral features. An ideal sample would have a distribution of NCs with size, deformation and oxidation that was tailored to a particular application. For

instance, a narrow photoluminescence peak could be achieved at a high energy by using free ultrasmall NCs with the same size, negligible deformation, and no O bonded to their surface. A broad peak could be achieved using NCs of various sizes levels of deformation and O bonding. Achieving the former presents a difficult challenge, whereas the latter is what is generally produced.

CHAPTER VII

WHITE LIGHT EMISSION FROM ULTRASMALL CDSE NANOCRYSTALS

Nanotechnology depends on the fact that, as structures are made smaller, they acquire unique properties. For semiconductor nanocrystals, one consequence of smallness is quantum confinement, which widens their energy gaps [136]. The threshold for absorption and the peak energy of their emission can be finely tuned through their size. Such control makes quantum dots very useful for lighting applications and as an alternative to fluorescent dyes in biological imaging [137, 138, 139, 140, 141, 142].

The quest to fully exploit quantum confinement brought with it a push to synthesize progressively smaller and monodisperse nanocrystals. As synthesis methods improved and reduced the size of nanoparticles into the sub-2-nm range, new properties emerged. In particular, nanocrystals that exhibit blue-shifted monochromatic light emission at larger sizes begin to show broad spectra when made ultrasmall [143, 144, 145, 146, 147, 148]. White light emission from ultrasmall CdSe nanocrystals [149, 150, 151, 152] is a particularly interesting case of such broad emission because of its potential for solid-state lighting.

It is also particularly intriguing as individual CdSe nanocrystals emit white light [153], ruling out its explanation as a superposition of narrow emission lines from nanoparticles of different sizes. On the other hand, it has been suggested that white light emission involves surface or defect states in the gap [149], but again, defect and surface states cannot explain the sudden appearance of a continuous spectrum of transition energies spanning the visual range when the diameter is reduced below 2 nm.

I used a combination of aberration-corrected transmission electron microscopy and finite-temperature density functional simulations to elucidate the mechanism of white light emission. A Nion UltraSTEM [18] equipped with a corrector capable of neutralizing up to fifth-order aberrations was used to obtain the Z-contrast images

at 60 kV and 100 kV. A VG Microscopes HB603 with a third-order Nion aberration corrector was used to acquire Z-contrast images at 300 kV. Both microscopes use a cold field emission source. Electron energy loss spectroscopy (EELS) was performed on the UltraSTEM using a Gatan Enfina EEL spectrometer.

The DFT simulations were performed using the generalized-gradient approximation and the projector-augmented-wave method with a plane-wave basis as implemented in the VASP code. The $Cd_{27}Se_{27}$ cluster was created by building a large supercell of bulk CdSe and removing the excess atoms. At least 2 nm of vacuum separate the atoms of adjacent supercells in the periodic supercell approach. All calculations were performed at the Γ point in k-space using the pseudopotentials, constructed for use with the Perdew-Burke-Ernzerhof exchange functional, supplied with VASP. An energy cutoff of 274.3 eV was used for bare CdSe. The atoms were allowed to move according to the forces without being constrained to retain any structural symmetries. Relaxation was performed using VASPs conjugate gradient method. In the finite-temperature quantum molecular dynamics simulations, atomic motion time-steps were chosen such that no atom could travel further than 0.1 per time-step. For bare CdSe we used 8 fs timesteps. For the calculations with ligands we introduced lighter elements, including H, and thus reduced the timestep to 1 fs. Because the ligands contain O we also used a higher energy cutoff of 400 eV in the calculations with ligands.

Optical emission data (collected by James R. McBride) and my Z-contrast scanning transmission electron microscopy (STEM) images from samples of various sizes of CdSe nanocrystals synthesized by McBride are shown in Figure 7.1. The figure documents the size and structure dependence of the optical properties. Monochromatic emission from red to green is seen to correlate with increasingly smaller diameters of wurtzite nanocrystal (Figure 7.1, (a) to (f)). Around each wurtzite core a fluxional surface layer of approximately a nanometer in thickness exists, appearing as a blurry layer in the STEM images (Figure 7.1, (a), (c) and (d)) because of the rapid rate at which the surface structure changes.

The images shown in Figure 7.1(a) to (c) are the result of summing several sequential frames from movies with fast per pixel times (1 to 2 microseconds per pixel). This method has a couple of advantages over using a single image with a long per pixel time to reduce noise. The nanoclusters tend to tilt on and off axis slightly under the beam. Using a fast per pixel time movie allows us to choose sequences where the particle is precisely on axis, whereas with a long per pixel time image, one can only hope the particle does not shift off axis during acquisition. The sample also tends to drift during image acquisition, which deforms images performed with a long per pixel time. Using a drift correction script I was able to align the frames in such movies. I have used such a script to remove most of drift effects from the images shown in Figure 7.1 (a) to (c). From these movies, the motion of the surface atoms is obvious.

Moving into the ultrasmall regime produces the broad white-light emission spectrum shown in Figure 7.1(g). The STEM observations confirm that the size distribution of the particles is far too narrow to produce such a spectrum through quantum confinement alone. Based on their sub-2-nm size, one would expect quantum confinement to produce only colors in the blue to ultra-violet range. The obvious difference from the larger monochromatic nanocrystals is the absence of the wurtzite crystal core. Successive frames (Figure 7.1, (g) to (h)) from a Z-contrast STEM movie of a typical white-light-emitting nanoparticle show it wriggling continuously. It was acquired with a 2 microsecond per pixel time and with a beam accelerating voltage of 60 kV, chosen to minimize knock-on damage. 60 kV is below the calculated knock-on damage threshold for even light materials such as boron nitride and carbon [154]. Despite operating in this gentle-STEM regime [20], every frame shows a significantly different structure. A fast per pixel scan time was required to resolve any individual atoms. Using a longer per pixel time resulted in less noisy images, but the atoms then move too quickly to be resolved. Using higher accelerating voltages of 100 kV or 300 kV increases the resolution of the STEM images but does not change the qualitative behavior of the ultrasmall CdSe under the beam. Every frame shows a significantly different structure at every accelerating voltage. Applying the averaging procedure

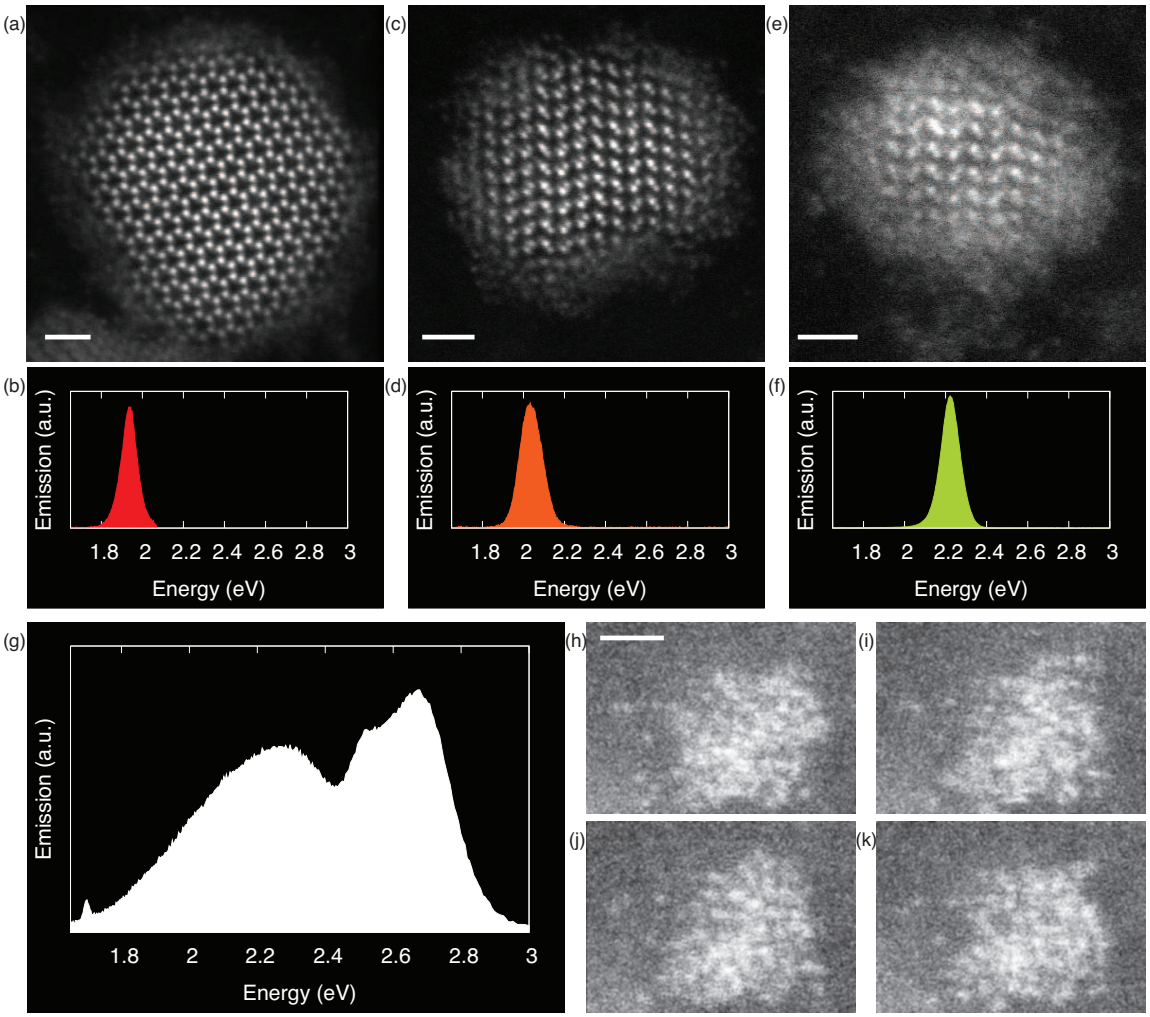

Figure 7.1: Atomic resolution Z-contrast STEM images and optical emission spectra from CdSe nanocrystals of 7 nm ((a) and (b)), 5 nm ((c) and (d)), and 3 nm ((e) and (f)) diameters. (g) White light spectrum emitted by ultrasmall sub-2-nm CdSe nanoclusters. ((h) to (k)) Successive frames from a STEM movie showing the continuous motion and disorder of the ultrasmall clusters. Scale bars are 1 nm.

used to produce the images of the larger monochromatic emitting clusters to the ultrasmall clusters results in a complete blur. The ultrasmall particles therefore cannot be regarded as crystalline, and hence I will refer to the white-light emitting structures as nanoclusters. The disordered fluxional surface layer seen around the larger nanocrystals appears to have consumed the whole crystal.

EELS was performed to check if the disordered material is the result of oxidation. The ligands used to synthesize the nanoclusters contain oxygen, so the presence of some oxygen is not unexpected. The oxygen signal I observed however was too low to be consistent with the formation of a disordered oxide shell around the CdSe nanocrystals.

The energy transfer from the fast electron beam is quite sufficient to be the cause of the continuous fluxional motion. The electron beam is known to impart heat to crystalline samples via inelastic scattering. The National Institute of Standards and Technology's ESTAR program [155] calculates electron stopping powers for electrons from the theory of Bethe [156, 157], with a density-effect correction evaluated according to Sternheimer [158, 159]. For 100 kV electrons ESTAR calculates the linear collision stopping power to be 1.38 eV/nm for CdSe (with a density of 5.816 g/cm3). The 100 kV electron beam therefore imparts about 2.8 eV per electron into a 2 nm CdSe nanocluster.

The white light spectrum spans from 1.7 to 3 eV, and is produced by exciting the nanoclusters with ultraviolet light. An electron excited by the absorption of a 3-eV ultraviolet photon must therefore loose up to 1.3 eV of energy to vibrations before emission in the visible spectrum can occur. For a 75-atom cluster, such an energy amounts to 17 meV per atom added to the existing thermal energy of the cluster at room temperature. For comparison, at the melting temperature of bulk Si, individual atoms possess a kinetic energy of 22 meV [160]. Furthermore, the melting point of nanoclusters decreases rapidly as their size decreases [161, 162, 163, 164, 165, 166]. Clearly something other than simple quantum confinement is causing the white emission. The only common property of the white light emitting nanoclusters seen by STEM is their dynamic amorphous structure. I therefore turned to DFT calculations

to test if such fluxionality could result from photoexcitation and cause the white light emission.

Carving out an ultrasmall $Cd_{27}Se_{27}$ nanocrystal from bulk wurtzite CdSe and relaxing it gives some hints as to the sensitivity of the electronic structure. Before relaxation, the nanocluster has no energy gap, but after relaxation it adopts a less crystalline structure, and a gap opens up. This result is consistent with previous theoretical work on magic-sized $Cd_{33}Se_{33}$ [167]. Heating the relaxed cluster up to room temperature (300 K) using quantum mechanical molecular dynamics, the cluster disorders further. The atoms move continuously, but after some time the motions look less wild. Relaxing the structure after the atomic motions have calmed down results in a structure lower in energy than the cluster relaxed from wurtzite. Therefore, I concluded that the ultrasmall nanoclusters are intrinsically disordered.

To estimate the effective temperature of a nanocluster that has absorbed an ultraviolet photon I use simple equipartition, i.e., at temperature T the energy per atom is (3/2)kT. An electron excited by a 3 eV ultraviolet photon must transfer up to 1.3 eV to vibrations in order for emission to occur in the range of white light emission, 1.7 to 3 eV. For the 54-atom cluster used in the simulations, such energy corresponds to 24 meV per atom, or an effective temperature of 186 K. When added to room temperature (300 K), this gives an effective temperature of around 500 K. To account for the additional vibrational energy imparted after the absorption of an ultraviolet photon, I therefore performed MD at 500 K . The extra energy makes the motion of the atoms more rapid and violent. Snapshots from the simulation are shown in Figure 7.2 (a) to (d). The atoms appear to move around as they do in the microscope.

The densities of states (DOS) calculated at 40 fs intervals during part of the 500 K MD simulation are shown in Figure 7.2(e). From this figure it is immediately clear that the continuous structural fluctuations result in correspondingly fluctuating energy gaps. The DOS have been colored according to the energy of their lowest unoccupied state. In determining the color, 1.2 eV was added to the calculated Kohn-Sham energy gaps, which are well known to be too small compared with measured values. The value 1.2 eV was chosen so that the first peak in the unoccupied DOS

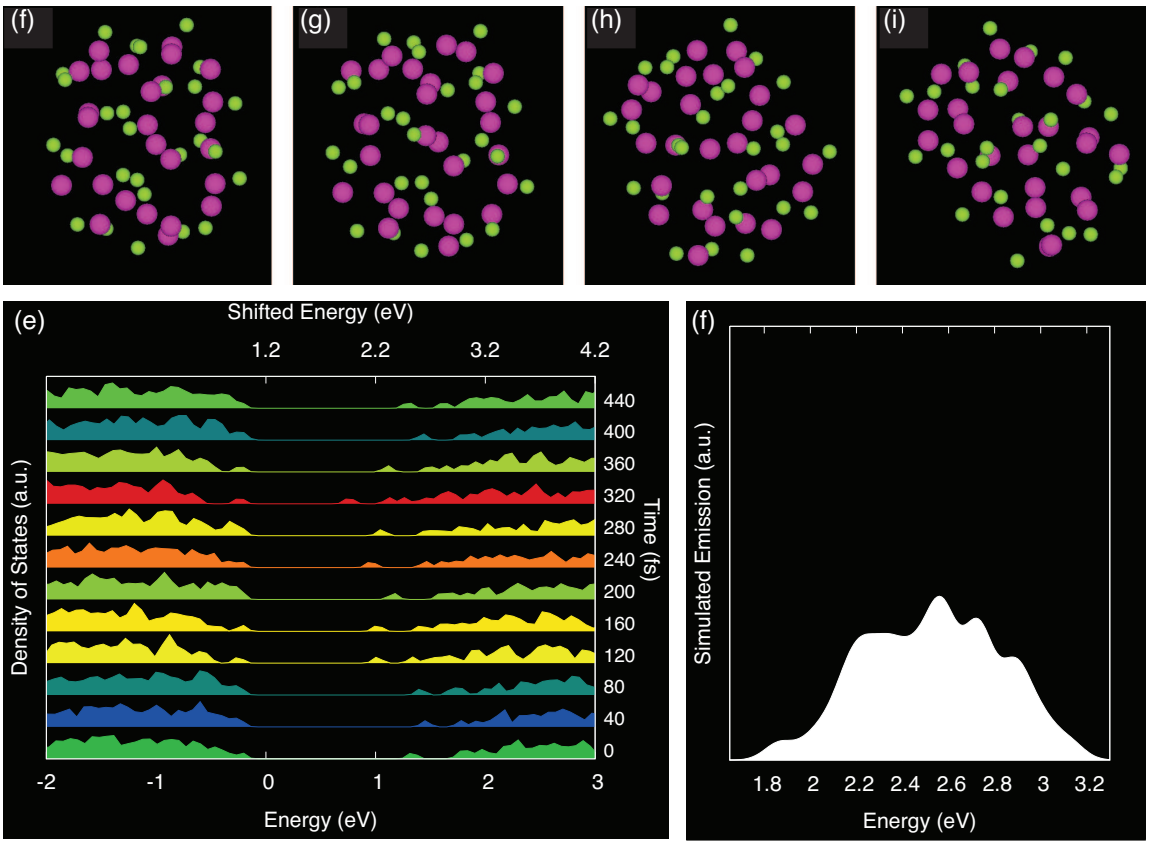

Figure 7.2: Density functional simulations of ultrasmall CdSe. ((a) to (d)) Snapshots from a 500 K quantum MD simulation of a $Cd_{27}Se_{27}$. (e) DOS calculated at 40 fs intervals during the 500 K simulation. The zero of the bottom energy axis has been set to the DFT Fermi level. The top axis has been shifted 1.2 eV to account for the well known underestimation of the band gap by DFT. Each DOS has been colored according to the energy of the lowest unoccupied state on this recalibrated axis. (f) An emission spectrum simulated from 20 DOS calculated at intervals of 40 fs.

of the relaxed steady-state structures matches the energy at which absorption begins experimentally. The colors span the range from red to blue. .

The first unoccupied peak in each DOS is separated from the continuous band of unoccupied states that appear at higher energies. In some cases an additional isolated peak appears between the first peak and the continuous band of unoccupied states. If one considers that emission may occur from all of these, the range of potential emission energies expands. One can get an idea of the spectrum that can be emitted by simply averaging over emission from the bottom of all the bands at 500 K. Figure 7.2(f) is the result of adding Gaussian peaks at each of these emission energies for 20 sets of DOS calculated at 40 fs intervals during the 500 K MD simulation, the first 12 of which are those shown in Figure 7.2(e). The energy axis includes the 1.2 eV rigid shift to the conduction band to facilitate comparison to experiment. The plot simulates the time-averaged emission of an excited ultrasmall nanocluster. The simulated spectrum matches the width and general shape of the experimental emission spectra.

I emphasize that the continuous emission spectrum arises from a continuously varying energy gap caused by the fluxionality. The bonds in the cluster are constantly and smoothly switching [168]. The evolving electronic states originate from different regions of the nanocluster, but the regions cannot be categorized as surface, bulk or trap states. As seen in other semiconductor nanoparticles [94, 169] the charge density of the states near the band gap are distributed through much of the simulated ultrasmall CdSe cluster, and therefore cannot be attributed to either surface or bulk states of the nanocluster. Charge density isosurfaces of the three highest occupied and three lowest unoccupied states for one of the $Cd_{27}Se_{27}$ structures produced during the 500 K molecular dynamics simulation are shown in Figure 7.3. Isosurfaces are plotted at 1% of the maximum charge density for each band.

The perceived color of the time-averaged emission depends on the shape of the emission spectrum, not just the range of emission energies. Experimentally, it is evident that the precise shape of the emission spectrum of ultrasmall CdSe depends on the mixture of ligands used in their synthesis [152]. All ultrasmall CdSe clusters,

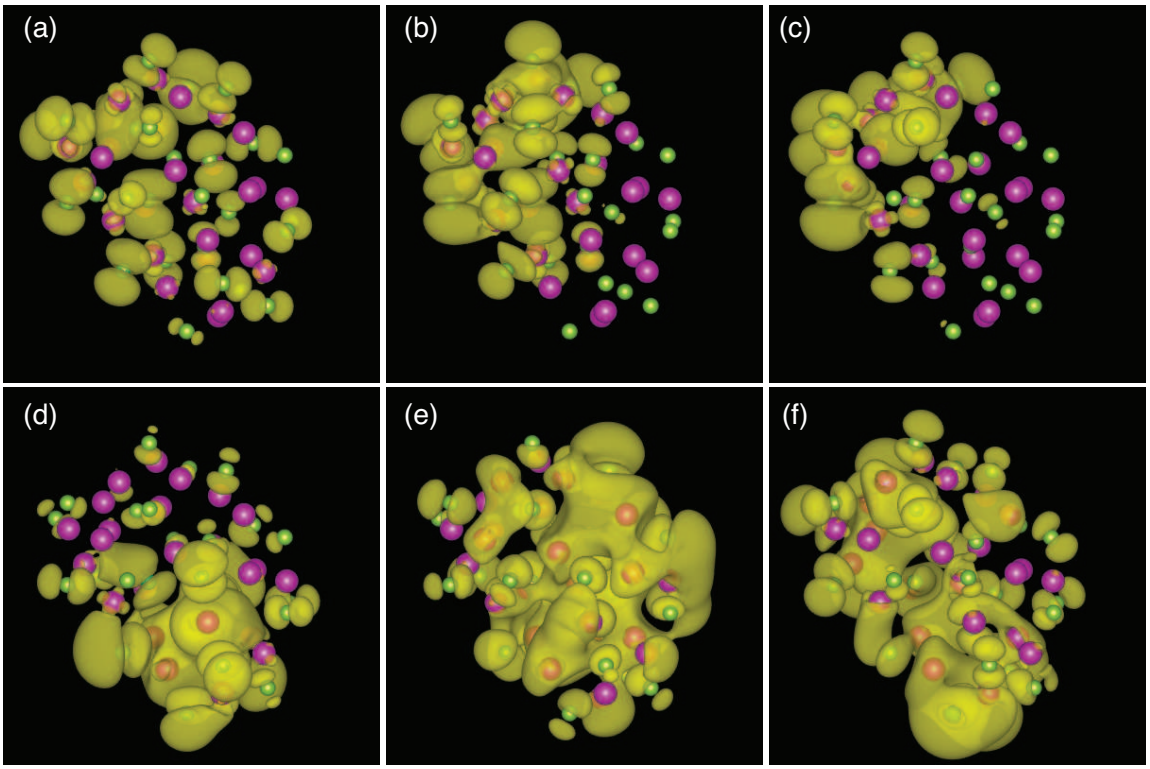

Figure 7.3: Charge density isosurfaces of the three highest occupied states ((a) to (c)) and three lowest unoccupied states ((d) to (f)) plotted for one of the $Cd_{27}Se_{27}$ structures produced during the 500 K molecular dynamics simulation.

however, emit broadly. Furthermore, simulations with partial ligand coverage produced levels of fluxionality similar to the bare clusters. Extended quantum molecular dynamics simulations of clusters covered by ligands are not practical, however I did perform some simulations with partial ligand coverage. I approximated the phosphonic acids used in the synthesis of the ultrasmall white light emitting CdSe by abbreviating the alkane chain to a single methyl group. The abbreviation has been shown [170] to accurately reproduce the band gap, band edge states, and binding energies of the full chain molecule on CdSe nanoclusters. First a single ligand was placed on a prerelaxed $Cd_{27}Se_{27}$ cluster. The optimal position for the ligand was found to be one in which it bonds to a Cd atom through the double bonded O atom, as has been reported before for other sizes of CdSe nanoclusters [170]. I then added six additional ligands in similar configurations distributed around the cluster, relaxed the structure, and performed MD. I observed the same kind of fluxionality at 500 K as I saw with the bare cluster, suggesting that the structural instability is intrinsic to ultrasmall nanoclusters. The instability is present because of the absence of a crystalline core and because the ligands do not form a continuously bonded outer shell. The mixture may tint the broad spectrum toward one color or another, but the origin of the broad visual spectrum is the fluxionality. The precise balance of colors is tuned by the ligands to result in the pure white-light emission spectrum.

In conclusion, the ultrasmall size marks the point at which the majority of atoms in a nanoparticle are at its surface. STEM observations and DFT simulations show that such a predominance of surface atoms can destabilize nanocrystals, causing them to take on a dynamic disordered structure. Furthermore, this fluxionality leads to a dynamic electronic structure. In ultrasmall CdSe, it leads to continuously changing energy gaps, resulting in their ability to individually exhibit a white time averaged emission spectrum. Fluxionality also exists at the surfaces of all the larger nanocrystals we have observed, and consequently, the ramifications exceed white light emission. This description of a nanocrystal surface is quite different from the concept of a stable trap state and may be relevant to observations of emission from poorly passivated nanocrystals as well as nanocrystal blinking [171, 172, 173]. F. A. Cotton [174] first

advocated the use of the term fluxionality in connection with organometallic molecules in 1968. Fluxionality of ultrasmall nanoclusters has been invoked in the past in the context of catalysis [165, 166] and has been discussed by other authors [164, 175, 176]. The present work establishes that fluxionality is the root of white-light emission by ultrasmall nanoclusters and that it persists at the surfaces of larger nanocrystals that emit monochromatic light. When optimizing nanocrystals for any application, such as solar cells, light emitting diodes, photocatalysis or biological imaging agents, dynamic fluxionality may be a critical consideration.

CHAPTER VIII

SUMMARY

In this thesis I used a combination of STEM and DFT to investigate a number of topical issues in condensed matter and materials physics. After initial explorations in magnesium oxide, which introduced me to density functional theory calculations, I studied STO/YSZ multilayers with first-principles calculations. I demonstrated that the origin of the observed colossal ionic conduction in the multilayers is a combination of strain on the YSZ and extreme disordering of its O sublattice, with both phenomena caused by lattice-constant and structure mismatch between the two materials. I also showed that the misfit strain is sustained because YSZ exhibits a stable phase with large strain. I then used a combination of STEM and EELS and theoretical EELS simulations to confirm the presence of a disordered YSZ O sublattice in coherent YSZ/SrTiO3 multilayers. O K-edge fine structure simulated for the strained disordered O sublattice phase of YSZ possesses blurred-out features compared to that of ordered cubic bulk YSZ, and experimental EELS fine structure taken from the strained YSZ of coherent YSZ/SrTiO3 thin films is similarly blurred out. Elemental mapping was shown to be capable of resolving ordered YSZ O sublattices. Elemental mapping of O in the coherent YSZ/STO multilayers was presented in which the O sublattice is seen to be clearly resolved in the STO but blurred out in the YSZ, indicating it to be disordered. In addition, I presented imaging and EELS results which show that strained regions exist at the incoherent interfaces of YSZ islands in STO with blurred out fine structure, suggesting these incoherent regions may also support high ionic conductivities. The presence of a region of O depleted STO at the interface with incoherent YSZ islands was revealed by EELS elemental mapping, implying the n-type doping of STO/YSZ nanocomposites with disconnected incoherent YSZ islands.

I described how it is now possible to use STEM with low accelerating voltages to identify individual atoms in light single layer materials such as BN. My collaborators

grew samples of BN and used a Nion UltraSTEM operated at 60 kV to image it. After using a probe-tail removing technique, they were able to determine from the Z-contrast image the chemical identify of every atom in a region of single layer BN, including C and O dopants. I performed DFT calculations to check the viability of the structure they believed they had identified. The simulation and the experiment agreed remarkably well, including small changes in bond lengths due to the presence of the dopants.

I tested the use of so called hybrid density functionals by applying the HSE06 hybrid density functional to $La_xCa_{1-x}MnO_3$. GGA outperforms GGA+U at predicting the magnetic ordering of LCMO for $x = 0$ to 0.5. However, because GGA slightly underestimates the Jahn-Teller distortions of LMO, it does not predict the correct magnetic ordering for $x = 1$ whereas GGA+U overestimates the distortions and predicts the correct magnetic ordering. I found the HSE06 hybrid density functional also slightly overestimates the Jahn-Teller distortions in LMO and gets the correct magnetic ordering. Unlike GGA+U, the hybrid functional also predicts the correct magnetic ordering at all the values of x I simulated, $x = 0, 0.33, 0.5$ and 1. The computational cost of using the hybrid functional was however a severe limitation, and the degree of convergence with respect to the number of kpoints for the $x = 0.33$ and 0.5 phases was not clear as I was not able to use more than 2 kpoints for these structures. The computational cost of such hybrid functionals would therefore seem to make them at present impractical for many of the systems of interest today, which tend to require larger supercells.

Nanotechnology depends on the fact that as structures are made smaller they acquire new properties. For semiconductor nanocrystals, one consequence of smallness is quantum confinement, which widens their energy gaps. I used DFT and TDLDA to study the optical gaps of free and embedded Si nanoclusters using models constructed by collaborators. I systematically compared the effects of deformation, the bonding of individual O atoms to their surfaces, and coverage by SiO_2 layers on the highest occupied molecular orbital-lowest unoccupied molecular orbital and optical gaps. I

found that all three can have a significant impact, but that O bonded to the surface and deformation cause the greatest reduction in the gaps, particularly in combination.

The quest to fully exploit quantum confinement brought with it a push to synthesize progressively smaller and monodisperse nanocrystals. The discovery that individual ultrasmall CdSe nanocrystals emit white light cannot be explained by quantum confinement alone. I have shown, using a combination of state-of-the-art DFT and STEM of nanoparticles provided by collaborators, how excitation sets the ultrasmall nanocrystals into a fluxional state. Because the structure of the ultrasmall sub-2nm particles is unstable, heat makes their structure continuously change, causing their energy gaps to vary continuously on a femtosecond time scale, so that even an individual nanocrystal emits across the entire visual range. In addition, we observe a layer of fluxional material around larger monochromatic emitting nanocrystals. Such fluxionality must be considered when optimizing nanocrystals for applications.

The chapters of this thesis show how the synergy of STEM and DFT can be used to elucidate the underlying mechanisms of new phenomena appearing on the forefront of condensed matter and materials physics. I make one final observation that has arisen coincidentally: Making materials ultrasmall or extremely thin can lead to disorder, and in turn new materials phenomena. As I showed with a combination of microscopy and theory, colossal ionic conductivity results from a disordered phase of YSZ that occurs when it is made into extremely thin strained layers of a multilayer structure. The Si nanoclusters I studied with DFT were ultrasmall and showed significant variations in their optical gaps when disordered by embedding them in a substrate or other means. The results could explain the experimental observation that the optical gaps of Si nanoparticles diverge from what is expected from quantum confinement alone when made very small. As with the Si nanoparticles, small CdSe nanocrystals behave as expected from quantum confinement, but ultrasmall CdSe behave differently. As I showed with STEM and DFT, instead of the monochromatic emission seen in larger nanocrystaline CdSe, fluxional disorder in ultrasmall CdSe leads to white light emission. Although small is different, ultrasmall or ultrathin are different yet again.

APPENDIX A

LIST OF REFEREED JOURNAL ARTICLES

1.1 Work Done as Part of This Thesis

T. J. Pennycook, J. R. McBride, S. J. Rosenthal, S. T. Pantelides and S. J. Pennycook, *"Dynamic fluctuations in ultrasmall nanocrystals induce white light emission"*, To be submitted to Nature Nanotechnology (2012).

A Rivera-Calzada, M R Diaz-Guillen, O J Dura, G Sanchez-Santolino, T.J. Pennycook, R Schmidt, F Y Bruno, J Garcia-Barriocanal, Z Sefrioui, N M Nemes, M Garcia-Hernndez, M Varela, C Leon, S T Pantelides, S J Pennycook, and J Santamaria, "Tailoring Interface Structure in Highly Strained YSZ/STO Heterostructures", Advanced Materials, **23** 5268 (2011).

T. J. Pennycook, M. P. Oxley, J. Garcia-Barriocanal, F. Y. Bruno, C. Leon, J. Santamaria, S. T. Pantelides, M. Varela and S. J. Pennycook, *"Seeing oxygen disorder in YSZ/$SrTiO_3$ colossal ionic conductor heterostructures using EELS"*, EPJ-AP, **54** 33507 (2011).

T. J. Pennycook, G. Hadjisavvas, J. C. Idrobo, P. C. Kelires and S. T. Pantelides, *"Optical gaps of free and embedded Si nanoclusters: Density functional theory calculations"*, Phys. Rev. B, **82**, 125310 (2010).

O. L. Krivanek, M. F. Chisholm, V. Nicolosi, T. J. Pennycook, G. J. Corbin, N. Dellby, M. F. Murfitt, C. S. Own, Z. S. Szilagyi, M. P. Oxley, S. T. Pantelides and S. J. Pennycook, *"Atom-by-atom structural and chemical analysis by annular dark-field electron microscopy"*, Nature **464**, 571 and Cover Page (2010).

T. J. Pennycook, M. J. Beck, K. Varga, M. Varela, S. J. Pennycook and S. T. Pantelides, *"Origin of colossal ionic conductivity in oxide multilayers: interface induced sublattice disorder"*, Phys. Rev. Lett. **104**, 115901 (2010).

1.2 Work Done in STEM as an Undergraduate

M. P. Oxley, M. Varela, T. J. Pennycook, K. van Benthem, S. D. Findlay, A. J. D'Alfonso, L. J. Allen and S. J. Pennycook, *"Interpreting atomic-resolution spectroscopic images"*, Phys. Rev. B, **76**, 064303 (2007).

M. Varela, T. J. Pennycook, W. Tian, D. Mandrus, S. J. Pennycook, V. Pena, Z. Sefrioui and J. Santamaria, *"Atomic scale characterization of complex oxide interfaces"*, J. Mater. Sci., **41**, 4389 (2006).

APPENDIX B

LIST OF TALKS AND POSTERS AT INTERNATIONAL MEETINGS

2.1 Talks

"*Structure of White Light Emitting CdSe*", Microscopy and Microanalysis, Nashville, TN, 2011.

"*Origin of colossal ionic conductivity in YSZ/STO multilayers*", Spring Materials Resarch Society Meeting, San Francisco, CA, 2011.

"*Origin of colossal ionic conductivity in YSZ/STO multilayers*", American Physical Society March Meeting, Dallas, TX, 2011.

"*Strain-Enhanced Ionic Conductivity*", International Federation of Societies for Microscopy International Microscopy Congress 17, Rio de Janeiro, Brazil, 2010.

"*Strain-Enhanced Ionic Conductivity*", Microscopy and Microanalysis, Portland, OR, 2010.

"*Hybrid density functional theory applied and the role of electron correlations in LCMO*", American Physical Society March Meeting, Portland, OR, 2010.

"*Origin of colossal ionic conductivity in YSZ-STO superlattices*", American Physical Society March Meeting, Pittsburgh, PA, 2009.

"*Effect of Mg doping on the Structure and Reflectivity of Alumina surfaces*",

American Physical Society March Meeting, New Orleans, LA, 2008.

2.2 Posters Presented During this Thesis

"*Elemental Mapping of Complex Oxides"*, Frontiers of Electron Microscopy in Materials Science, Sonoma, CA, 2007.

"*Elemental Mapping of Complex Oxides"*, Microscopy and Microanalysis, Ft. Lauderdale, FL, 2007.

2.3 Poster on STEM Presented as an Undergraduate

"*Spatial Resolution of Spectroscopic Imaging in Complex Oxides"*, Microscopy and Microanalysis, Honolulu HI, 2005.

APPENDIX C

AWARDS

3.1 Work Done as Part of This Thesis

International Federation of Societies for Microscopy Scholarship for "*Strain-Enhanced Ionic Conductivity*", 2010.

Microscopy Society of America, Presidential Scholar Award for "*Strain-Enhanced Ionic Conductivity*", 2010.

3.2 Work Done in STEM as an Undergraduate

Second Place, Graduate Student Poster Competition for "*Spatial Resolution of Spectroscopic Imaging in Complex Oxides*", Microscopy and Microanalysis, 2005.

Microscopy Society of America Undergraduate Research Scholarship for *"Atomic Scale Studies of Manganite Grain Boundaries with Colossal Magnetoresistance"*, 2005.

REFERENCES

[1] P. Hohenberg and W. Kohn, Physical Review **136**, 864 (1964)

[2] W. Kohn and L. Sham, Physical Review **140**, A1133 (1965)

[3] M. Payne, M. Teter, D. Allan, T. Arias, and J. Joannopoulos, Reviews of Modern Physics **64**, 1045 (1992)

[4] W. Kohn, Nobel lectures, chemistry, 1996-2000 **3**, 213 (2003)

[5] M. Ardenne, Zeitschrift fr Physik **109**, 553 (1938)

[6] A. V. Crewe and J. Wall, Journal of molecular biology **48**, 375 (1970)

[7] A. V. Crewe, J. Wall, and J. Langmore, Science **168**, 1338 (1970)

[8] S. Pennycook and D. Jesson, Physical Review Letters **64**, 938 (1990)

[9] S. J. Pennycook and L. A. Boatner, Nature **336**, 565 (1988)

[10] J. Liu and J. M. Cowley, Ultramicroscopy **52**, 335 (1993)

[11] P. D. Nellist, Science **305**, 1741 (2004)

[12] J. Hillier and R. F. Baker, Journal of Applied Physics **15**, 663 (1944)

[13] C. Colliex, Ultramicroscopy **1**, 301 (1976)

[14] N. D. Browning, M. F. Chisholm, and S. J. Pennycook, Nature **366**, 143 (1993)

[15] P. E. Batson, Nature **366**, 727 (1993)

[16] H. Sawada, F. Hosokawa, T. Kaneyama, T. Tomita, Y. Kondo, T. Tanaka, Y. Oshima, Y. Tanishiro, N. Yamamoto, and K. Takayanagi, *EMC 2008 14th European Microscopy Congress 1–5 September 2008, Aachen, Germany* (Springer Berlin Heidelberg, Berlin, Heidelberg, 2008)

[17] R. Erni, M. D. Rossell, C. Kisielowski, and U. Dahmen, Physical Review Letters **102**, 96101 (2009)

[18] O. L. Krivanek, G. J. Corbin, N. Dellby, B. F. Elston, R. J. Keyse, M. F. Murfitt, C. S. Own, Z. S. Szilagyi, and J. W. Woodruff, Ultramicroscopy **108**, 179 (2008)

[19] O. L. Krivanek, M. F. Chisholm, V. Nicolosi, T. J. Pennycook, G. J. Corbin, N. Dellby, M. F. Murfitt, C. S. Own, Z. S. Szilagyi, M. P. Oxley, S. T. Pantelides, and S. J. Pennycook, Nature **464**, 571 (2010)

[20] O. L. Krivanek, N. Dellby, M. F. Murfitt, M. F. Chisholm, T. J. Pennycook, K. Suenaga, and V. Nicolosi, Ultramicroscopy **110**, 935 (2010)

[21] D. B. Williams and C. B. Carter, *Transmission electron microscopy* (Springer Verlag, 2009)

[22] O. Scherzer, Journal of Applied Physics **20**, 20 (1949)

[23] M. Haider, S. Uhlemann, E. Schwan, H. Rose, B. Kabius, and K. Urban, Nature **392**, 768 (1998)

[24] O. L. Krivanek, N. Dellby, and A. R. Lupini, Ultramicroscopy **78**, 1 (1999)

[25] P. Batson, N. Dellby, and O. Krivanek, Nature **418**, 617 (2002)

[26] M. Haider, S. Uhlemann, and J. Zach, Ultramicroscopy **81**, 163 (2000)

[27] O. L. Krivanek, P. D. Nellist, N. Dellby, M. F. Murfitt, and Z. Szilagyi, Ultramicroscopy **96**, 229 (2003)

[28] H. Sawada, F. Hosokawa, T. Kaneyama, T. Ishizawa, M. Terao, M. Kawazoe, T. Sannomiya, T. Tomita, Y. Kondo, T. Tanaka, Y. Oshima, Y. Tanishiro, N. Yamamoto, and K. Takayanagi, Japanese Journal of Applied Physics **46**, L568 (2007)

[29] H. Sawada, Y. Tanishiro, N. Ohashi, T. Tomita, F. Hosokawa, T. Kaneyama, Y. Kondo, and K. Takayanagi, Journal of Electron Microscopy **58**, 357 (2009)

[30] P. Nellist and S. Pennycook, Physical Review Letters **81**, 4156 (1998)

[31] M. P. Oxley, M. Varela, T. Pennycook, K. van Benthem, S. Findlay, A. d'Alfonso, L. Allen, and S. Pennycook, Physical Review B **76**, 064303 (2007)

[32] M. Oxley and S. Pennycook, Micron **39**, 676 (2008)

[33] W. Kohn, *Course LXXIV* (Proceedings of the International School of Physics "Enrico Fermi", 1985)

[34] J. Perdew and Y. Wang, Physical Review B **45**, 13244 (1992)

[35] H. J. Monkhorst and J. D. Pack, Physical Review B **13**, 5188 (1976)

[36] J. Phillips, Physical Review **112**, 685 (1958)

[37] C. Park and D. Yoon, Journal of the American Ceramic Society **84**, 456 (2001)

[38] C. Park and D. Yoon, Journal of the American Ceramic Society **85**, 1585 (2002)

[39] B.-K. Kim, S.-H. Hong, S.-H. Lee, D.-Y. Kim, and N. M. Hwang, Journal of the American Ceramic Society **86**, 634 (2003)

[40] C. W. Park, D. Y. Yoon, J. E. Blendell, and C. A. Handwerker, Journal of the American Ceramic Society **86**, 603 (2003)

[41] K. Sohlberg, S. J. Pennycook, and S. T. Pantelides, Journal of the American Chemical Society **121**, 7493 (1999)

[42] S. Cai, S. N. Rashkeev, S. T. Pantelides, and K. Sohlberg, Physical Review Letters **89**, 235501 (2002)

[43] H. Knözinger and P. Ratnasamy, Catalysis Reviews **17**, 31 (1978)

[44] A. A. Tsyganenko and P. P. Mardilovich, Journal of the Chemical Society, Faraday Transactions **92**, 4843 (1996)

[45] B. Steele and A. Heinzel, Nature **414**, 345 (2001)

[46] R. M. Ormerod, Chemical Society Reviews **32**, 17 (2002)

[47] J. Goodenough, Annual review of materials research **33**, 91 (2003)

[48] J. A. Kilner, Nature Materials **7**, 838 (2008)

[49] J. Maier, Solid State Ionics **131**, 13 (2000)

[50] N. Sata, K. Eberman, K. Eberl, and J. Maier, Nature **408**, 946 (2000)

[51] A. Peters, C. Korte, D. Hesse, N. Zakharov, and J. Janek, Solid State Ionics **178**, 67 (2007)

[52] C. Korte, A. Peters, J. Janek, D. Hesse, and N. Zakharov, Physical Chemistry Chemical Physics **10**, 4623 (2008)

[53] I. Kosacki, C. Rouleau, P. Becher, J. Bentley, and D. Lowndes, Solid State Ionics **176**, 1319 (2005)

[54] C. Fisher and H. Matsubara, Journal Of The European Ceramic Society **19**, 703 (1999)

[55] G. Mahan and W. Roth, *Superionic conductors*, Physics of solids and liquids (Plenum Press, 1976)

[56] S. Hull, Reports on Progress in Physics **67**, 1233 (2004)

[57] C. Nichols, C. Van de Walle, and S. Pantelides, Physical Review Letters **62**, 1049 (1989)

[58] J. Garcia-Barriocanal, A. Rivera-Calzada, M. Varela, Z. Sefrioui, E. Iborra, C. Leon, S. J. Pennycook, and J. Santamaria, Science **321**, 676 (2008)

[59] K. Suzuki, M. Kubo, Y. Oumi, R. Miura, H. Takaba, A. Fahmi, A. Chatterjee, K. Teraishi, and A. Miyamoto, Applied Physics Letters **73**, 1502 (1998)

[60] J. Matthews and A. Blakeslee, J. Cryst. Growth **27**, 118 (1974)

[61] R. Car and M. Parrinello, Physical Review Letters **55**, 2471 (1985)

[62] P. Blöchl, O. JEPSEN, and O. Andersen, Physical Review B **49**, 16223 (1994)

[63] G. Kresse and J. Furthmuller, Physical Review B **54**, 11169 (1996)

[64] K. Nordlund, Computational Materials Science **3**, 448 (1995)

[65] X. Zhao, D. Ceresoli, and D. Vanderbilt, Physical Review B **71**, 85107 (2005)

[66] T. J. Pennycook, M. J. Beck, K. Varga, M. Varela, S. J. Pennycook, and S. T. Pantelides, Physical Review Letters **104**, 115901 (2010)

[67] M. Bosman, M. Watanabe, D. T. L. Alexander, and V. J. Keast, Ultramicroscopy **106**, 1024 (2006)

[68] M. Varela, M. P. Oxley, W. Luo, J. Tao, M. Watanabe, A. R. Lupini, S. T. Pantelides, and S. J. Pennycook, Physical Review B **79**, 085117 (2009)

[69] R. Buczko, G. Duscher, S. Pennycook, and S. Pantelides, Physical Review Letters **85**, 2168 (2000)

[70] W. Luo, M. Varela, J. Tao, S. J. Pennycook, and S. T. Pantelides, Physical Review B **79**, 052405 (2009)

[71] L. Allen, S. Findlay, M. Oxley, and C. Rossouw, Ultramicroscopy **96**, 47 (2003)

[72] L. Allen and C. Rossouw, Physical Review B **42**, 11644 (1990)

[73] M. Oxley and L. Allen, Physical Review B **57**, 3273 (1998)

[74] M. Kim, G. Duscher, N. Browning, K. Sohlberg, S. Pantelides, and S. Pennycook, Physical Review Letters **86**, 4056 (2001)

[75] R. Klie, J. Buban, M. Varela, A. Franceschetti, C. Jooss, Y. Zhu, N. Browning, S. Pantelides, and S. Pennycook, Nature **435**, 475 (2005)

[76] A. Cavallaro, M. Burriel, J. Roqueta, A. Apostolidis, A. Bernardi, A. Tarancon, R. Srinivasan, S. N. Cook, H. L. Fraser, J. A. Kilner, D. W. McComb, and J. Santiso, Solid State Ionics **181**, 592 (2010)

[77] J. C. Meyer, A. Chuvilin, G. Algara-Siller, J. Biskupek, and U. Kaiser, Nano Letters **9**, 2683 (2009)

[78] C. Jin, F. Lin, K. Suenaga, and S. Iijima, Physical Review Letters **102**, 195505 (2009)

[79] N. Alem, R. Erni, C. Kisielowski, M. D. Rossell, W. Gannett, and A. Zettl, Physical Review B **80**, 155425 (2009)

[80] M. Isaacson, D. Kopf, M. Ohtsuki, and M. Utlaut, Ultramicroscopy **4**, 101 (1979)

[81] P. M. Voyles, D. A. Muller, J. L. Grazul, P. H. Citrin, and H. J. L. Gossmann, Nature **416**, 826 (2002)

[82] P. Schiffer, A. Ramirez, W. Bao, and S. Cheong, Physical Review Letters **75**, 3336 (1995)

[83] C. Ritter, M. Ibarra, J. De Teresa, P. Algarabel, C. Marquina, J. Blasco, J. Garcia, S. Oseroff, and S. Cheong, Physical Review B **56**, 8902 (1997)

[84] J. Heyd, G. Scuseria, and M. Ernzerhof, The Journal of Chemical Physics **118**, 8207 (2003)

[85] J. Perdew, M. Ernzerhof, and K. Burke, The Journal of Chemical Physics **105**, 9982 (1996)

[86] J. Perdew, M. Ernzerhof, K. Burke, and A. Savin, International Journal of Quantum Chemistry **61**, 197 (1997)

[87] M. Ernzerhof and G. Scuseria, The Journal of Chemical Physics **110**, 5029 (1999)

[88] C. Adamo and V. Barone, The Journal of Chemical Physics **110**, 6158 (1999)

[89] J. P. Perdew, K. Burke, and M. Ernzerhof, Physical Review Letters **77**, 3865 (1996)

[90] J. Heyd, J. Peralta, G. Scuseria, and R. Martin, The Journal of Chemical Physics **123**, 174101 (2005)

[91] K. Hirschman, L. Tsybeskov, S. Duttagupta, and P. Fauchet, Nature **384**, 338 (1996)

[92] R. Collins, P. Fauchet, and M. Tischler, Physics Today **50**, 24 (1997)

[93] A. Fowler, Physics Today **50**, 50 (1997)

[94] A. Puzder, A. Williamson, J. Grossman, and G. Galli, Physical Review Letters **88**, 97401 (2002)

[95] K. Seino, F. Bechstedt, and P. Kroll, Nanotechnology **20**, 135702 (2009)

[96] M. Cazzanelli, D. Kovalev, L. Dal Negro, Z. Gaburro, and L. Pavesi, Physical Review Letters **93**, 207402 (2004)

[97] J. Proot, C. Delerue, and G. Allan, Applied Physics Letters **61**, 1948 (1992)

[98] L. Wang and A. Zunger, The Journal of Physical Chemistry **98**, 2158 (1994)

[99] S. Schuppler, S. Friedman, M. Marcus, D. Adler, Y. Xie, F. Ross, Y. Chabal, T. Harris, L. Brus, W. Brown, E. Chaban, P. Szajowski, S. Christman, and P. Citrin, Physical Review B **52**, 4910 (1995)

[100] M. V. Wolkin, J. Jorne, and P. M. Fauchet, Physical Review Letters **82**, 197 (1999)

[101] D. Kovalev, E. Gross, N. Künzner, F. Koch, V. Timoshenko, and M. Fujii, Physical Review Letters **89**, 137401 (2002)

[102] M. Carrada, A. Wellner, V. Paillard, C. Bonafos, H. Coffin, and A. Claverie, Applied Physics Letters **87**, 251911 (2005)

[103] T. Van Buuren, L. Dinh, L. Chase, W. Siekhaus, and L. Terminello, Physical Review Letters **80**, 3803 (1998)

[104] J. Von Behren, T. Van Buuren, M. Zacharias, E. Chimowitz, and P. Fauchet, Solid State Communications **105**, 317 (1998)

[105] L. Patrone, D. Nelson, V. Safarov, M. Sentis, W. Marine, and S. Giorgio, Journal of Applied Physics **87**, 3829 (2000)

[106] K. D. Rinnen and M. Mandich, Physical Review Letters **69**, 1823 (1992)

[107] J. C. Idrobo, M. Yang, K. Jackson, and S. Ogut, Physical Review B **74**, 153410 (2006)

[108] J. C. Idrobo, A. Halabica, R. H. Magruder, R. F. Haglund, S. J. Pennycook, and S. T. Pantelides, Physical Review B **79**, 125322 (2009)

[109] I. Vasiliev, J. R. Chelikowsky, and R. Martin, Physical Review B **65**, 121302 (2002)

[110] M. Luppi and S. Ossicini, Physical Review B **71**, 35340 (2005)

[111] Z. Zhou, L. Brus, and R. Friesner, Nano Letters **3**, 163 (2003)

[112] A. Puzder, A. Williamson, J. Grossman, and G. Galli, Journal of the American Chemical Society **125**, 2786 (2003)

[113] E. Luppi, E. Degoli, G. Cantele, S. Ossicini, R. Magri, D. Ninno, O. Bisi, O. Pulci, G. Onida, M. Gatti, A. Incze, and R. Del Sole, Optical Materials **27**, 1008 (2005)

[114] Q. Li, R. Zhang, S. Lee, T. Niehaus, and T. Frauenheim, Applied Physics Letters **91**, 043106 (2007)

[115] C. Garoufalis and A. Zdetsis, Physical Chemistry Chemical Physics **8**, 808 (2006)

[116] A. Seraphin, S. Ngiam, and K. Kolenbrander, Journal of Applied Physics **80**, 6429 (1996)

[117] L. Ramos, J. Furthmüller, and F. Bechstedt, Applied Physics Letters **87**, 143113 (2005)

[118] L. Ramos, J. Furthmüller, and F. Bechstedt, Physical Review B **70**, 33311 (2004)

[119] L. Ramos, J. Furthmüller, and F. Bechstedt, Physical Review B **71**, 35328 (2005)

[120] N. Daldosso, M. Luppi, S. Ossicini, E. Degoli, R. Magri, G. Dalba, P. Fornasini, R. Grisenti, F. Rocca, and L. Pavesi, Physical Review B **68**, 85327 (2003)

[121] H. Peter Kroll, physica status solidi (b) **243**, R47 (2006)

[122] G. Hadjisavvas and P. Kelires, Physica E: Low-dimensional Systems and Nanostructures **38**, 99 (2007)

[123] R. Guerra, I. Marri, R. Magri, L. Martin-Samos, O. Pulci, E. Degoli, and S. Ossicini, Superlattices and Microstructures **46**, 246 (2009)

[124] R. Guerra, E. Degoli, and S. Ossicini, Physical Review B **80**, 155332 (2009)

[125] G. Hadjisavvas and P. Kelires, Physical Review Letters **93**, 226104 (2004)

[126] S. Öğüt, J. Chelikowsky, and S. Louie, Physical Review Letters **79**, 1770 (1997)

[127] M. L. Tiago, J. C. Idrobo, S. Oguet, J. Jellinek, and J. R. Chelikowsky, Physical Review B **79**, 155419 (2009)

[128] M. del Puerto, M. Jain, and J. R. Chelikowsky, Physical Review B **81**, 035309 (2010)

[129] F. Wooten, K. Winer, and D. Weaire, Physical Review Letters **54**, 1392 (1985)

[130] Y. Tu and J. Tersoff, Physical Review Letters **84**, 4393 (2000)

[131] Y. Tu and J. Tersoff, Physical Review Letters **89**, 086102 (2002)

[132] J. Chelikowsky, N. Troullier, and Y. Saad, Physical Review Letters **72**, 1240 (1994)

[133] Y. Zhou, Y. Saad, M. Tiago, and J. Chelikowsky, Physical Review E **74**, 066704 (2006)

[134] D. Chong, *Recent advances in density functional methods*, Recent advances in computational chemistry (World Scientific, 1995)

[135] I. Vasiliev, S. Öğüt, and J. Chelikowsky, Physical Review B **65**, 115416 (2002)

[136] L. E. Brus, The Journal of Chemical Physics **80**, 4403 (1984)

[137] V. L. Colvin, M. C. Schlamp, and A. P. Alivisatos, Nature **370**, 354 (1994)

[138] M. Bruchez Jr, M. Moronne, P. Gin, S. Weiss, and A. P. Alivisatos, Science **281**, 2013 (1998)

[139] S. Coe, W.-K. Woo, M. Bawendi, and V. Bulović, Nature **420**, 800 (2002)

[140] W. U. Huynh, J. J. Dittmer, and A. P. Alivisatos, Science **295**, 2425 (2002)

[141] M. A. Schreuder, J. D. Gosnell, N. J. Smith, M. R. Warnement, S. M. Weiss, and S. J. Rosenthal, Journal of Materials Chemistry **18**, 970 (2008)

[142] S. J. Rosenthal, J. C. Chang, O. Kovtun, J. R. Mcbride, and I. D. Tomlinson, Chemistry & Biology **18**, 10 (2011)

[143] C. Landes, M. Braun, and M. El-Sayed, Journal Of Physical Chemistry B **105**, 10554 (2001)

[144] V. N. Soloviev, A. Eichhofer, D. Fenske, and U. Banin, Journal of the American Chemical Society **123**, 2354 (2001)

[145] X. Chen, A. Samia, Y. Lou, and C. Burda, Journal of the American Chemical Society **127**, 4372 (2005)

[146] P. Dagtepe, V. Chikan, J. Jasinski, and V. J. Leppert, Journal of physical chemistry. C **111**, 14977 (2007)

[147] O. E. Rayevska, G. Y. Grodzyuk, V. M. Dzhagan, O. L. Stroyuk, S. Y. Kuchmiy, V. F. Plyusnin, V. P. Grivin, and M. Y. Valakh, The Journal of Physical Chemistry C **114**, 22478 (2010)

[148] M. S. Devadas, J. Kim, E. Sinn, D. Lee, T. Goodson III, and G. Ramakrishna, The Journal of Physical Chemistry C **114**, 22417 (2010)

[149] M. Bowers II, J. McBride, and S. Rosenthal, Journal of the American Chemical Society **127**, 15378 (2005)

[150] R. Jose, Z. Zhelev, R. Bakalova, Y. Baba, and M. Ishikawa, Applied Physics Letters **89**, 013115 (2006)

[151] M. J. Bowers Ii, J. R. Mcbride, M. D. Garrett, J. A. Sammons, A. D. Dukes Iii, M. A. Schreuder, T. L. Watt, A. R. Lupini, S. J. Pennycook, and S. J. Rosenthal, Journal of the American Chemical Society **131**, 5730 (2009)

[152] J. McBride, A. Dukes III, M. Schreuder, and S. Rosenthal, Chemical Physics Letters **498**, 1 (2010)

[153] A. D. I. Dukes, P. C. Samson, J. D. Keene, L. M. Davis, J. P. Wikswo, and S. J. Rosenthal, Journal of Physical Chemistry A **115**, 4076 (2011)

[154] A. Zobelli, A. Gloter, C. Ewels, G. Seifert, and C. Colliex, Physical Review B **75**, 245402 (2007)

[155] M. J. Berger, J. S. Coursey, M. A. Zucker, and C. J., "ESTAR, PSTAR, and ASTAR: Computer Programs for Calculating Stopping-Power and Range Tables for Electrons, Protons, and Helium Ions(version1.2.3).." "http://www.wikipedia.org"

[156] H. Bethe, Annalen der Physik **397**, 325 (1930)

[157] H. Bethe, Zeitschrift fr Physik **76**, 293 (1932)

[158] R. Sternheimer, Physical Review **88**, 851 (1952)

[159] R. Sternheimer, S. Seltzer, and M. Berger, Physical Review B **26**, 6067 (1982)

[160] M. Beck, R. Schrimpf, D. Fleetwood, and S. Pantelides, Physical Review Letters **100**, 185502 (2008)

[161] P. Buffat and J. Borel, Physical Review A **13**, 2287 (1976)

[162] P. Ajayan and L. Marks, Physical Review Letters **63**, 279 (1989)

[163] A. N. Goldstein, C. M. Echer, and A. P. Alivisatos, Science **256**, 1425 (1992)

[164] L. Marks, Reports on Progress in Physics **57**, 603 (1994)

[165] B. Yoon, H. H. kkinen, U. Landman, A. S. W. rz, J.-M. Antonietti, S. e. Abbet, K. Judai, and U. Heiz, Science **307**, 403 (2005)

[166] S. N. Rashkeev, A. R. Lupini, S. Overbury, S. J. Pennycook, and S. T. Pantelides, Physical Review B **76**, 035438 (2007)

[167] A. Puzder, A. Williamson, F. Gygi, and G. Galli, Physical Review Letters **92**, 217401 (2004)

[168] Y. S. Su and S. T. Pantelides, Physical Review Letters **88**, 165503 (2002)

[169] T. Pennycook, G. Hadjisavvas, J. C. Idrobo, Kelires, P.C., and S. T. Pantelides, Physical Review B **82**, 125310 (2010)

[170] A. Puzder, A. Williamson, N. Zaitseva, G. Galli, L. Manna, and A. Alivisatos, Nano Letters **4**, 2361 (2004)

[171] M. G. Bawendi, P. J. Carroll, W. L. Wilson, and L. E. Brus, The Journal of Chemical Physics **96**, 946 (1992)

[172] T. Plakhotnik, M. Fernée, B. Littleton, H. Rubinsztein-Dunlop, C. Potzner, and P. Mulvaney, Physical Review Letters **105**, 167402 (2010)

[173] A. A. Cordones, T. J. Bixby, and S. R. Leone, The Journal of Physical Chemistry C **115**, 6341 (2011)

[174] F. Cotton, Accounts of Chemical Research **1**, 257 (1968)

[175] M. R. Hoare and P. Pal, Journal of Crystal Growth **17**, 77 (1972)

[176] D. Vollath and F. D. Fischer, Progress in Materials Science **56**, 1030 (2011)